EVALUATING UNMANNED AERIAL VEHICLE REMOTE SENSING TOWARDS IMPROVING SITE-SPECIFIC MANAGEMENT

A Dissertation

by

GREGORY SCOTT ROUZE

Submitted to the Office of Graduate and Professional Studies of
Texas A&M University
in partial fulfillment of the requirements for the degree of

DOCTOR OF PHILOSOPHY

Chair of Committee,	Cristine Morgan
Co-Chair of Committee,	Haly Neely
Committee Members,	Binayak Mohanty
	Nithya Rajan
	John Thomasson
Head of Department,	David Baltensberger

December 2019

Major Subject: Soil Science

ABSTRACT

Unmanned aerial vehicles (UAVs) offer exciting new potentials within the field of precision agriculture. However, the technology remains in an experimental setting because of questions concerning data quality and quantity. To address these concerns, field research was conducted within a cotton cropping system, with particular applications focused on management zone delineation and evapotranspiration (ET) mapping. The overall objective of this proposal is to evaluate the suitability of UAV imagery (i.e. thermal, near-infrared, visible) as decision-making tools for precisions agriculture or site-specific management. UAVs were analyzed in terms of their ability to: 1) define MZs at various points before, during, and at the end of, a growing season, and 2) estimate ET using energy balance models. Results from Chapter 2 indicate that multispectral, thermal, and RGB imagery were significant predictors of in-season yield indicators such as canopy height and yield itself. In addition, MZs showed significant separation during flowering and boll filling, respectively. Results from Chapter 3 indicate that non-contextual energy balance models outperformed those of contextual models using eddy covariance data. Furthermore, LE model performance varied by soil type. Results from Chapter 4 indicate that upscaling UAV data is an important component towards practical management operations. In particular, it was better to evaluate UAV imagery at initial resolutions (here ~1.3 m) before aggregating to coarser resolutions.

CONTRIBUTORS

Contributors

This work was supervised by a dissertation committee consisting of Professors Cristine Morgan (chair), Haly Neely (co-chair), Nithya Rajan of the Department of Soil & Crop Sciences, and Professor(s) Binayak Mohanty and John Thomasson of the Department of Biological and Agricultural Engineering. Bill Kustas from the USDA-Agricultural Research Service served as an advising member for the committee as well. At the time of submission, Dr. Neely has accepted a new job as Assistant Professor at Washington State University, while Dr. Morgan has accepted a new job as Chief Scientific Officer at the Soil Health Institute. Anyone that is interested in obtaining the original data presented in this dissertation should speak with Dr. Rajan, as she is the sole remaining committee member at the Heep Center on Texas A&M campus. All other questions regarding analysis should be redirected towards my personal email at gregoryrouze0@gmail.com.

The RGB imagery and the multispectral imagery used in the original articles from Chapters 2-4 was orthomosaicked by Jinha Jung and Anjin Chang from the Engineering and Computer Science Department at Texas A&M Corpus Christi University. All unmanned aerial imagery was collected by Ian Gates and Andrew Vree, with direction by Dr. Dale Cope. Ground control points were designed by Cody Bagnall, with direction by Dr. Alex Thomasson. Ground control point spatial coordinates were collected by Cody Bagnall and Matthew Wiethorn. Radiometric calibration data for UAV multispectral imagery was collected by Cody Bagnall. Manned aerial imagery was

collected by Chenghai Yang. CSAT-3 and LI-7500 sensors for eddy covariance towers were provided by members of the United States Department of Agriculture Agricultural Research Service, including Bill Kustas, John Prueger, and Lynn McKee. All other sensor data was provided by Binayak Mohanty as part of the Texas Water Observatory. Additional field data collection includes the following student workers: Kenny Le, Nicole Shigley, Michael Hiefner, Matthew Wiethorn. All other work conducted for the dissertation was completed by the student independently.

Funding was provided by Texas A&M Agrilife Research, specifically from Corporate Relations members such as Bob Avant and team.

NOMENCLATURE

Abbreviation	Description	Units
LAI	leaf area index	$m^2\ m^{-2}$
EC_a	apparent electrical conductivity	$mS\ m^{-1}$
MZ	management zone	-
UAV	unmanned aerial vehicle	-
MAV	manned aerial vehicle	-
SAT	satellite	-
AICc	Akaike Information Criterion "corrected"	-
GPS	global positioning system	-
NDVI	normalized difference vegetation index	unitless
RGB	red + green + blue	-
AGL	above ground level	-
DAP	days after planting	-
NAWF	nodes above white flower	-
ICI	Infrared Cameras Inc.	-
GCP	ground control point	-
SFM	structure from motion	-
RMSE	root mean squared error	-
NIR	near-infrared	-
ρ_{NIR}	near infra-red reflectance	unitless
ρ_{Red}	red reflectance	unitless
T_r	radiometric surface temperature	K
IRT	infra-red thermography	-
MAE	mean absolute error	-
OLS	ordinary least squares	-
ANOVA	analysis of variance	-
ET	evapotranspiration	$mm\ time^{-1}$
DATTUTDUT	Deriving Atmospheric Turbulence Transport Useful to Dummies Using Temperature	-
TSEB	Two-source Energy Balance Model	-

LE	latent heat flux	W m^{-2}
R_n	net radiation	W m^{-2}
G	soil heat flux	W m^{-2}
H	sensible heat flux	W m^{-2}
SEB	surface energy balance	-
λ	latent heat of vaporization	J kg^{-1}
LE_c	canopy latent heat flux	W m^{-2}
$R_{n,c}$	canopy net radiation	W m^{-2}
H_c	canopy sensible heat flux	W m^{-2}
LE_s	soil latent heat flux	W m^{-2}
$R_{n,s}$	soil net radiation	W m^{-2}
H_s	soil sensible heat flux	W m^{-2}
T_c	canopy radiometric surface temperature	K
T_s	soil radiometric surface temperature	K
f_c	vegetation fraction cover	-
TSEB-PT	Two-source Energy Balance Model Priestley-Taylor	-
TSEB-DTD	Two-source Energy Balance Model Dual-Time Difference	-
TSEB-2T	Two-source Energy Balance Model two-component temperature	-
GDD	growing degree days	-
IOP	intense observation period	-
CMOS	complementary metal-oxide-semiconductor	-
UFPA	uncooled focal plane array	-
DN	digital number	-
T_{br}	brightness temperature	K
T_{bg}	Background temperature	K
ε	overall emissivity	unitless

θ_v	volumetric water content	unitless
AWD	available water depleted	unitless
θ_{FC}	volumetric water content at field capacity	unitless
θ_{WP}	volumetric water content at wilting point	unitless
ρ	air density	kg m^{-3}
w	vertical wind speed	m s^{-1}
q	vapor flux mass fraction	kg kg^{-1}
C_p	specific heat capacity	kJ kg^{-1} K^{-1}
ρC_p	volumetric heat capacity	J m^{-3} K^{-1}
α_{PT}	Priestley–Taylor coefficient	unitless
Δ	the slope of the saturation vapor pressure-temperature curve	Pa K^{-1}
γ	psychrometric constant	Pa K^{-1}
r_a	aerodynamic resistance to momentum and heat transfer	s m-1
T_a	air temperature	K
$\Omega(\theta)$	vegetation clumping factor at given θ viewing angle	unitless
r_s	soil resistance to momentum and heat transfer	s m-1
$T_{r,0}$	Surface radiometric temperature in the AM	K
$NDVI_{soil}$	soil normalized difference vegetation index	unitless
$NDVI_{veg}$	vegetation normalized difference vegetation index	unitless
ρ_0	surface albedo	unitless
EF	evaporative fraction	unitless
R_s, Sw_{in}	incoming shortwave radiation	W m^{-2}
ε_0	surface emissivity	unitless

ε_a	atmospheric emissivity	unitless
$T_{r,max}$	hottest pixel within scene	K
$T_{r,min}$	coldest pixel within scene	K
NDVI∞	maximum or infinite NDVI	unitless
e_a	actual vapor pressure	kPa?
$f(x_i,y_i,z_m)$	weight for footprint	-
MBE	mean bias error	-
MBPE	mean bias percent error	-
MSE_u	unsystematic mean squared error	-
NMM	neutron moisture meter	-
TIR	thermal infrared	-
MODTRAN	Moderate Resolution Atmospheric Transmission	-
In-SA	Input aggregation, simple average	-
In-BC	Input aggregation, boxcox average	-
Out-SA	Output aggregation, simple average	-
Out-BC	Output aggregation, boxcox average	-
z_{oh}	roughness length for heat transfer	-
z_{om}	roughness length for momentum transfer	-
METRIC	Mapping EvapoTranspiration at high Resolution with Internalized Calibration	-
ASTER	Advanced Spaceborne Thermal Emission and Reflection Radiometer	-
OLI	Operational Land Imager	-
TIRS	Thermal Infrared Sensor	-
τ	transmissivity	unitless

LEDAPS	Landsat Ecosystem Disturbance Adaptive Processing System	-
h_c	canopy height	m
w_c	canopy width	m
pyTSEB	A Python Two Source Energy Balance Model	-
E_r	relative error	-
μ	spatial mean of fine resolution pixels	-
u*	friction velocity	m s^{-1}
$L_{n,c}$	canopy net longwave radiation	W m^{-2}
$L_{n,s}$	soil net longwave radiation	W m^{-2}
$S_{n,c}$	canopy net shortwave radiation	W m^{-2}
$S_{n,s}$	soil net shortwave radiation	W m^{-2}
r_x	resistance between canopy and canopy boundary layer	s m^{-1}

TABLE OF CONTENTS

Page

LIST OF FIGURES

Page

LIST OF TABLES

Page

1. INTRODUCTION

1.1. General context

Within production farming, there exists a global and persistent challenge to sustain the inhabitants of this world, both in the present and in the future. These inhabitants include not only humans and animals but crops as well. While crop growth is affected by parameters (e.g. temperature, humidity, rain, wind, etc.) that cannot be controlled, crops can still be managed through inputs such as water, fertilizer, pesticides, and herbicides. The question then becomes how to optimize these management inputs, often expressed in terms of the five R's: how do we select the right input, in the right amount, to the right place, at the right time, and in the right manner? These input questions are weighed against two additional objectives. First, profitability and input efficiency should be maximized, meaning that the total costs of production (i.e. labor, machinery, seed, water use, etc.) should be far less than the total revenue obtained from yields; second, adverse environmental impacts such as soil erosion and nutrient leaching should be minimized (Shannon et al., 2018).

Farmers have sought to achieve these goals by considering the abiotic and biotic environment within a given field. Average environmental conditions are often assumed, and inputs are applied uniformly across the entire field (Babcock and Pautsch, 1998). This approach can become problematic within fields that exhibit large degrees of spatial and temporal variability. Spatial variability within this context refers to "changes in soil, crop, landscape, and environmental attributes that occur across a certain area", while

temporal variability refers to these same sources of variability, only "within a certain area at different measurement times" (Whelan and Taylor, 2013). Parameters that vary in space and time include: 1) soil texture, 2) soil structure, 3) soil depth, 4) soil organic matter, 5) soil water, 6) soil pH, 7) soil nutrients, 8) weeds, 9) insects, 10) diseases, 11) terrain, 12) past crop management, and 13) crop growth parameters such as vegetation fraction cover and leaf area index (LAI) (Whelan and Taylor, 2013).

The presence of spatial and temporal variability for both soils and crops has implications for management. In irrigation management, water that is uniformly applied across a variable field can result in soils becoming over-/under-irrigated; in such a situation, crops can become stressed to the point of premature death, resulting in potential yield reductions (King et al., 2006). In weed management, uniform application of herbicides across a heterogeneous field can result in greater weed resilience (Shannon et al., 2018). Therefore, fields with spatial and/or temporal variability may benefit from strategies beyond uniform management, so that agronomic, environmental, and economic losses can be minimized, a term referred to as precision agriculture or site-specific management (Nawar et al., 2017). Site-specific management is also defined as a "management strategy that uses information technology to bring data from multiple sources to bear on decisions associated with crop production" (National Research Council, 1997).

One tool that has been used to depict field variability, and thus facilitate site-specific management, is through an imaging sensor. Imaging sensors non-invasively collect radiation from several portions of the electromagnetic spectrum, including the shortwave

visible/near infrared (400-1400 nm) and longwave thermal infrared (7-14 μm) regions. The radiation signal received by these instruments is then then tied back with physical characteristics of objects on the ground, such as soils and crops - reviews on remote sensing applications within agriculture are well documented (Bastiaanssen et al., 2000; Pinter Jr. et al., 2003; Liaghat and Balasundram, 2010; Khanal et al., 2017). The wealth of literature regarding remote sensing and agriculture has focused on sensors equipped aboard platforms such as satellites and manned aircraft. Satellites, while generally extensive and free, remain infeasible for site-specific management, as they are inflexible and provide inadequate (i.e. 30 m or greater) resolutions. This problem is partially offset with manned aircraft, but its imagery can be burdened by high acquisition costs.

Alternative to satellites and manned aircraft, images can be obtained from lower flying unmanned aerial vehicles (UAVs). UAVs offer improved spatial and temporal resolutions relative to satellites, and at a fraction of the cost relative to manned aircraft. Despite these technical improvements, UAVs have not been integrated within the site-specific management framework for agriculture applications - this is because technological developments in UAVs have often outpaced the rate at which research can be performed (McCabe et al., 2017). While recent review papers have indicated UAVs have plenty of applications for crop monitoring (Manfreda et al., 2018), such demonstrations have not been provided for more complex applications, such as variable rate technology, where spatially accurate orthomosaics (with < 1 day turnaround times) are currently required (Hunt Jr and Daughtry, 2017). Thus, there is a need to first evaluate UAVs within the context of relatively simple agriculture applications before

proceeding to more complex questions. Subsequent discussion will focus on motivations for the three research articles presented in this dissertation, specifically regarding UAVs.

1.2. Literature review

1.2.1. Chapter 2 literature review

Site-specific farming allows decision-making strategies to vary within fields where large spatial and temporal variability is observed. Site-specific farming has recently become enhanced using variable rate technologies (VRT). VRT constitutes the use of global positioning systems (GPS), decision support systems, and machinery that can change the rate of planting or application of an input (e.g. agrochemical, water etc.) as the tractor moves along the field (Schimmelpfennig, 2016). Since the late 1990s, VRT has been applied to fertilizers, seeds and water, citing economic and environmental benefits, although this will depend to some extent on the temporal variance of the specific management parameter (Pierce and Novak, 1999; Balafoutis et al., 2017; Sui and Yan, 2017).

VRT is aided by defining management zones (MZs), which are broad and unbroken areas where a specific management or treatment is applied (Doerge, 1999). MZs are categorized by the scale where data is collected, and the category of VRT equipment (Whelan and Taylor, 2013). In grain crops, such as corn and soybeans, MZs are often made at the end of a season using yield maps via yield monitors (Brock et al., 2005). However, in non-food crops, such as cotton, yield monitors can be difficult to obtain, especially with older field equipment (Gaylon Morgan, personal communication, 2018). MZs can alternatively be created using soil grid sampling, but such an approach is not

particularly time- and cost-effective (Viscarra-Rossel et al., 2011). Farmer knowledge-based MZs, while a cheaper alternative than soil sampling, maybe unreliable because variability can change within a growing season, and this may not be consistent from year to year (Whelan and McBratney, 2000). Alternatively, bulk soil apparent electrical conductivity (EC_a) sensors have been successful in mapping soil properties such as soil available water holding capacity and even making MZs (Sudduth et al., 2005; Hedley and Yule, 2009; Stanislav, 2010). However, EC_a MZs, like farmer knowledge MZs, are limited because the plant environment changes with weather within a giving growing season (Stoorvogel et al., 2015). While initial MZ approaches have had some success in defining MZs between growing seasons, they are not particularly useful for delineating MZs within a particular growing season.

Within this context, UAVs have potential for delineating MZs because they can adequately respond to temporally dynamic conditions. UAVs can be categorized in terms of rotocopters and fixed-wing platforms (Sankaran et al., 2015). Sensors that have been equipped on UAVs include visible (red, green, blue or RGB) sensors (Bendig et al., 2014), multispectral sensors (Candiago et al., 2015), hyperspectral sensors (Ishida et al., 2018), thermal sensors (Gómez-Candón et al., 2016), and LIDAR sensors (Khan et al., 2017). The holistic framework for UAV-based remote sensing includes: 1) identifying the problem, 2) data acquisition planning, 3) the flight itself, 4) orthorectification, 5) radiometric calibration and 6) analytics – this process then operates within a feedback loop back to farm managers (McKee, 2017). Recent demonstrations of UAV-based MZs have been performed within sugarcane (Magalhães et al., 2013), olives (Gertsis et al.,

2015) and maize (Sona et al., 2016). However, such capabilities have not been performed within row crops such as cotton.

MZ studies with row crops may be sparse because its value has not been shown to farmers. A recent survey by Erickson (2017) indicates that, in 2017, only 6 % of farmers were using UAVs, and only 22 % are expected to use UAVs by 2020. Low adoption rates maybe occurring because there is a wide variety of sensors available on the market, as optical, multispectral, thermal, hyperspectral and laser sensors have all positively contributed to site-specific management (Hunt Jr and Daughtry, 2017; Manfreda et al., 2018). However, there is no indication as to which sensor is most appropriate, especially within MZ delineation. Initial results from Rouze et al. (2018) suggest that, during a growing season, UAV thermal imagery can be favorable over multispectral imagery, because the former exhibits greater spatial structure. At the end of the growing season, visible (i.e. RGB) imagery may serve as an alternative tool for delineating MZs compared with soil mapping. One motivation for favoring UAV RGB imagery, in addition to an increased spatial resolution, is price. Sensors for RGB cost an average of $1500 USD (Manfreda et al., 2018). Recent literature (Martineli Sanches et al., 2018) indicates that UAV RGB shows promise in modeling sugarcane yield ($R^2 = 0.79$), but no such conclusions have been demonstrated within cotton.

1.2.2. Chapter 3 literature review

Quantifying evapotranspiration (ET) is important because it controls ecosystem functioning, carbon and climate feedbacks, agricultural management and water resources (Fisher et al., 2017). The concept of ET has thus been utilized by scientists and

stakeholders alike for developing decision-making strategies, such as water rights allocation and monitoring, provisioning and regulating ecosystem services, and rangeland management (Anderson et al., 2012). Within the precision agriculture industry, farmers have applied knowledge of ET toward crop water management (Hunsaker et al., 2005; Davis and Dukes, 2010). However, recent water management practices have resulted in problems for farmers, particularly within semiarid environments, such as water scarcity (Qadir et al., 2003). Responsible crop water management means applying only enough water so that actual crop requirements can be met (Calera et al., 2017).

Water management is conducted through irrigation scheduling. Irrigation scheduling is based on estimating actual water crop requirements. Initial formulations of crop water requirements were obtained from the FAO-56 Penman Monteith method (Allen et al., 1998). In this method, ET is calculated based on assumptions of root zone depth and soil moisture (Allen et al., 1998). This method, however, is problematic because the parameter values may not be precise because root zone depths can vary in space due to differences in the local environment, such as soil moisture and nutrient availability (Calera et al., 2017). Crop ET has also been obtained directly using the water balance equation (Hunsaker et al., 2003). Estimating ET using the soil water balance method has been critiqued for several reasons. Measurements, while direct, are collected over very small areas (up to 100 m^2, World Meteorological Organization, 2014) and may not be representative over the area of interest - implementing an experimental design to account for this limitation is costly (Jones et al., 2004). Experimental designs become even more

costly if the area of interest exhibits soil spatial variability. In addition, changes in soil water storage are not directly tied with changes in plant response or physiology (Jones et al., 2004). In particular, the leaf water potential is controlled by not only soil moisture, but also on the rate of water movement throughout the plant (Jones et al., 2004).

The energy balance method has been presented as an alternative to previous methods. The energy balance method is advantageous over FAO-56 because measurements are direct, and it is advantageous over the water balance because measurements are obtained across larger areas (larger than 100 m^2). A generalized energy balance equation is defined as:

$$LE = R_n - G - H, \quad \text{(Eq. 1.1)}$$

where LE is latent energy flux (conceptually analogous to ET), R_n is net radiation, G is soil heat flux, H is sensible heat flux, all in W m^{-2}. ET is then calculated from LE by dividing the latent heat of vaporization or λ (units of J kg^{-1}) and the density of water (1000 kg m^{-3} at 20° C, Allen et al., 1998).

Latent heat fluxes are estimated with one-source and two-source energy balance models (OSEB and TSEB, respectively) that use thermal and multispectral imagery as inputs (Anderson et al., 1997; Bastiaanssen et al., 1998). Unlike one-source models, two-source models estimate the fluxes for canopies and soils separately (Liou et al., 2014). One-source energy balance models include Mapping Evapotranspiration at High Resolution and with Internalized Calibration (METRIC) and Deriving Atmosphere Turbulent Transport Useful to Dummies (DATTUTDUT). DATTUTDUT only requires surface temperature measurements, whereas METRIC additionally requires multispectral

imagery and weather station data (Xia et al., 2016). TSEB models include TSEB-Priestley Taylor (or TSEB-PT), TSEB-Penman Monteith (or TSEB-PM), and Dual Temperature Difference (TSEB-DTD) (Anderson et al., 1997; Norman et al., 2000). Gowda et al. (2008) found that the errors of these energy balance models ranged from 2.7-35% across all land surface types.

Given the plethora of energy balance models, it is important to quantify the uncertainty of LE (and ET) estimates through model comparisons. Colaizzi et al. (2014), for example, quantified differences in accuracy between TSEB-PT and TSEB-PM for evaporation and transpiration separately using eddy flux measurements. In their results, Colaizzi et al. (2014) obtained an evaporation root-mean squared error of 273 and 76 %, respectively; for transpiration, a root-mean squared error (RMSE) of 13 and 55 % for PT and PM, respectively. However, their modeling results used ground infrared thermometers over small areas. French et al. (2015) conducted an energy balance model comparison between TSEB-PT and METRIC models within cotton using satellite (i.e. Landsat) remote sensing data. In their results, French et al. (2015) showed similar agreement in estimating ET between the two models but suggested that METRIC and TSEB-PT should be preferred in data sparse and data-plentiful situations, respectively. Xia et al. (2016) compared DATTUTDUT with TSEB-PT using manned aircraft and found that the former was unsatisfactory in situations where a scene did not contain pixels with extreme ET conditions.

Energy balance modeling have recently been performed for UAVs. There are a few examples of UAV-based data being used in energy balance modeling and comparisons,

such as grasslands (Brenner et al., 2017), barley (Hoffmann et al., 2016), olives (Ortega-Farias et al., 2016) and wine grapes (Kustas et al., 2018). Within cotton, energy balance model comparisons using UAVs are non-existent. Identifying the appropriate model within a cotton crop growing season would benefit future irrigation management strategies.

1.2.3. Chapter 4 literature review

Evaluating ET using remote sensing has been established since the early 1990s (Price, 1990; Moran and Jackson, 1991; Kustas et al., 1994). ET estimates are important towards improving crop water management across various spatial scales (Khanal et al., 2017). To obtain ET, remote sensing platforms such as satellites and manned aircraft are equipped with sensors that capture thermal and multispectral imagery; these images along with ground-truth data are used as inputs, and LE fluxes are estimated with one- and two-source energy balance models (Anderson et al., 1997; Bastiaanssen et al., 1998). ET fluxes are then validated using independent measurement sources such as a lysimeter (water balance) or an eddy covariance flux tower (energy balance) (Verstraeten et al., 2008).

The accuracy of modeled ET fluxes can be expressed as a function of remote sensing platform. Satellite ET fluxes are on the order of hundreds of meters, while manned aerial vehicle fluxes on the order of meters. However, satellite-based imagery is usually free, while manned aerial vehicle imagery costs based on the amount of land surveyed. UAVs have been touted with providing data with higher spatial resolutions on the order of centimeters (Matese et al., 2015; Xia et al., 2016; Khanal et al., 2017). UAVs, however,

present their own unique set of challenges. Unlike satellite data processing, UAV processing is left to the user, requiring highly specialized expertise (Manfreda et al., 2018). Additionally, considerable time is needed to handle and post process all the relevant data needed for energy balance modeling. Finally, sensors equipped aboard UAVs are more limited in terms of geometric and radiometric quality (Manfreda et al., 2018). For example, UAV payloads for thermal imagery are restricted to uncooled microbolometers, and these sensors exhibit lower precision and accuracy relative to cooled microbolometers (Ribero-Gomes et al., 2016). Thus, tradeoffs exist between these different platforms, and one universal solution does not currently exist.

Identifying the most appropriate platform for given a given application has initially been conducted using cost-benefit analyses (Matese et al., 2015). Value within an ET context can also be assessed in terms of water savings. An appropriate water savings strategy will first require comparing the accuracy in modeled ET fluxes as a function of spatial scale or pixel resolution. Li et al. (2008), for example, modeled ET using original and resampled Landsat 5 imagery at three different pixel sizes: 30, 120 and 960 meters. These comparisons were performed within a semi-arid watershed that consisted of shrublands and riparian areas. Poor agreement with ground-truth EC fluxes were found with the 960 m imagery, which was caused by sub-pixel heterogeneity. In other words, a single pixel can contain multiple land uses, surface roughness and moisture content values (Kustas et al., 2004). Within a predominantly row-crop (i.e. maize/soybean) dominated watershed, McCabe and Wood (2006) found similar results for satellite imagery at 60, 90 and 1000 m, with prediction errors of 2, 5 and 15 % respectively.

Across smaller spatial scales relevant to production agriculture, there are a lack of studies comparing ET fluxes, both within across remote sensing platforms. For management applications, UAV imagery needs to be aggregated to a coarser spatial resolution, as the pixel resolutions from UAVs are often too fine (i.e. cm-scale). Within this context, there is a need to evaluate the effect of aggregation on UAV estimated ET.

1.3. Objectives of dissertation

The overall objective of this proposal is to evaluate the suitability of UAV imagery (i.e. thermal, near-infrared, visible) as decision-making tools for precisions agriculture or site-specific management. Additionally, ground-truth information will serve to complement the data collected by the UAVs. UAVs will be analyzed in terms of their ability to: 1) define MZs at various points before, during, and at the end of, a growing season, and 2) estimate ET using energy balance models.

1.3.1. Objectives for chapter 2

The overall objective of the first chapter of the dissertation is to evaluate UAV imagery as a tool for creating MZs that can be used for site-specific decision making, before during, and at the end of, a single growing season. UAV collected data and a soil EC_a map will be used to create MZs. The UAV data include thermal, multispectral (red, green, blue or RGB, near infrared or NIR) and visible imagery. A yield map will be created with EC_a and compared with a yield map from the UAV visible imagery. Both UAV and EC_a will be compared in terms of how well they predict agronomic characteristics, both within and at the end of a season. Finally, UAV and EC_a -based MZs will be tested and compared in terms of significant differences between individual

zones – an MZ map is valid if the individual zones are unique from one another. MZs will be delineated using the k-means algorithm. This chapter provides a basic MZ-oriented example of using UAV data in production-agriculture fields.

1.3.2. Objectives for chapter 3

The overall objective of the second chapter of the dissertation is to evaluate the accuracy and spatial responsiveness of energy balance models created from multispectral and thermal UAV imagery. The energy balance models include are one-source models, such as DATTUTDUT, and two-source models, such as TSEB-PT, TSEB-PM and TSEB-DTD. These models will be used to estimate ET at a cm-scale on a 16-ha cotton field. These models will be compared to ET eddy covariance flux towers that collect flux data. To compare flux tower ET measurements with the fine-scale UAV-based modeling ET estimates, a footprint model will be used to create a spatially averaging scheme. The value of such a study will provide some guidance on how UAV-based models of ET can best be created, with the goal of water savings and/or yield improvements.

1.3.3. Objectives for chapter 4

The overall objective of the third chapter of the dissertation is to evaluate a *single* energy balance model (i.e. TSEB-PT) across multiple platforms (i.e. UAVs, manned aircraft, satellite) using eddy covariance flux tower measurements. Landsat 8 will be selected as the satellite for this study. Outcomes from this chapter will be that readers would consider the usefulness of UAVs as a function of plot size – unless the areas surveyed are very large, every effort should attempt to utilize UAVs for real-time management.

1.4. Dissertation outline

The dissertation is divided into five chapters. The first chapter has provided a broad overview of the motivations for the dissertation through a literature review. Chapters 2, 3, and 4 are original research articles, while Chapter 5 summarizes the findings from Chapters 2-4, while providing an outlook detailing future research that is needed.

1.5. References

Allen, R. G., Pereira, L. S., Raes, D., & Smith, M. (1998). *Crop evapotranspiration (guidelines for computing crop water requirements). FAO Irrigation and Drainage. No. 56.* Rome, Italy.

Anderson, M. C., Allen, R. G., Morse, A., & Kustas, W. P. (2012). Use of Landsat thermal imagery in monitoring evapotranspiration and managing water resources. *Remote Sensing of Environment*, *122*, 50–65.

Anderson, M. C., Norman, J. M., Diak, G. R., Kustas, W. P., & Mecikalski, J. R. (1997). A two-source time-integrated model for estimating surface fluxes using thermal infrared remote sensing. *Remote Sensing of Environment*, *60*(2), 195–216.

Babcock, B. A., & Pautsch, G. R. (1998). Moving from uniform to variable fertilizer rates on Iowa corn: Effects on rates and returns. *Journal of Agricultural and Resource Economics*, *23*(2), 385–400.

Balafoutis, A., Beck, B., Fountas, S., Vangeyte, J., Van Der Wal, T., Soto, I., et al. (2017). Precision agriculture technologies positively contributing to ghg emissions mitigation, farm productivity and economics. *Sustainability*, *9*(8), 1–28.

Bastiaanssen, W. G. M., Menenti, M., Feddes, R. A., & Holtslag, A. A. M. (1998). A remote sensing surface energy balance algorithm for land (SEBAL) 1. Formulation. *Journal of Hydrology*, *213*, 198–212.

Bastiaanssen, W. G. M., Molden, D. J., & Makin, I. W. (2000). Remote sensing for irrigated agriculture: Examples from research and possible applications. *Agricultural Water Management*, *46*(2), 137–155.

Bendig, J., Yu, K., Aasen, H., Bolten, A., Bennertz, S., Broscheit, J., et al. (2015). Combining UAV-based plant height from crop surface models, visible, and near infrared vegetation indices for biomass monitoring in barley. *International Journal of Applied Earth Observation and Geoinformation*, *39*, 79–87.

Brenner, C., Thiem, C. E., Wizemann, H. D., Bernhardt, M., & Schulz, K. (2017). Estimating spatially distributed turbulent heat fluxes from high-resolution thermal imagery acquired with a UAV system. *International Journal of Remote Sensing*, *38*, 1–24.

Brock, A., Brouder, S. M., Blumhoff, G., & Hofmann, B. S. (2005). Defining yield-based management zones for corn-soybean rotations. *Agronomy Journal*, *97*(4), 1115–1128.

Calera, A., Campos, I., Osann, A., D'Urso, G., & Menenti, M. (2017). Remote sensing for crop water management: From ET modelling to services for the end users. *Sensors*, *17*(5), 1104.

Candiago, S., Remondino, F., De Giglio, M., Dubbini, M., & Gattelli, M. (2015). Evaluating multispectral images and vegetation indices for precision farming applications from UAV images. *Remote Sensing*, *7*(4), 4026–4047.

Colaizzi, P. D., Agam, N., Tolk, J. A., Evett, S. R., Howell, T. A., Gowda, P. H., et al. (2014). Two-source energy balance model to calculate E, T, and ET: Comparison of Priestley-Taylor and Penman-Monteith formulations and two time scaling methods. *Transactions of the ASABE*, *57*(2), 479–498.

Davis, S. L., & Dukes, M. D. (2010). Irrigation scheduling performance by evapotranspiration-based controllers. *Agricultural Water Management*, *98*(1), 19–28.

Doerge, T. (2001). Fitting soil electrical conductivity measurements into the precision farming toolbox. In *2001 Wisconsin Fertilizer, Aglime and Pest Management Conference*. Madison, Wisconsin.

Erickson, B., Lowenberg-Deboer, J., & Bradford, J. (2017). *2017 Precision Agriculture Dealership Survey*. *Purdue University*. Lafayette, IN.

Fisher, J. B., Melton, F., Middleton, E., Hain, C., Anderson, M., Allen, R., et al. (2017). The future of evapotranspiration: global requirements for ecosystem functioning, carbon and climate feedbacks, agricultural management, and water resources. *Water Resources Research*, *53*, 2618–2626.

French, A. N., Hunsaker, D. J., & Thorp, K. R. (2015). Remote sensing of evapotranspiration over cotton using the TSEB and METRIC energy balance models. *Remote Sensing of Environment*, *158*, 281–294.

Gertsis, A., Fountas, D., Arpasanu, I., & Michaloudis, M. (2013). Precision agriculture applications in a high density olive grove adapted for mechanical harvesting in Greece. *Procedia Technology*, *8*, 152–156.

Gómez-Candón, D., Virlet, N., Labbé, S., Jolivot, A., & Regnard, J. L. (2016). Field phenotyping of water stress at tree scale by UAV-sensed imagery: new insights for thermal acquisition and calibration. *Precision Agriculture*, *17*(6), 786–800.

Gowda, P. H., Chavez, J. L., Colaizzi, P. D., Evett, S. R., Howell, T. A., & Tolk, J. A. (2008). ET mapping for agricultural water management: Present status and challenges. *Irrigation Science*, *26*(3), 223–237. doi:10.1007/s00271-007-0088-6

Hedley, C. B., & Yule, I. J. (2009). Soil water status mapping and two variable-rate irrigation scenarios. *Precision Agriculture*, *10*, 342–355.

Hoffmann, H., Nieto, H., Jensen, R., Guzinski, R., Zarco-Tejada, P., & Friborg, T. (2016). Estimating evaporation with thermal UAV data and two-source energy balance models. *Hydrology and Earth System Sciences*, *20*, 697–713.

Hunsaker, D. J., Pinter, P. J., Barnes, E. M., & Kimball, B. A. (2003). Estimating cotton evapotranspiration crop coefficients with a multispectral vegetation index. *Irrigation Science*, *22*(2), 95–104. doi:10.1007/s00271-003-0074-6

Hunsaker, D. J., Barnes, E. M., Clarke, T. R., & Fitzgerald, G. J. (2005). Cotton irrigation scheduling using remotely sensed and FAO-56 basal crop coefficients. *Transactions of the ASABE*, *48*(4), 1395–1408.

Hunt, E. R., & Daughtry, C. S. T. (2017). What good are unmanned aircraft systems for agricultural remote sensing and precision agriculture? *International Journal of Remote Sensing*, 1–32.

Ishida, T., Kurihara, J., Viray, F. A., Namuco, S. B., Paringit, E. C., Perez, G. J., et al. (2018). A novel approach for vegetation classification using UAV-based hyperspectral imaging. *Computers and Electronics in Agriculture*, *144*, 80–85.

Jones, H. G. (2004). Irrigation scheduling: Advantages and pitfalls of plant-based methods. *Journal of Experimental Botany*, *55*(407), 2427–2436.

Khan, S., Aragão, L., & Iriarte, J. (2017). A UAV–lidar system to map Amazonian rainforest and its ancient landscape transformations. *International Journal of Remote Sensing*, *38*(8–10), 2313–2330.

Khanal, S., Fulton, J., & Shearer, S. (2017). An overview of current and potential applications of thermal remote sensing in precision agriculture. *Computers and Electronics in Agriculture*, *139*, 22–32.

King, B. A., Stark, J. C., & Wall, R. W. (2006). Comparison of site-specific and conventional uniform irrigation management for potatoes. *Applied Engineering in Agriculture*, *22*(5), 677–688.

Kustas, W. P., Moran, M. S., Humes, K. S., Stannard, D. I., Pinter, P. J., Hipps, L. E., et al. (1994). Surface energy balance estimates at local and regional scales using optical remote sensing from an aircraft platform and atmospheric data collected over semiarid rangelands. *Water Resources Research*, *30*(5), 1241–1259.

Kustas, W. P., Li, F., Jackson, T. J., Prueger, J. H., MacPherson, J. I., & Wolde, M. (2004). Effects of remote sensing pixel resolution on modeled energy flux variability of croplands in Iowa. *Remote Sensing of Environment*, *92*(4), 535–547.

Kustas, W. P., Anderson, M. C., Alfieri, J. G., Knipppper, K., Torres-Rua, A., Parry, C. K., et al. (2018). The grape remote sensing atmospheric profile and evapotranspiration experiment. *Bulletin of the American Meteorological Society*, *99*(9), 1791–1812.

Liaghat, S., & Balasundram, S. K. (2010). A review: The role of remote sensing in precision agriculture. *American Journal of Agricultural and Biological Science*, *5*(1), 50–55.

Li, F., Kustas, W. P., Anderson, M. C., Prueger, J. H., & Scott, R. L. (2008). Effect of remote sensing spatial resolution on interpreting tower-based flux observations. *Remote Sensing of Environment*, *112*, 337–349.

Liou, Y. A., & Kar, S. K. (2014). Evapotranspiration estimation with remote sensing and various surface energy balance algorithms-a review. *Energies*, *7*(5), 2821–2849.

Magalhães, P. S. G., Sanches, G. M., Molin, J. P., Portz, G., Amaral, L., Kolln, O. T., & Duft, D. G. (2013). Potential solution to contribute for sugar cane spatial variability management. *EFITA-WCCACIGR Conference "Sustainable Agriculture through ICT Innovation", Turin, Italy*, (May 2014), 24–27.

Manfreda, S., McCabe, M. F., Miller, P. E., Lucas, R., Madrigal, V. P., Mallinis, G., et al. (2018). On the use of unmanned aerial systems for environmental monitoring. *Remote Sensing*, *10*(4), 641.

Martineli Sanches, G., Duft, D. G., Kölln, O. T., Luciano, A. C. dos S., De Castro, S. G. Q., Okuno, F. M., & Franco, H. C. J. (2018). The potential for RGB images

obtained using unmanned aerial vehicle to assess and predict yield in sugarcane fields. *International Journal of Remote Sensing*, *00*(00), 1–13. doi:10.1080/01431161.2018.1448484

Matese, A., Toscano, P., Di Gennaro, S. F., Genesio, L., Vaccari, F. P., Primicerio, J., et al. (2015). Intercomparison of UAV, aircraft and satellite remote sensing platforms for precision viticulture. *Remote Sensing*, *7*(3), 2971–2990.

McCabe, M. F., & Wood, E. F. (2006). Scale influences on the remote estimation of evapotranspiration using multiple satellite sensors. *Remote Sensing of Environment*, *105*(4), 271–285.

McCabe, M. F., Rodell, M., Alsdorf, D. E., Miralles, D. G., Uijlenhoet, R., Wagner, W., et al. (2017). The future of Earth observation in hydrology. *Hydrology and Earth System Sciences*, *21*(7), 3879–3914. doi:10.5194/hess-21-3879-2017

McKee, M. (2017). The remote sensing data from your UAV probably isn't scientific, but it should be! *Autonomous Air and Ground Sensing Systems for Agricultural Optimization and Phenotyping II*, *10218*, 102180M.

Moran, M. S., & Jackson, R. J. (1991). Assessing the spatial distribution of evapotranspiration using remotely sensed inputs. *Journal of Environmental Quality*, *20*, 525–537.

National Research Council (1997). *Precision Agriculture in the 21st Century: Geospatial and Information Technologies in Crop Management*. Washington D.C.: The National Academic Press.

Nawar, S., Corstanje, R., Halcro, G., Mulla, D., & Mouazen, A. M. (2017). *Delineation of Soil Management Zones for Variable-Rate Fertilization: A Review*. *Advances in Agronomy* (1st ed., Vol. 143). Elsevier Inc.

Norman, J. M., Kustas, W. P., Prueger, J. H., & Diak, G. R. (2000). Surface flux estimation using radiometric temperature: A dual-temperature-difference method to minimize measurement errors. *Water Resources Research*, *36*(8), 2263–2274.

Ortega-Farías, S., Ortega-Salazar, S., Poblete, T., Kilic, A., Allen, R., Poblete-Echeverría, C., et al. (2016). Estimation of energy balance components over a drip-irrigated olive orchard using thermal and multispectral cameras placed on a helicopter-based unmanned aerial vehicle (UAV). *Remote Sensing*, *8*(638), 1–18.

Pierce, F., & Novak, P. (1999). Aspects of precision agriculture. *Advances in Agronomy*, *67*, 1–85.

Pinter Jr., P. J., Hatfield, J. L., Schepers, J. S., Barnes, E. M., Moran, M. S., Daughtry, C. S. T., & Upchurch, D. R. (2003). Remote sensing for crop management. *Photogrammetric Engineering and Remote Sensing*, *69*(6), 647–664.

Price, J. C. (1990). U sing Spatial Context in Satellite Data to Infer Regional Scale Evapotranspiration. *IEEE Transactions on Geoscience and Remote Sensing*, *28*(5), 940–948.

Qadir, M., Boers, T. M., Schubert, S., Ghafoor, A., & Murtaza, G. (2003). Agricultural water management in water-starved countries: Challenges and opportunities. *Agricultural Water Management*, *62*(3), 165–185.

Ribeiro-Gomes, K., Hernández-López, D., Ortega, J. F., Ballesteros, R., Poblete, T., & Moreno, M. A. (2017). Uncooled thermal camera calibration and optimization of the photogrammetry process for UAV applications in agriculture. *Sensors (Switzerland)*, *17*(10), 9–11.

Rouze, G., Neely, H. L., Morgan, C., & Yang, C. (2018). Spatial analysis of multispectral and thermal imagery from multiple platforms. In J. A. Thomasson, M. McKee, & M. R. J. (Eds.), *Proc. SPIE 10664 Autonomous Air and Ground Sensing Systems for Agricultural Optimization and Phenotyping III* (pp. 1–11). Orlando, FL.

Sanches, G. M., Duft, D. G., Kölln, O. T., Luciano, A. C. dos S., De Castro, S. G. Q., Okuno, F. M., & Franco, H. C. J. (2018). The potential for RGB images obtained using unmanned aerial vehicle to assess and predict yield in sugarcane fields. *International Journal of Remote Sensing*, *00*(00), 1–13.

Sankaran, S., Khot, L. R., Espinoza, C. Z., Jarolmasjed, S., Sathuvalli, V. R., Vandemark, G. J., et al. (2015). Low-altitude, high-resolution aerial imaging systems for row and field crop phenotyping: A review. *European Journal of Agronomy*, *70*, 112–123.

Schimmelpfennig, D. (2016). Farm Profits and Adoption of Precision Agriculture. *Economic Research Report*, (217), 46.

Shannon, D. K., Clay, D. E., & Sudduth, K. A. (2018). An Introduction to precision agriculture. In D. K. Shannon, D. E. Clay, & K. A. Sudduth (Eds.), *Precision Agriculture Basics* (pp. 1–12). Madison, Wisconsin: Soil Science Society of America.

Sona, G., Passoni, D., Pinto, L., Pagliari, D., Masseroni, D., Ortuani, B., & Facchi, A. (2016). UAV multispectral survey to map soil and crop for precision farming applications. *International Archives of the Photogrammetry, Remote Sensing and*

Spatial Information Sciences - ISPRS Archives, *2016-January*, 1023–1029. doi:10.5194/isprsarchives-XLI-B1-1023-2016

Stanislav, S. (2010). *A field-scale assessment of soil-specific seeding rates to optimize yield factors and water use in cotton. Masters Thesis.* Texas A&M University.

Stoorvogel, J. J., Kooistra, L., & Bouma, J. (2015). Managing soil variability at difference spatial scales as a basis for precision agriculture. In R. Lal & B. A. Stewart (Eds.), *Soil-Specific Farming: Precision Agriculture* (pp. 37–72). Boca Raton, FL: CRC Press.

Sudduth, K. ., Kitchen, N. ., Wiebold, W. ., Batchelor, W. ., Bollero, G. ., Bullock, D. ., et al. (2005). Relating apparent electrical conductivity to soil properties across the north-central USA. *Computers and Electronics in Agriculture*, *46*, 263–283.

Sui, R., & Yan, H. (2017). Field Study of Variable Rate Irrigation Management in Humid Climates. *Irrigation and Drainage*, *66*(3), 327–339.

Verstraeten, W. W., Veroustraete, F., & Feyen, J. (2008). Assessment of evapotranspiration and soil moisture content across different scales of observation. *Sensors*, *8*, 70–117.

Viscarra Rossel, R. A., Adamchuk, V. I., Sudduth, K. A., McKenzie, N. J., & Lobsey, C. (2011). *Proximal Soil Sensing. An Effective Approach for Soil Measurements in Space and Time*. *Advances in Agronomy* (Vol. 113). Elsevier Inc.

Whelan, B. M., & McBratney, A. B. (2000). The "null hypothesis" of precision agriculture management. *Precision Agriculture*, *2*(3), 265–279.

Whelan, B., & Taylor, J. (2013). Yield variability and site-specific crop management. In *Precision Agriculture for Grain Production Systems*. CSIRO Publishing.

World Meteorological Organization (2014). *Guide to Instruments and Methods of Observation*. Geneva, Switzerland.

Xia, T., Kustas, W. P., Anderson, M. C., Alfieri, J. G., Gao, F., McKee, L., et al. (2016). Mapping evapotranspiration with high-resolution aircraft imagery over vineyards using one-and two-source modeling schemes. *Hydrology and Earth System Sciences*, *20*, 1523–1545.

2. EVALUATING UNMANNED AERIAL VEHICLE (UAV) IMAGERY AS AN ALTERNATIVE TOOL TOWARDS COTTON SITE-SPECIFIC MANAGEMENT

2.1. Introduction

Achieving longevity for future generations requires sustainable farming decisions be made in the present. Such goals have been addressed with precision agriculture equipment, beginning around the 1990s. For example, chlorophyll/greenness sensors were designed to monitor crop conditions within a growing season, which can help save money and produce less environmental waste (Blackmer, 1995). This technology has continued to show usefulness in part because its data is georeferenced GPS (Ahmad et al., 1999; Taskos et al., 2015). Transitioning into the twenty-first century, GPS has also been integrated with sensors that use concepts of electromagnetic induction (EMI) to measure EC_a (e.g. Veris®, EM-38®). A recent survey by Erickson et al. (2017) indicates that EC_a sensors, relatively speaking, remain popular within industry. For example, 22 % of central USA precision agriculture dealers (as of 2017) are using soil EC_a mapping in some capacity, while less than 10 % of dealers are using chlorophyll/greenness sensors. EC_a also remains popular within academia, as evidenced by the steady production of literature reviews on the topic (Rhoades et al., 1989; McNeill, 1992; Corwin and Lesch, 2005; Corwin and Scudiero, 2016). One reason why EC_a sensors remain popular across both industry and academia is because it can map soil properties across space and time, such as clay content and water holding capacity (Adamchuk et al., 2004).

One proposed application of EC_a beyond soil mapping includes MZ delineation (Lund et al., 1999). A MZ is a sub-region within a field that exhibits a relatively homogenous set of factors directly or indirectly related with yield, such as biomass and plant height (Schepers et al., 2004; Marino and Alvino, 2018). However, EC_a-based MZs have been critiqued for several reasons. First, interpreting EC_a signals within low-medium saline environments (0-200 mS m^{-1}) can be challenging, as several soil properties are likely to influence EC_a signals (Corwin and Scudiero, 2016). Second, EC_a signals are not directly tied with crop behavior within a growing season (Corwin and Lesch, 2003). Lastly, EC_a measurements can be inconsistent predictors of yield because of confounding influences beyond the soil medium, such as the weather (Guo et al., 2018).

UAVs may serve as a potential alternative to EC_a for MZ delineation. This is because its measurements can characterize yield-related factors, and its data collection is relatively flexible and cheap (Shi et al., 2016). UAVs have three application areas: 1) crop scouting, 2) monitoring to prevent yield losses, and 3) planning crop management operations, such variable rate fertilization (Hunt Jr. and Daughtry, 2017). UAVs are equipped with sensors or cameras that visually depict object behavior within a production field. For example, multispectral sensors generate images containing information on soil and crop reflectance, using visible (red, green, blue bands or RGB) and near-infrared (or NIR) regions of the electromagnetic spectrum (~400-1000 nm) (Zhou et al., 2017; Manfreda et al., 2018). Crop growth indicators, such as the Normalized Difference Vegetative Index (NDVI) (Rouse et al., 1974), for example, are

then created by combining several (e.g. red + NIR) bands that exhibit sharply contrasting vegetation reflectance patterns.

Studies have only recently addressed UAVs and their associated indicators towards MZ applications. NDVI and RGB imagery, for example, have been used to create MZs within a wine grape vineyard (Matese et al., 2017; Padua et al., 2018). Thermal cameras (7–14 μm), using radiometric surface temperature (or T_r), have also been used to model MZs based on water stress signatures within date-palm orchards (Cohen et al., 2017). While UAV MZs have shown favor within these high value crops, few studies have addressed the suitability of UAV-based MZs within row crops. Cotton, for example, is an important row crop because it has many uses - one cotton bale (227 kg) can make up to 215 pairs of jeans, 1,200 t-shirts, and 680,000 cotton balls (Cotton Australia, 2018). Recent estimates suggest global cotton consumption to be 120.5 million bales in 2017/2018, its highest since 2007/2008 (Johnson et al., 2018). Cotton is an economic staple in many regions of the United States, such as Texas, contributing about $3.3 billion to the state in 2018 (U.S. Census Bureau Trade Data, 2018). Recent UAV-based cotton studies have focused on applications such as: 1) ground cover estimation (Duan et al., 2017), 2) plant protection (Lou et al., 2018), and 3) germination monitoring (Chen et al., 2018). To the authors' knowledge, however, UAVs have not been used to model cotton based MZs, particularly at different points before and during a growing season.

The purpose of this study was to evaluate UAVs, relative to EC_a, in terms of their ability to generate cotton based MZs. The study was conducted within a field where past yields were affected by soil texture and, thus, water holding capacity. MZs were

delineated using various UAV sensors (i.e. multispectral, thermal, RGB) at different points before and within a growing season. In-season MZ traits such as canopy height were modelled using information from all three sensors via ordinary least squares regression. Height and yield were also used to address the distinctness of two sub-regions created within the field. UAV MZs were then compared with MZs previously established by soil EC_a using analysis of variance (ANOVA) tests. The question that drives the ANOVA models is the relative importance of each layer - to what extent is the other layer needed to create MZs?

2.2. Methods

2.2.1. Field location and crop management

The study site (17-ha cotton field) is located on the Texas A&M Experimental Farm, located near central-eastern Texas (30.531° N, 96.430° W) (Fig. 2.1a). The soils are currently forming under alluvial parent materials. Soil surface textures sampled in the area include silt loam, silty clay loam and silty clay (Fig. 2.1b). The range in clay content is from 210-530 g kg^{-1}, a difference of 320 g kg^{-1} (Fig. 2.1b). Clay content distribution is positively skewed (0.25), with a median clay content of 335 g kg^{-1}. Elevations are relatively constant, with an average elevation of 67.7 ± 0.3 m above ground level or AGL (based on 2017 UAV digital surface models, Sect. 2.2.3.3). Growing season precipitation was 1248 mm. A heavy rain event (65.8 mm) occurred during cotton planting and emergence, resulting in soil crusting (Fig. 2.1a) and some poor stands. The cotton plants experienced some particularly hot days – about a third of

the time, the daily maximum temperatures were greater than the upper threshold for optimal growth (37.8 °C).

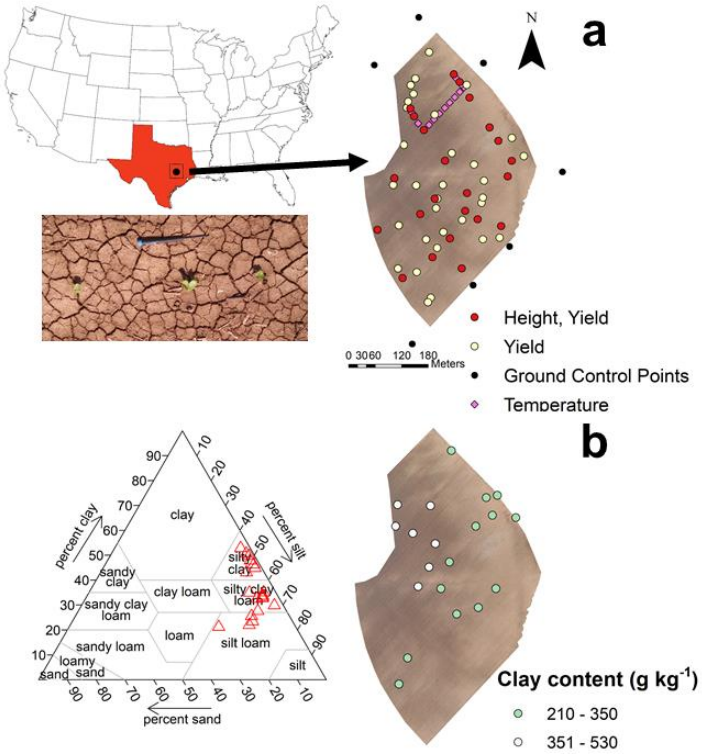

Fig. 2.1 (a) Site location, along with locations of ground control points (black) and field measurements (yellow, red, pink) taken throughout the 2017 field season. In-season canopy height measurements were collected at the red circles on July 1, July 13, and July 28 (Table 2.1). Temperature measurements were collected at pink diamonds during the UAV thermal surveys on July 13 and July 28. End-of-season yield and height measurements were collected at the yellow and red circles around September 26. The field photograph (blue screwdriver for scale, top) shows soil cracks that emerged from an early rain event (six days after planting or DAP). (b) Particle-size distribution data collected from near-surface samples (0–0.3 m depth, left), as well as their spatial distribution (right). The soil texture classes are defined using the USDA classification system.

The field was actively managed with conventional tillage practices with a crop rotation of corn (*Zea mays L.*) and cotton (*Gossypium hirsutum L.*). In 2017, a cotton variety (PHY 444 WRF) was planted at a rate of 111,200 seeds ha^{-1} and 1.02 m row spacing on April 5, 2017 (DOY 95). Pre-emerge and post-emergence herbicides (Prowl H2O, Cotoran 4L, Cornerstone Plus) were applied to ensure uniform stand establishment. In-season management of cotton included fertilization, plant growth regulation, and weed control. Cotton was irrigated using a center-pivot sprinkler system (Lindsay Corporation, Omaha, NE, USA[1]), and each irrigation event applied water at a depth of 21.5 mm. Irrigation water was applied on May 4 (29 days after planting or DAP), June 28 (84 DAP), July 19 (105 DAP), and July 21 (107 DAP). Due to the large field size, each irrigation event lasted about 2.5 days. Cotton harvest was slightly delayed due to regrowth caused by adequate water resources via Hurricane Harvey (513 mm, August 26-28, 2017); as a result, harvesting commenced on October 14, 2017 (192 DAP). Based on field observations, first flowering was observed on June 8 (64 DAP), with cutout (i.e. five nodes above white flower or NAWF) observed on July 1, 2017. Boll filling occurred approximately between June 29 and July 28 (85-112 DAP). Open bolls for about 90 % of the field occurred around September 1 (210 DAP).

2.2.2. Soil and agronomic sampling

Agronomic data collected on each UAV survey date included canopy height and yield. Height and yield sampling locations were established using EC_a raw sampling points (see Sect. 2.2.3.1. below), under a stratified random sampling design. On the day of a given UAV survey (Table 2.1), plant height measurements, due to limited resources,

were collected at select locations (Fig. 2.1a, red dots, n = 23). At the end of the season, yield and height measurements were obtained from additional sampling locations between September 18-19, 2017 (Fig. 2.1a, red and yellow dots, n = 55). Yield measurements were collected within a 3 x 3 (9 m^2) sampling area around each point. Samples were then brought back to the laboratory and seed cotton yield measurements were obtained. Canopy height was used as an in-season yield trait because it was a significant predictor of yield (Fig. 2.2). The height of a cotton plant affects yield by the addition of branching sites via nodes and internodes at the top of the plant (Hake, 1989).

Table 2.1 List of UAV surveys, along with physiological stage and field average LAI values during the 2017 field season. Field average LAI values were obtained at select points (Fig. 2.1a, red) using an LAI-2200C sensor (LI-COR, Lincoln, USA), with details described elsewhere (Rouze et al., in preparation). Abbreviations: DAP – Days After Planting; GDD – Growing Degree Days; NAWF – Nodes Above White Flower; RGB – Visible Sony A6000 camera; MS – Multispectral MicaSense RedEdge sensor; TH – Thermal ICI 8640-P sensor.

Growth Stage	Date	DAP	Sensor	Variable	Survey Time	Pixel resolution (m)	LAI (m^2 m^{-2})	GDD	NAWF
Pre-planting	March 22	N/A	RGB	Soil color	9:56-10:10	0.03	N/A	0	N/A
Flowering	July 1	87	MS	NDVI	12:05-12:27	0.08	1.72	1545	5
Boll filling	July 13	99	TH	T_r	14:54-15:06	0.15	2.21	1875	3
	July 28	114	TH	T_r	14:46-15:00	0.15	2.37	2305	2
Open boll	September 26	174	RGB	Open bolls	11:21-11:39	0.03	N/A	3742	0

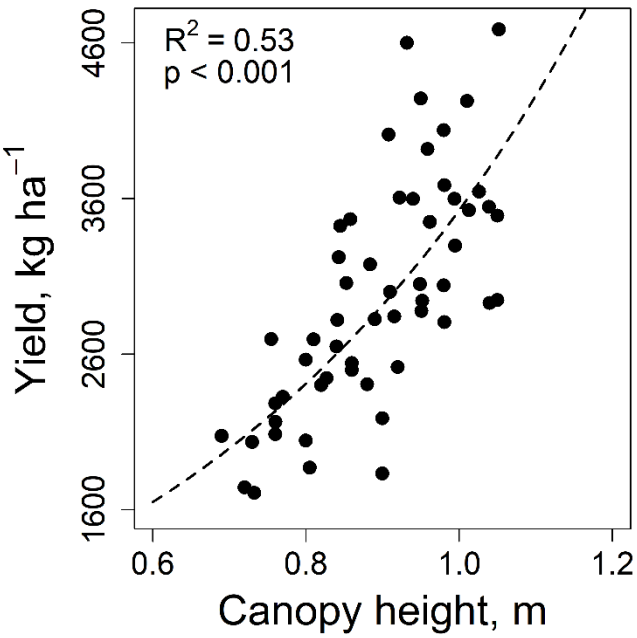

Fig. 2.2 End-of-season seed-cotton yield plotted against canopy height (Fig. 2.1a, red + yellow circles).

2.2.3. Sensor data collection and preparation

2.2.3.1. EC_a data

An EMI survey was conducted over a bare soil field on December 31, 2007 using an EM38DD sensor (Geonics Limited, Ontario, Canada). In EMI, primary electromagnetic currents generated by a transmitter coil are induced into the soil, and the soil produces secondary magnetic currents that are recognized by a receiver coil; the ratio between the primary and secondary currents collected at the receiving coil is a linear function of EC_a (McNeil, 1980). Temperature drift of EC_a readings was minimized by placing a sunshield over the instrument (Robinson et al., 2004). Transects were spaced approximately ten meters apart, and each measurement was tagged with spatial coordinates using an integrated Trimble AG 114 GPS system (Trimble Inc., Sunnydale,

CA, USA). Coordinates were defined using a projected coordinate system (WGS 84/UTM Zone 14 N or EPSG: 32614). EC_a measurements from vertical and horizontal dipole modes were logged every second, corresponding with effective measurement depths of 1.50 and 0.75 m, respectively (McNeill, 1992). The vertical dipole mode was chosen for this study because its measurement depth corresponds with commonly reported cotton root zone depths (Allen et al., 1998). While EC_a is a function of several soil properties such as salinity, water content, organic matter, and cation exchange capacity (Corwin and Scudiero, 2016), the EC_a data collected in this field has previously shown strong correlations with clay content ($R^2 = 0.86$, $p < 0.01$) and, thus, soil water holding capacity (Stanislav, 2010). Interpolated soil EC_a values (Sect. 2.2.3.1.) were extracted at each sampling location (Fig. 2.1a) for later height and yield modeling.

Raw EC_a survey data were then processed into field MZs. EC_a post-processing began by first discarding raw EC_a sampling points located five meters from the boundary edge. The protocol outlined by Cordoba et al. (2016) was then adopted, which includes the following steps: 1) removal of outliers and inliers, 2) spatial interpolation, 3) classification, and 4) smoothing of classification values. All MZ delineation was performed by adapting R scripts (R Core Development Team, 2018) supplied by Cordoba et al. (2016). A Gaussian model (effective range = 293 m; nugget to sill ratio = 2.9 %) was fit to an empirical semi-variogram, and predictions were block kriged onto a three-meter grid. To reduce computation time, only samples located within 30 m at each prediction node were considered. A three-meter grid was selected based on the inter-measurement sample distance, as well as previous recommendations for reliable yield

estimation (Mulla et al., 2013). Two MZs were used to classify the interpolated data EC_a using an unsupervised k-means algorithm. Two zones were selected using expert knowledge of the field, as well as recommendations from a host of Euclidean distance-based clustering algorithms (Charrad et al., 2014).

2.2.3.2. UAV system and flights

Table 2.1 shows dates when UAV surveys (and their respective sensors) were flown over the field throughout the 2017 cotton season. Table 2.2 describes the technical details of the individual cameras. The main stages selected for this study include pre-planting, flowering, boll filling, and open bolls. A pre-planting RGB survey was conducted from previous findings that bare-soil aerial imagery could be used to create pre-season MZs (Fleming et al., 2004). RGB images were collected from a Sony A6000 camera (Minato, Tokyo, Japan), and multispectral images were collected from a MicaSense RedEdge camera (Seattle, WA, USA). Unlike the A6000, which measures spectral luminance (units of Lumens sr^{-1} m^{-2}), the RedEdge measures spectral brightness or radiance (W sr^{-1} m^{-2}). Thermal images were collected using an ICI 8640-P sensor (Infrared Cameras Inc., Beaumont, TX, USA).

A6000, RedEdge and ICI 8640-P sensors were integrated were mounted and flown individually on a fixed wing UAV platform (Tuffwing, Boerne, Texas, USA). The fixed wing communicated with a ground control station at a frequency of 915 MHz. All images were instantaneously geotagged using a u-blox M8N GPS module aboard the UAV platform. Flight plans were created within Mission Planner software (ArduPilot Dev Team). The multispectral camera was set under manual settings, with exposure

times ranging between 0.44-1 seconds depending on band. Exposure time for the A6000 was constant at 0.01 seconds. In order to achieve full field coverage in a reasonable time, while minimizing cloud presence, multispectral and visual surveys were flown at 65 % sidelap and overlap, while thermal surveys were flown 60 % sidelap and overlap. All flights (except for pre-planting) were conducted within plus or minus two hours of solar noon, which is defined here as 13:30 (Table 2.1). The average flight time for the thermal, multispectral and RGB imagery was 13, 22, and 16 minutes, respectively. All flights were carried out under clear skies, with a flight altitude of about 120 m AGL, and average winds below 4 m s^{-1}.

Table 2.2 Technical description of UAV sensors utilized in this study.

Characteristics	Visible (RGB)	Multispectral (RGB+NIR)	Thermal
Sensor name	Sony A6000	MicaSense RedEdge	ICI 8640-P
Sensor	CMOS APS-C	CMOS	Uncooled Microbolometer
Resolution (px)	4000x6000	1280x960	640x512
Spectral bands	RGB	RGB/NIR	Long Wave Infrared
Spectral range (nm)	400-700	Blue: 455-495; Green: 540-580; Red-659-678; NIR:800-880	$7000^{-1}4000$
Focal length (mm)	16	5.5	12.5

In order to orient and relate UAV image coordinates to the ground position, ground control points (GCPs) were deployed across the perimeter of the field (Fig. 2.1a, black

points). A GCP consisted of a two-level deck whose spatial coordinates were measured using a Trimble R7/R8 GPS system (Trimble Inc., Sunnydale, CA, USA). Each deck on a given GCP securely housed three radiometric calibration tiles (six tiles per GCP) with known albedo values of 4, 20 and 45 % obtained from a Spectral Evolution PSR+ 3500 spectral radiometer (Haverhill, MA, USA). The radiometric calibration tiles served to later calibrate the UAV multispectral imagery (Sect. 2.2.3.4.). Additional information regarding the GCPs can be found in Han et al. (2018).

2.2.3.3. UAV orthorectification

All imagery was orthomosaiced using Agisoft PhotoScan Pro (St. Petersburg, RU). Orthomosaic generation is based on the structure from motion (SFM) method, which is based on the generation of a digital surface model, given camera positions and calibration parameters. For brevity's sake, the reader is referred to Westoby et al. (2012) for detailed information on the technique. Thermal orthomosaics were aided by aluminized polyester located on the top level of each GCP. Orthomosaics were exported as GeoTIFFs when the RMSE values were less than or equal to 1.5 times the pixel resolution.

2.2.3.4. Multispectral radiometric calibration

Radiometric calibration was performed on multispectral orthomosaics using the empirical line method (Smith and Milton, 1999). In this approach, digital numbers (DNs) acquired from the red and NIR bands were converted into percent reflectance using the three calibration tiles. For the red band, it was observed that crop DNs were lower than that of the four percent albedo target, resulting in erroneously negative reflectance

values. To get around this issue, a new low-end reflectance point within the red band was established within nearby tree shadows at two percent reflectance (Pristolas et al., 2016). Similar problems were encountered for the NIR band, where crop DNs were higher than the 45 % albedo target. Therefore, a new high-end reflectance point was established using the GCP plywood material, measured at 79 % reflectance.

Quality control on this approach was performed by comparing the estimated red and NIR reflectance values with those from other calibration tiles. In this comparison, reflectance values agreed well with independent ground-truth measurements, with a bias of 0.5 % and RMSE of 2.5 %. This accuracy is similar, if not lower, reported errors by Berni et al. (2009) and Xia et al. (2016). The calibrated red and NIR bands were then used to estimate the NDVI. NDVI uses red (ρ_{Red}) and NIR (ρ_{NIR}) reflectance using Eq. 2.1:

$$NDVI = \frac{\rho_{NIR} - \rho_{Red}}{\rho_{NIR} + \rho_{Red}} \quad \text{(Eq. 2.1)}$$

2.2.3.5. Thermal radiometric correction

Thermal images collected by the ICI 8640-P were first processed from 8-bit DNs or radiance to 16-bit camera calibrated brightness temperature (T_{br}) using the provided software (IRFlash 2.16.4.21). T_{br} is not the same as T_r, the variable of interest, as the former contain sources of uncertainty such as atmospheric attenuation and differences in land surface emissivity (ε) (Torres Rua et al., 2017). T_r can be estimated from T_{br} at each i^{th} pixel, given ε and the background air temperature (T_{bg}) (Maes and Steppe, 2012):

$$T_{r,i} = \sqrt[4]{\frac{T_{br,i}^4 - (1-\varepsilon)T_{bg}^4}{\varepsilon_i}} \quad \text{(Eq. 2.2)}$$

Because soil and vegetation pixels were visible from thermal images at all points in time, and because these two objects were found to exhibit different emissivity values from field measurements, spatially distributed ε was needed to derive accurate T_r (Eq. 2.2). ε was calculated at each i^{th} pixel, therefore, by weighting soil and vegetation emissivity values (ε_s and ε_v, respectively) by the vegetation fraction cover (f_c) (Jimenez-Munoz et al., 2006):

$$\varepsilon_i = \varepsilon_s(1 - f_{c,i}) + \varepsilon_v f_{c.i} \quad \text{(Eq. 2.3)}$$

where ε_s was 0.96 as obtained from a box method (Fuchs and Tanner, 1966), and ε_v was set to 0.99, per recommendations from Maes and Steppe (2012). $f_{c,i}$ was derived from NDVI imagery by scaling between 'infinite' NDVI ($NDVI_\infty$) and soil NDVI ($NDVI_s$) (Carlson and Ripley, 1997):

$$f_c = \left(\frac{NDVI - NDVI_s}{NDVI_\infty - NDVI_s}\right)^2 \quad \text{(Eq. 2.4)}$$

$NDVI_\infty$ was taken to be the maximum NDVI observed from the original spatial resolution (0.976). $NDVI_s$ was based off an average bare soil NDVI using UAV imagery collected before cotton squaring (0.2). T_{bg} (Eq. 2.2) was found using air temperature data from an HC2S3 temperature probe (Campbell Scientific, Logan, UT, USA).

Validation for the thermal correction approach above was assessed by comparing predicted and measured T_r obtained from vegetated and bare soil surfaces during thermal image collection (Fig. 2.1a, pink diamonds). Predicted temperatures were computed by first aggregating up to the field-of-view of the infrared thermography (IRT) sensor

(around 0.08 m^2). Predicted canopy and soil temperatures were obtained by extracting the minimum and maximum temperatures within the approximate measurement area (3 m radius). MAE values of 2.9 and 4.4 °C and mean biases (predicted-measured) of -0.2 and -3.4 °C were found for plants and soils, respectively. One possible source of error using this validation approach lies within the different spectral ranges between the ground thermal sensor (i.e. MI-220) and the aerial thermal sensor (i.e. ICI-8640 P) (8-14 μm and 7-14 μm, respectively).

2.2.3.6. Open boll generation

In addition to NDVI and T_r, an additional variable or indicator was developed for MZ delineation, this time using RGB imagery around open boll growth stage (Sep. 26, Table 2.1). The primary objective of the algorithm was to create a yield-like map based on open boll detection, with the objective to discriminate open bolls against the background (i.e. soil, defoliated leaves, stem branches). To do this, a red/blue ratio map was developed, with a threshold less than 1.13 identified as an open boll. The hypothesis here is that open cotton bolls, being white, will have similar luminance values across all RGB bands, while background components will not. Therefore, there should exist some threshold that can be used to extract the signal (i.e. bolls) from the noise (i.e. non-bolls). This approach is like the Otsu algorithm, except threshold values are automatically determined within each band (Yeom et al., 2018). However, a manual threshold approach was selected in this study because the luminance distributions across all bands were not bimodal, a key assumption of the Otsu algorithm. After boll detection, the red/blue ratio map was reclassified to a binary image (open/absent boll) based on the

established threshold (1.13) - Fig. 2.3 shows the result of this technique applied over a portion of the field.

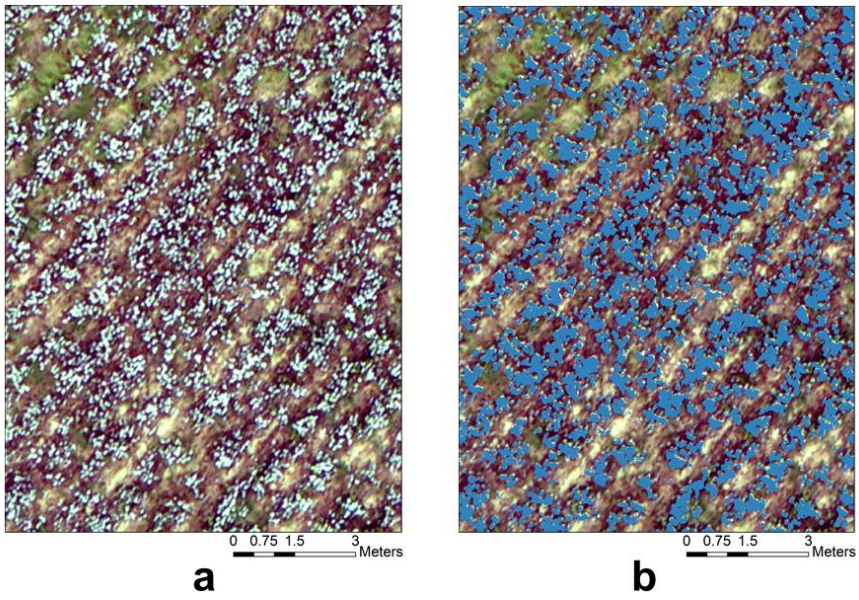

Fig. 2.3 (a) Geographical subset of RGB UAV survey conducted on September 26, 2017; (b) result of open boll methodology, with open bolls (in blue) overlaying the image from Fig. 2.3a.

2.2.3.7. UAV management zone creation

NDVI, T_r and open boll orthomosaics were used to delineate MZs from the selected survey dates from Table 2.1. UAV pixels located five meters from the boundary edges were first removed. NDVI and T_r imagery were aggregated to the nearest multiple of three meters (i.e. the EC_a pixel resolution) using an arithmetic mean. NDVI and T_r aggregated pixels represent, therefore, a mixture of soil and canopy pixels depending on vegetation fraction cover. Open boll count imagery was also aggregated to the nearest

multiple spatial resolution to three meters, but a summation (instead of mean) operation was performed. Thus, each pixel represents the number of counted open bolls within a square area of 9 m^2. Two zones or classes were defined for consistent comparison with EC_a MZs. For the pre-planting orthomosaic (Fig. 2.1a), a maximum likelihood supervised classification scheme was performed across all bands within ArcGIS 10.6.1 (ESRI, Redlands, USA). For all other UAV layers, unsupervised k-means algorithm was applied on the pixel values using the k-means base function within R. All UAV raster maps were reclassified based on the two pixel clusters, and a three meter smoothing filter was similarly applied as with the EC_a MZs.

2.2.3.8. Statistical analysis

To facilitate regression modeling, aggregated UAV values (i.e. NDVI, T_r) and zone clusters were extracted at each sampling location (Fig. 2.1a, red and yellow circles). A different procedure was performed for the open boll count map, as yield samples were unfortunately collected before the UAV RGB survey (Table 2.1). At each sample location an erase operation was performed, whereby a spatial polygon was created from an outer buffer (4 meters) and an inner buffer (3 meters) - all pixels that fell within this outer ring were extracted and used in the boll counting process.

UAV MZs were first assessed by predicting canopy height from in-season UAV layers (i.e. July 1 NDVI, July 13 T_r, July 28 T_r) using ordinary least squares (OLS) regression. Similarly, yield was also predicted using the bolls counted within each of the outer rings as described above. Regression validation was performed for all models, including checks for heteroskedasticity (residual plots, Bresuch-Pagan tests) and spatial

autocorrelation. Linear models were then assessed for quality of fit in terms of R^2, RMSE, MAE and p-values.

Validation of delineated regions within each MZ was determined using randomization methods. The purpose of MZ validation is to determine if the two delineated MZs present significant statistical differences with respect to yield related attributes. Randomization tests were preferred over more commonly used ANOVA tests, as significant spatial autocorrelation was observed from height and yield samples ($p = 0.048$ and $p = 0.006$, respectively) - such spatial autocorrelation, if present, will violate spatial independence assumptions from ANOVA tests (Tisseyre and Leroux, 2017). Randomization approaches are most appropriate when sample sizes are too small (i.e. less than 100) to conduct a reliable semivariogram (Webster and Oliver, 1992) - the sample size for height was 23 on July 1 and July 13, and 55 on July 28. The sample size for yield was 55 on September 26. The following paragraph provides details on the randomization test used in this study.

The general premise of the randomization approach is to test whether it is better to classify the field into random MZs, or to use the k-mean based UAV MZs. To perform this test, an observed F-statistic (F_{obs}) was first calculated from an ANOVA model, with the y-variable being the agronomic variable of interest (i.e. canopy height/yield), and the x-variable being the set of UAV MZ classes extracted at each site (Fig. 2.1a). F_{obs} was then compared with a random set of F-statistic values (F_{rand}). F_{rand} was determined by first randomly assigning zones to all aggregated raster pixels, followed by extraction of these zones at the same sampling locations. After class extraction, an ANOVA was

performed, with the y-variable again being the agronomic variable of interest (i.e. canopy height/yield), but the x-variable now being the random MZ extracted at each site. The result of this ANOVA model is F_{rand}, and this procedure was repeated for a total of 1500 iterations. A randomization p-value was then calculated as: : $\frac{(\text{the \# of times } F_{rand} > F_{obs})}{1500\ iterations}$. Statistical tests were deemed significant if the p-value was less than 0.05.

In addition to regression and randomization techniques, ANOVA tests were conducted to address the value of adding EC_a to UAV data, or vice-versa. In other words, how important is it to include both EC_a and UAV layers in MZ delineation? Four models were constructed:

- Yield was predicted from EC_a only (model 1);
- Yield was predicted from an optimal set of UAV layers (Table 2.1) using stepwise backwards regression (model 2);
- Yield was predicted from both EC_a and an interaction term between the optimal set of UAV layers and EC_a (model 3);
- Yield was predicted from both UAV and the same interaction term from model 3 (model 4).

An interaction term was added to models 3 and 4 based on the theory that crop yields are a function of interactions between soil (i.e. EC_a) and crop (i.e. UAV) information. The ANOVA models were constructed to test the significance of this interaction term (i.e. model 1 vs. model 3, model 2 vs. model 4). ANOVA models were deemed adequate here because spatial autocorrelation was not present from model residuals ($p > 0.05$).

In addition to ANOVA, the second order Akaike Information Criterion or AIC_c (Hurvich and Tsai, 1989) was used to evaluate the relative quality of fit from the four models above in predicting seed cotton yield. AIC_c was deemed useful here because ANOVA models cannot address model performance, only model difference. AIC_c is

most appropriate when n/k < 40 as was the case here (Burnham and Anderson, 2002). AIC_c aims to balance the fit of a model (or accuracy), model complexity, and sample size using concepts of log-likelihood. AIC_c is defined as:

$$AIC_c = \frac{-2logL(\hat{\theta}) + 2k + (2k+1)}{n-k-1} \quad \text{(Eq. 2.5)}$$

where $L(\hat{\theta})$ is the log-likelihood estimate, *k* is the number of parameters, and *n* is the number of observations. Log-likelihood refers to the probability of obtaining the data, given the candidate model. The relatively best model within this context refers to the model with the lowest AIC_c value.

2.3. Results

2.3.1. Agronomic data

Summary statistics for canopy height and yield are given in Table 2.3, along with yield spatial patterns in Fig. 2.4c. As expected, median canopy heights increased over time due to continued vegetative growth in the month of July (Table 2.3). The skewness of canopy height measurements were negative or left-skewed to some extent. Yield exhibited positive amounts of skew (0.31), and a coefficient of variation (CV) of 24.7 %. The non-normal distributions for canopy height and yield (Table 2.3) are the reason why non-linear regression modeling was needed in this study (ref. 'Statistical Analysis'). Yield values ranged from 1708-4687 kg ha^{-1}, with a median value of 2928 kg ha^{-1}. Many of the high yields (blue circles) are located within zone 2, or the high EC_a region (Fig. 2.4b-2.4c).

Table 2.3 Summary statistics of agronomic (canopy height, yield), EC_a, and UAV layers such as NDVI and T_r. Note that EC_a data and the UAV imagery statistics are from the 3 m aggregated images.

Property	Unit	n	Minimum	Maximum	Mean	Median	Std. Dev.	Skewness
Height-July 1	m	23	0.48	0.73	0.61	0.61	0.07	-0.15
Height-July 13		23	0.56	0.78	0.70	0.71	0.06	-0.46
Height-July 28		23	0.64	0.95	0.80	0.80	0.08	-0.04
Yield	kg ha^{-1}	55	1708	4687	2970	2928	733	0.31
EC_a	mS m^{-1}	3875	17	100	57	57	17	0.11
NDVI-July 1	Kelvin	17141	0.22	0.95	0.69	0.7	0.09	-0.75
T_r-July 13		17367	305	325	312	312	3.2	0.52
T_r-July 28		17507	305	330	315	315	4.1	0.01

2.3.2. EC_a regression modeling and management zone delineation

Regression and MZ results are first presented in terms of EC_a (Table 2.3, Fig. 2.4). EC_a values in Table 2.3 represent the raw survey data after screening for outliers and inliers (about seven percent of data in total). The mean EC_a was 57 ± 18 mS m^{-1} (CV = 0.30), and its distribution was approximately normal, with a skewness of 0.11 (Fig. 2.4a, Table 2.3). The interpolated EC_a map obtained through ordinary block kriging (Fig. 2.4b) indicates soils with relatively high and low EC_a values located on the western and eastern halves of the field, respectively. A once active fluvial channel could explain the observed EC_a spatial distribution (Fig. 2.4b), as clay-sized particles (i.e. relatively high EC_a values), being relatively small, are deposited relatively further from the stream - this hypothesis was partially confirmed with the soil texture data (Fig. 2.1b). Subsequent delineation into two MZs using k-means (Fig. 2.4c) shows that the first zone (white) contains EC_a values between 19.8-57.8 mS m^{-1}, while the second (black) contains EC_a

values between 57.9-96.4 mS m^{-1} (black). About 56 % of the total areas classified into zone 1 (i.e. low EC_a), while 44 % of the field into zone 2 (i.e. high EC_a).

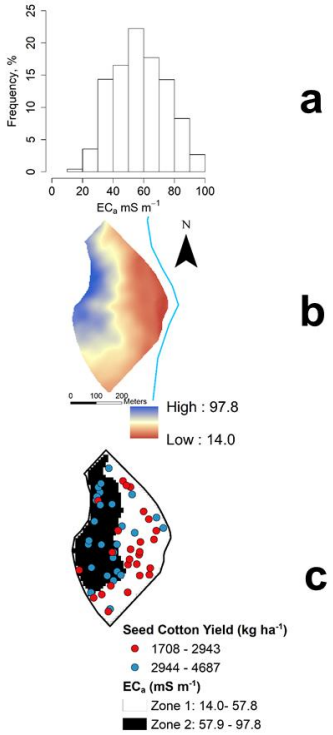

Fig. 2.4 (a) Histogram of EC_a values, along with its density curve in blue (with outliers and inliers removed); (b) ordinary kriged EC_a map, with a continuous color scheme. An abandoned fluvial channel is outlined in blue on the right side of the field; (c) results of k-means classification for the EC_a image in Fig. 2.4b, with low EC_a zones in white and high EC_a zones in black. Seed-cotton yield measurements overlay the EC_a MZ, with low yield areas colored in red, and high yield areas in blue.

Yield modeling was conducted first with EC_a data. The scatterplot between seed cotton yield and EC_a is shown in Fig. 2.5. The addition of other covariates such as elevation via UAV digital surface models did not significantly improve model prediction

and was, therefore, not included in this analysis. The trend between yield and EC_a was positive, but non-linear. The R^2 was low (0.21), but the relationship was statistically significant ($p < 0.001$), based on a log-normal fit. The mean absolute percent error (or MAPE, MAE/μ_{yield}) from the log-normal fit was 18.3 %. The OLS model accounted for the spatial autocorrelation that originally existed within the dataset (residual p-value = 0.47). Previous research in this field (Stanislav, 2010) has shown EC_a to be a significant predictor of yield in past seasons ($R^2 = 0.36$, $p < 0.001$) because it represents yield-limiting factors such as soil water holding capacity.

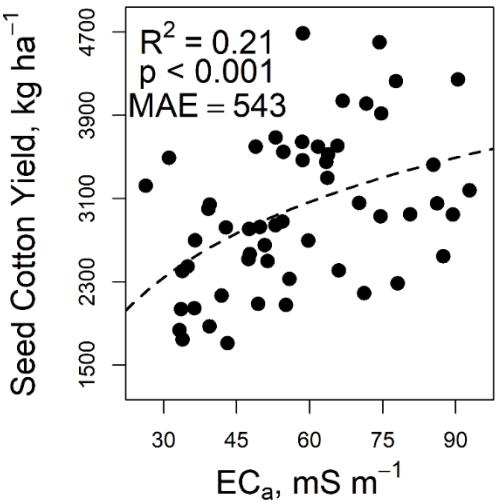

Fig. 2.5 Scatterplot of seed cotton yield (kg ha^{-1}) versus EC_a (mS m^{-1}) for the 2017 field season.

The strength in relationship between EC_a and yield may have been poor for several reasons. Yields may have been affected by poor crop emergence from extreme weather early in the season (Fig. 2.1a). Sampling errors could have also contributed to the low R^2

value, as some of the extreme EC_a values were not sampled (Table 2.3). The EC_a values from collected samples ranged from 26-93 mS m^{-1}, but the range in EC_a across the entire field was between 14-98 mS m^{-1} (Table 2.3, Fig. 2.4a, Fig. 2.5). However, these extreme EC_a values only account for about four percent of the entire dataset (Fig. 2.4a). Considering that a significant relationship was already established between yield and EC_a (Fig. 2.5), therefore, any sampling errors should not significantly change the results above. Therefore, it can be concluded that soil EC_a was a weak predictor of end-of-season cotton yield.

The comparison of end-of-season height and seed cotton yield means (n = 55) within each MZ is shown in Fig. 2.6. Zone 1 refers to the low EC_a zone (Fig. 2.4c, white), while Zone 2 refers to the high EC_a zone (Fig. 2.4c, black). Statistically significant mean differences in canopy height were observed between the two EC_a MZs using the randomization test approach ($p = 0.003$) (Fig. 2.6a). Using EC_a clustering, the mean height values within zones 1 and 2 were 0.86 and 0.93, respectively. In addition to height, seed cotton yield values were significantly different between EC_a MZs using randomization tests ($p < 0.001$, Fig. 2.6b). Using EC_a clustering, the mean yield values within zones 1 and 2 were 2600 and 3382 kg ha^{-1}, respectively. While the regression results (Fig. 2.5) indicate that, while EC_a alone may not be entirely useful in predicting seed cotton yield, it was still able to produce statistically significant MZs in terms of height and yield.

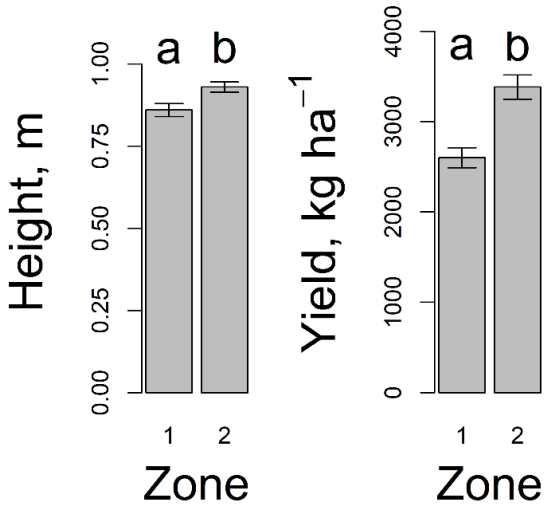

Fig. 2.6 (a) End-of-season canopy height differences based on EC_a zones delineated in Fig. 2.4c; (b) Cotton seed yield differences based on zones delineated in Fig. 2.4c. Different lowercase letters indicate significant differences using randomization tests ($p < 0.05$). The sample size is 55.

2.3.3. UAV regression modeling and management zone delineation

Regression and MZ results are now given in terms of aggregated UAV layers, including NDVI (July 1), T_r (July 13, July 28), and open bolls (September 26). Summary statistics for NDVI and T_r are first given in Table 2.3. The distribution for NDVI and T_r indicates canopy-dominated pixels. For example, the skewness is negative for NDVI on July 1 (-0.75), while T_r is positively skewed on July 13 (0.47). Full vegetation coverage was not entirely reached within the field, so the summary statistics for NDVI and T_r reflect a composite of both soil and vegetation information.

Fig. 2.7 shows scatterplots between in-season canopy height against both NDVI (Fig. 2.7a) and T_r (Fig. 2.7b-2.7c) at various points throughout the growing season. All UAV layers were significant predictors ($p < 0.01$) of canopy height between July 1 to July 28

(Table 2.1). The R^2 values range from 0.53 (July 1) to 0.60 (July 28), and MAE values were between 0.03-0.04 m, with an average MAPE of 5.1 %. NDVI and canopy height were positively correlated and the relationship was quadratic (Fig. 2.7a). On the other hand, T_r trended negatively with canopy height, and the relationship was either linear or cubic (Fig. 2.7b-2.7c) - a cubic model was necessary to ensure homoscedastic residuals.

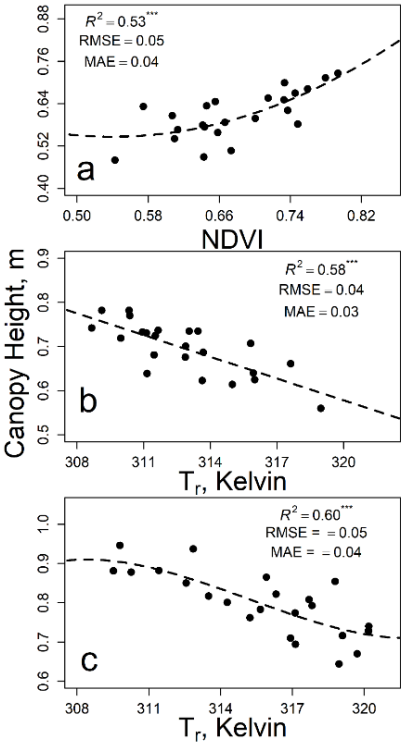

Fig. 2.7 Scatterplots between canopy height and a) NDVI on July 1, b) T_r on July 13, and c) T_r on July 28 (n = 23).

While previous findings have confirmed the utility of the RedEdge camera towards predicting cotton height (Ballester at al., 2017), to our knowledge such findings have not

been extended towards UAV thermal imagery. Canopy height has been shown to affect soil temperatures via shading effects for various vegetation types (Green et al., 1984; Yu et al., 2018). Canopy height can also affect canopy temperatures via plant growth in terms of three potential stress factors, namely nutrients, temperature, and moisture (Hake et al., 1989). While the main stress factor driving this relationship could not be identified in this study, the takeaway message here is that multispectral and thermal sensors were good predictors of yield-related factors such as canopy height (Fig. 2.2), which is a prerequisite for delineating in-season MZs.

The scatterplot between cotton seed yield and RGB open boll count imagery is shown in Fig. 2.8. Note that the open boll count metric used here is only possible after aggregating the RGB imagery up to the target pixel resolution (here 3 m). The relationship was logarithmic and the model was a significant predictor of seed cotton yield (Fig. 2.8). The MAE was 442 kg ha^{-1}, which was 101 kg ha^{-1} lower than the EC_a model (Fig. 2.5). Similarly, the MAPE for the relationship in Fig. 2.8 was 14.9 %, which was 3.4 % lower than that from the EC_a-yield model (Fig. 2.5). While aggregated NDVI and T_r measurements reflect temperatures from canopies and soils, RGB measurements characterize canopies only, specifically the open bolls. The relationship between seed cotton yield and open boll counts may have been degraded because harvest sampling was conducted before the September 26 survey – in other words, the areas selected for boll counting may not be entirely representative of the yield harvested at each sample location. Despite this experimental design error, however, the relationship between the two variables was still significant and even more accurate than EC_a. While Yeom et al.

(2018) recommend RGB spatial resolutions less than one centimeter are required for open boll detection, the results presented here suggest the pixel resolution here (2.80 cm) was adequate, relative to pre-existing techniques.

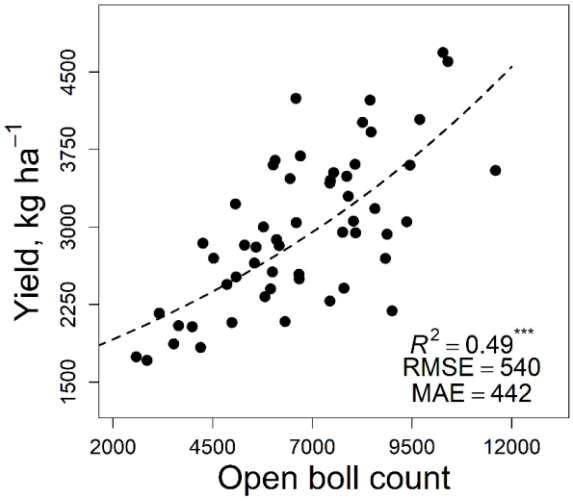

Fig. 2.8 Scatterplots of seed cotton yield versus open boll count from RGB imagery (September 26, n = 55).

The MZs delineated from multispectral (July 1 NDVI), thermal (July 13/July 28 T_r) and RGB (March 22 soil color, September 26 open bolls) sensors are shown in Fig. 2.9. Blue zones in Fig. 2.9 represent relatively high growing areas (Zone 2, Fig. 2.4c), while orange zones the low growing areas (Zone 1). The pre-planting MZ based on soil color (Fig. 2.9a) has similar spatial patterns as the EC_a MZ (Fig. 2.4c). On July 1 (Fig. 2.9b), a large amount of zone 1 (Fig. 2.9b arrow) is located within the clayey soils or the high EC_a region (Fig. 2.4c). The relatively low NDVI response in this region may be

attributed to poor crop emergence due to early season rain events (Fig. 2.1a). On July 13, the areas of low crop productivity have shifted from the high EC_a to areas around the perimeter of the field (arrow in Fig. 2.9b). On July 28, or maximum LAI (Table 2.1), the low zones located around the perimeter of the field have expanded inwards within the field (Fig. 2.9d). The September 26 MZ (Fig. 2.9e) obtained from the open boll map looks very similar to the July 28 T_r MZ, although the former has a greater proportion of Zone 2. In summary, UAV MZ spatial patterns varied from pre-planting to mid- and late-season, with mid-season low zones located within the Zone 2 areas, while late-season shifting towards Zone 1. Fig. 2.9 illustrates the intangible advantages provided by UAVs over EC_a in terms of in-season management. For example, farmers could field scout the areas classified as zone 1 for problems and determine whether such problems can be remedied with management practices.

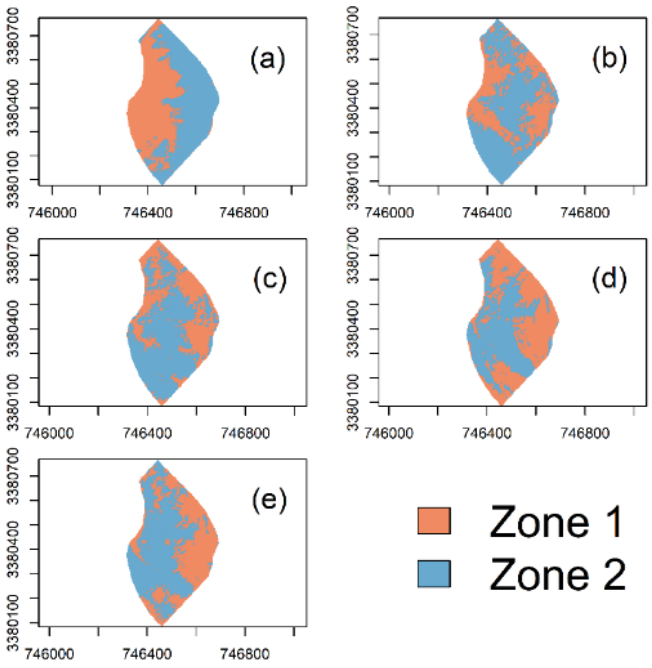

Fig. 2.9 MZs created for a) March 22 bare earth, b) July 1 NDVI, c) July 13 T_r, d) July 28 T_r and e) September 26 open boll count. Fig. 2.9a was made using supervised classification, while Figs. 2.9b-2.9e using unsupervised k-means classification. Black arrows are discussed in the text.

The MZs shown in Fig. 2.9 were furtherly evaluated using AIC_c and randomization tests, and these results are initially presented in Table 2.4. AIC_c values are not reported for in-season canopy height because height varies throughout the season, so model comparisons across dates are not meaningful. With regards to in-season canopy height, the two delineated zones were significantly different from each other using both NDVI and T_r ($p \leq 0.001$). With regards to yield, RGB imagery at pre-planting (i.e. bare soil image) showed significant differences between the two zones ($p = 0.01$). Similarly, the open boll MZs showed significant mean differences in yield ($p < 0.001$), with the mean yields in zones 1 and 2 being 2342 kg ha^{-1} and 3361 kg ha^{-1}, respectively. Furthermore,

the p-value from open boll MZ delineation ($p < 0.001$) was much lower than that from EC_a (0.003).

Table 2.4 Results of randomization p-values, as well as AIC_c values after modeling height or yield as a function of assigned zones.

Date	Layer	P-value	AIC_c
	Height		
July 1 2017	NDVI	0.001	
July 13 2017	T_r	0.001	N/A
July 28 2017	T_r	< 0.001	
	Yield		
March 22 2017	Soil color	0.01	878.5
July 28 2017	T_r	< 0.001	867.5
September 26 2017	Open bolls	< 0.001	866.0
EC_a		0.003	868.5

Table 2.4 shows the AIC_c values in terms of UAV and EC_a MZs. The two delineated EC_a regions were statistically different from each other, thus reiterating the results presented in Fig. 2.6b. A comparison of AIC_c values from the different UAV yield models indicates the best models (in decreasing performance or increasing AIC_c): 1) September 26 and 2) March 22 (866.0 and 878.5, respectively). While the pre-planting UAV RGB orthomosaic performed worse (i.e. higher AIC_c) than the EC_a image (Table 2.4), it still showed significant ($p = 0.01$) differences in separating the field into two sub-regions or MZs, and even produce similar spatial patterns as with EC_a (Fig. 2.4c, Fig. 2.9). Thus, in terms of individual UAV performance, the open boll count image was the best in terms of producing yield-based MZs. The EC_a AIC_c value was lower than the pre-

planting image (868.5). These results indicate that the pre-planting MZ delineation was inadequate relative to EC_a, while the opposite was true for the open boll imagery. However, AIC_c values are only relative and do not address whether these differences (and thus the MZ patterns) are statistically meaningful.

In order to address this question, yield models are using various combinations of UAV and EC_a layers as shown in Table 2.5. Table 2.5 presents two different scenarios: one where UAV information is added to pre-existing EC_a information (i.e. models 1 vs. 2), and one where EC_a information is added to pre-existing UAV information (model 3 vs. model 4). Note that models 2-4 only contain the UAV RGB open boll map, based on the results from Table 2.4. The model with the lowest AIC_c value was model 3, which only uses the UAV layer or open boll count information alone (-27.8, Table 2.5). The model with the highest AIC_c was model 1, which uses EC_a only (-4.4). Table 2.5 also shows the effect of adding UAV:EC_a interaction terms. For example, when the UAV:EC_a term was added to the EC_a term (model 2), the AIC_c decreased from -4.4 to -24.2. In contrast, when the UAV:EC_a term was added to the UAV term (model 4), the AIC_c increased from -27.8 to -26.0. Thus, the addition of EC_a to UAV via an interaction term resulted in a relatively worse yield model.

Table 2.5 also gives the ANOVA p-values comparing the significance of the interaction term (i.e. model 1 vs. model 2, model 3 vs. model 4). The p-value in comparing model 1 with model 2 is less than 0.001, indicating that the inclusion of the UAV boll count layer significant changes the model interpretation. The p-value in comparing model 3 with model 4 is 0.69, indicating no significant differences in yield

models when EC_a information is added alongside UAV data. The results from Table 2.5 indicate two main points. First, the addition of UAV information to an EC_a model results in a significantly better yield model. Second, the addition of EC_a information to a UAV model does not result in a significantly better yield model.

Table 2.5 Modeling results that predict yield using various combinations of EC_a and/or UAV terms. The UAV term refers to the open boll created from visible imagery only (Fig. 2.3). ANOVA p-values refer to two cases: comparisons of models 1 and 3, as well as models 2 and 4.

Model	AIC_c	ANOVA p-value
1) EC_a only	-4.4	-
2) EC_a + UAV:EC_a	-24.2	< 0.001
3) UAV (Sep. 26) only	-27.8	-
4) UAV + UAV:EC_a	-26.0	0.69

2.4. Discussion

The purpose of this paper was to evaluate the performance of UAV-based MZs at various points before and within a single growing season. The motivation for UAV MZs stems from the need to monitor crop health, so that farmers can be proactive in achieving their management goals (i.e. maximize yield outputs, minimize management input costs). Current tools such as proximal EC_a sensing have only been partially helpful in this regard because its data is not timely, and it remains an inconsistent predictor of yield depending on climatic condition (Guo et al., 2012). While other papers have suggested that MZs are best created by fusing remotely sensed imagery and EC_a (Triantafilis et al., 2009; Cordoba et al., 2016; Scudiero et al., 2018), it is not always practical or possible to

combine such layers, especially if soil calibration is needed for EC_a signals (EC_a less than 200 mS m^{-1}, Corwin and Scudiero, 2016).

Despite its infancy, UAVs are expected to be increasingly used in the future (Maes and Steppe, 2018). A recent precision agriculture dealership survey (Erickson, 2017) projects that, by 2020, 22 % of central USA dealers will offer UAV imagery services, while EC_a mapping only at 17 %. While their survey does not indicate what proportion of these dealers will use UAVs towards MZ delineation, they are expected to have some role in this application space, at the very least for crop scouting purposes (Hunt and Daughtry, 2017; Nawar et al., 2017). Remote sensing and EC_a tools are meant to compliment, not replace, farmer knowledge towards MZ delineation (Martínez-Casasnovas et al., 2018). MZs can theoretically be used beyond simple crop scouting applications to more complex applications such as variable rate input (e.g. water, fertilizer etc.) management (Hunt and Daughtry, 2017). However, the costs of switching from uniform to variable-rate management are high, and value needs to first be demonstrated. The work presented here is meant to demonstrate this value as a proof-of-concept approach.

While the results presented here only span a single growing season, the value of such results can be contextualized in terms of beginning approaches in MZ delineation. Many farmers define MZs using traditional soil survey maps and/or Google Earth maps. Second, traditional soil survey maps lack consistency and have not been extensively validated (Brevik et al., 2016). Finally, Google Earth has its own set of disadvantages, including: 1) requirements of internet access and 2) requirements of high bandwidth

(Patterson, 2007). While farmer-based MZs offer a starting point towards MZ delineation (Heijting et al., 2011), the results presented here suggest it may be worth exploring complementary tools such as UAVs. UAV MZs, however, cannot diagnose a problem (e.g. water/nutrient deficiencies) - field scouting should always be used to follow up the trends presented by the UAV data.

Considering that RGB sensors are considerably cheaper than multispectral/thermal sensors (Manfreda et al., 2018), or EC_a sensors ($25000 USD, Geonics, personal communication), UAV RGB surveys may serve as a first step in developing MZ strategies. This recommendation has additional weight within cotton production fields, as sensors can generate MZs at the beginning, during and end of a growing season (Table 2.4). While in-season MZ delineation did not include RGB sensors, there is evidence to suggest they can be used in that capacity, for example site-specific weed management (de Castro et al., 2018; Maes and Steppe, 2018). While pre-/post-season MZs cannot be used as proactive tools, per se, they can be used to determine if significant spatial yield variability exists within a field, and whether that variability is consistent from year to year. If this condition is determined to be true, and the cause of the variability is reliably known, UAVs can help a farmer decide if site-specific field management is profitable, and therefore, justifiable. A key component of UAV MZ adoption, in addition to profits, will be delivery time. UAV processing, including geometric and radiometric corrections, can be challenging, especially if large areas are to be monitored (Zhang and Kovacs, 2012). Such processing challenges have been particularly noted for thermal imagery because it can exhibit low contrast within a scene

(Ribeiro-Gomes et al., 2017). Thus, it is imperative that a proper processing pipeline, regardless of the sensor, be established for (near) real-time delivery (Maes and Steppe, 2018).

2.5. Conclusions

The purpose of this study was to evaluate UAV imagery in terms of modeling MZ traits (e.g. height, seed-cotton yield), as well as MZ delineation, relative to previously approaches such as soil EC_a. Regression results indicate that both multispectral imagery (via NDVI) and thermal imagery (T_r) were significant predictors of in-season yield indicators such as canopy height. In addition, their respective MZs showed significant separation during flowering and boll filling, respectively. An RGB sensor could also be used to create MZs at the beginning and end of a season. The paper then addressed how UAV imagery compared with EC_a information in terms of modeling seed cotton yield. While the EC_a survey was also able to separate the field into two distinct zones, AIC_c results indicate that it was outperformed by UAV imagery, even with the high amounts of soil variability encountered within the field (Fig. 2.1b). Furthermore, the addition of UAV imagery via open boll imagery significantly affected the previous EC_a-yield model, suggesting the former may complement EC_a if desired.

Future studies should address the suitability of UAV-based MZs across multiple years, as compared with EC_a sensing. If financial resources permit the use of variable rate technologies, an additional objective would be to conduct a cost-benefit analysis (Nawar et al., 2017). A cost-benefit analysis aims to compare, within a designated test strip, the net returns provided by variable rate strategies versus uniform rate strategies.

The effectiveness of these management strategies will depend on the scale where decisions are implemented. For example, a 10 m block is a reasonable pixel resolution for boom sprayers because it represents the approximate distance between individual spray nozzles (Maes and Steppe, 2018). Of course, this resolution will change depending on the application. For example, Mulla (2013) suggest variable rate of spraying of herbicides operates at a pixel resolution between 0.5-1.0 m, while variable rate of water between 5-10 m. The important point to make here, regardless of selected pixel size, is that UAV MZs need to be defined at the spatial scale at which the information will be used. Thus, in the case of variable rate input scenarios described above, UAV imagery should be aggregated or upscaled to a coarser resolution that falls in line with the needs of the user.

It would also be interesting to compare the efficacy of the open boll detection method presented here against previous yield mapping approaches such as yield monitors. While yield monitors have been successful in mapping cotton yield variability (Thomasson and Sui, 2003; Zarco-Tejada et al., 2005), they can be complicated in terms of installation, calibration and extended maintenance (Fulton et al., 2018). Furthermore, the availability of commercial cotton yield monitors is relatively low compared with grain monitors (Dr. Gaylon Morgan, personal communication), indicating additional motivations to explore the UAV RGB boll mapping approach here. Within this context, RGB-based UAVs may provide a more optimal approach in defining yield-based MZs, given a UAV workflow is in order to produce deliverable results in a timely manner. The

adoption of UAV-based MZs may be aided through deliverables via smart phone/tablet integration (Araus and Kefauver, 2018).

2.6. References

Adamchuk, V. I., Hummel, J. W., Morgan, M. T., & Upadhyaya, S. K. (2004). On-the-go soil sensors for precision agriculture. *Computers and Electronics in Agriculture*, *44*, 71–91.

Ahmad, I. S., Reid, J. F., Noguchi, N., & Hansen, A. C. (1999). Nitrogen sensing for precision agriculture using chlorophyll maps. In *Proceeding of 1999 ASAE/CSAE-SCGR Annual International Meeting* (p. 13).

Allen, R. G., Pereira, L. S., Raes, D., & Smith, M. (1998). *Crop evapotranspiration: guidelines for computing crop water requirements*. *Irrigation and Drainage*.

Araus, J. L., & Kefauver, S. C. (2018). Breeding to adapt agriculture to climate change: affordable phenotyping solutions. *Current Opinion in Plant Biology*, *45*(Figure 2), 237–247. doi:10.1016/j.pbi.2018.05.003

Ballester, C., Zarco-Tejada, P. J., Nicolás, E., Alarcón, J. J., Fereres, E., Intrigliolo, D. S., & Gonzalez-Dugo, V. (2017). Evaluating the performance of xanthophyll, chlorophyll and structure-sensitive spectral indices to detect water stress in five fruit tree species. *Precision Agriculture*, *19*, 1–16.

Berni, J. A. J., Zarco-Tejada, P. J., Suárez, L., & Fereres, E. (2009). Thermal and narrowband multispectral remote sensing for vegetation monitoring from an unmanned aerial vehicle. *IEEE Transactions on Geoscience and Remote Sensing*, *47*, 722–738.

Blackmer, T. M., & Schepers, J. S. (1995). Use of a chlorophyll meter to monitor nitrogen status and schedule fertigation for corn. *Journal of Production Agriculture*, *8*(1), 56–60.

Brevik, E. C., Calzolari, C., Miller, B. A., Pereira, P., Kabala, C., Baumgarten, A., & Jordán, A. (2016). Soil mapping, classification, and pedologic modeling: History and future directions. *Geoderma*, *264*, 256–274.

Burnham, K. P., & Anderson, D. R. (2002). *Model Selection and Multimodel Inference* (2nd ed.). Springer-Verlag New York.

Carlson, T. N., & Ripley, D. A. (1997). On the relation between NDVI, fractional vegetation cover, and leaf area index. *Remote Sensing of Environment*, *62*(3), 241–252.

de Castro, A. I., Torres-Sánchez, J., Peña, J. M., Jiménez-Brenes, F. M., Csillik, O., & López-Granados, F. (2018). An automatic random forest-OBIA algorithm for early weed mapping between and within crop rows using UAV imagery. *Remote Sensing*, *10*(2), 1–21.

Charrad, M., Ghazzali, N., Boiteau, V., & Niknafs, A. (2014). NbClust : An R Package for determining the relevant number of clusters in a data set. *Journal of Statistical Software*, *61*(6), 1–36.

Chen, R., Chu, T., Landivar, J. A., Yang, C., & Maeda, M. M. (2017). Monitoring cotton (*Gossypium hirsutum L.*) germination using ultrahigh-resolution UAS images. *Precision Agriculture*, 1–17.

Cohen, Y., Agam, N., Klapp, I., Karnieli, A., Beeri, O., Alchanatis, V., & Sochen, N. (2017). Future approaches to facilitate large-scale adoption of thermal based images as key input in the production of dynamic irrigation MZs. *Advances in Animal Biosciences*, *8*(2), 546–550.

Cordoba, M. A., Bruno, C., Costa, J. L., Peralta, N. R., & Balzarini, M. G. (2016). Protocol for multivariate homogeneous zone delineation in precision agriculture. *Biosystems Engineering*, *143*, 95–107.

Corwin, D. L., Lesch, S. M., Shouse, P. J., Soppe, R., & Ayars, J. E. (2003). Idenfifying soil properties that influence cotton yield using soil sampling directed by apparent soil electrical conductivity. *Agronomy Journal*, *95*, 352–364.

Corwin, D. L., & Lesch, S. M. (2005). Apparent soil electrical conductivity measurements in agriculture. *Computers and Electronics in Agriculture*, *46*, 11–43.

Corwin, D. L., & Scudiero, E. (2016). Field-Scale Apparent Soil Electrical Conductivity. *Methods of Soil Analysis*, *1*(1), 1–29.

Cotton Australia. (2018). Interesting Cotton Facts. *Cotton Library*. https://cottonaustralia.com.au/cotton-library/fact-sheets/cotton-fact-file-interesting-cotton-facts. Accessed 29 July 2019.

Duan, T., Zheng, B., Guo, W., Ninomiya, S., Guo, Y., & Chapman, S. C. (2017). Comparison of ground cover estimates from experiment plots in cotton, sorghum and sugarcane based on images and ortho-mosaics captured by UAV. *Functional Plant Biology*, *44*, 169–183.

Erickson, B., Lowenberg-Deboer, J., & Bradford, J. (2017). *2017 Precision Agriculture Dealership Survey*. *Purdue University*. Lafayette, IN.

Fleming, K. L., Heermann, D. F., & Westfall, D. G. (2004). Evaluating soil color with farmer input and apparent soil electrical conductivity for MZ delineation. *Agronomy Journal*, *96*, 1581–1587.

Fuchs, M., & Tanner, C. B. (1966). Infrared Thermometry of Vegetation. *Agronomy Journal*, *58*(6), 597–601.

Fulton, J., Hawkins, E., Taylor, R., & Franzen, A. (2018). Yield monitoring and mapping. In D. K. Shannon, D. E. Clay, & N. R. Kitchen (Eds.), *Precision Agriculture Basics* (1st ed., pp. 63–78). Madison, Wisconsin: ASA/CSA/SSSA.

Green, F. H. W., Harding, R. J., & Oliver, H. R. (1984). The relationship of soil temperature to vegetation height. *Journal of Climatology*, *4*(7), 229–240.

Guo, W. (2018). Spatial and temporal trends of irrigated cotton yield in the southern High Plains. *Agronomy*, *8*(12), 298. 1-14.

Guo, W., Maas, S. J., & Bronson, K. F. (2012). Relationship between cotton yield and soil electrical conductivity, topography, and Landsat imagery. *Precision Agriculture*, *13*(6), 678–692.

Hake, K., Burch, T., & Mauney, J. (1989). Making sense out of stalks. *Physiology Today. National Cotton Council.*, 1–4.

Han, X., Thomasson, J. A., Bagnall, G. C., Pugh, N. A., Horne, D. W., Rooney, W. L., et al. (2018). Measurement and calibration of plant-height from fixed-wing UAV images. *Sensors*, *18*, 4092.

Heijting, S., de Bruin, S., & Bregt, A. K. (2011). The arable farmer as the assessor of within-field soil variation. *Precision Agriculture*, *12*(4), 488–507.

Hunt Jr., E. R., & Daughtry, C. S. T. (2017). What good are unmanned aircraft systems for agricultural remote sensing and precision agriculture? *International Journal of Remote Sensing*, 1–32.

Hurvich, C. M., & Tsai, C.-L. (1989). Regression and time series model selection in small samples. *Biometrika*, *76*(2), 297–307.

Jiménez-Muñoz, J. C., Sobrino, J. A., Gillespie, A., Sabol, D., & Gustafson, W. T. (2006). Improved land surface emissivities over agricultural areas using ASTER NDVI. *Remote Sensing of Environment*, *103*(4), 474–487.

Johnson, J., MacDonald, S., Meyer, L., & Stone, L. (2018). *The world and Untied States cotton outlook.* Arlington, Virginia.

Lou, Z., Xin, F., Han, X., Lan, Y., Duan, T., & Fu, W. (2018). Effect of unmanned aerial vehicle flight height on droplet distribution, drift and control of cotton aphids and spider mites. *Agronomy*, *8*, 187.

Lund, E. D., Christy, C. D., & Drummond, P. E. (1999). Practical applications of soil electrical conductivity. In *Proceedings of the 2nd European Conference on Precision Agriculture* (pp. 1–9).

Maes, W. H., & Steppe, K. (2012). Estimating evapotranspiration and drought stress with ground-based thermal remote sensing in agriculture: a review. *Journal of Experimental Botany*, *63*(13), 4671–4712.

Maes, W. H., & Steppe, K. (2018). Perspectives for remote sensing with unmanned aerial vehicles in precision agriculture. *Trends in Plant Science*, *24*(2), 152–164.

Manfreda, S., McCabe, M. F., Miller, P. E., Lucas, R., Madrigal, V. P., Mallinis, G., et al. (2018). On the use of unmanned aerial systems for environmental monitoring. *Remote Sensing*, *10*(4).

Marino, S., & Alvino, A. (2018). Detection of homogeneous wheat areas using multi-temporal UAS images and ground truth data analyzed by cluster analysis and ground truth data analyzed by cluster analysis. *European Journal of Remote Sensing*, *51*(1), 266–275.

Martínez-Casasnovas, J., Escolà, A., & Arnó, J. (2018). Use of farmer knowledge in the delineation of potential MZs in precision agriculture: a case study in maize (*Zea mays L.*). *Agriculture*, *8*(6), 84.

Matese, A., Di Gennaro, S. F., Miranda, C., Berton, A., & Santesteban, L. G. (2017). Evaluation of spectral-based and canopy-based vegetation indices from UAV and Sentinel 2 images to assess spatial variability and ground vine parameters. *Advances in Animal Biosciences*, *8*(2), 817–822.

McNeill, J. D. (1980). *Electromagnetic terrain conductivity measurement at low induction numbers. Technical Note TN-6.* (Vol. 76). Ontario, Canada.

McNeill, J. D. (1992). Rapid, accurate mapping of soil salinity by electromagnetic ground conductivity meters. In *Advances in Measurement of Soil Physical Properties: Bringing Theory Into Practice* (pp. 209–229). Madison, Wisconsin: SSSA.

Mulla, D. J. (2013). Twenty five years of remote sensing in precision agriculture: key advances and remaining knowledge gaps. *Biosystems Engineering*, *114*(4), 358–371.

Nawar, S., Corstanje, R., Halcro, G., Mulla, D., & Mouazen, A. M. (2017). *Delineation of Soil MZs for Variable-Rate Fertilization: A Review*. *Advances in Agronomy* (1st ed., Vol. 143). Elsevier Inc.

Padua, L., Marques, P., Hruska, J., Adao, T., Peres, E., Morais, R., & Sousa, J. J. (2018). Multi-temporal vineyard monitoring through UAV-based RGB imagery. *Remote Sensing*, *10*, 1907.

Patterson, T. C. (2007). Google Earth as a (not just) geography education tool. *Journal of Geography*, *106*, 145–152.

Pritsolas, J., Pearson, R., Connor, J., & Kyveryga, P. (2016). Challenges and successes when generating in-season multi-temporal calibrated aerial imagery. In *Proceedings of the 13th International Conference on Precision Agriculture* (pp. 1–15).

Rhoades, J.D.; Manteghi, N. A.; Shouse, P. J.;Alves, W. J. (1989). Soil electrical conductivity and soil salinity: new formulations and calibrations. *Soil Science Society of America Journal*, *53*, 433–439.

R Core Development Team (2018). R: A Language and Environment for Statistical Computing. Vienna, Austria.

Robinson, D. A., Lebron, I., Lesch, S. M., & Shouse, P. (2004). Minimizing drift in electrical conductivity measurements in high temperature environments using the EM-38. *Soil Science Society of America Journal*, *68*(2), 339–345.

Rouse, J. W., Hass, R. H., Schell, J. A., & Deering, D. W. (1974). Monitoring vegetation systems in the great plains with ERTS. *Third Earth Resources Technology Satellite (ERTS) symposium*, *1*, 309–317.

Rouze, G., Neely, H., Morgan, C., Kustas, B., McKee, L., Prueger, J., et al. (in preparation). Evaluation of contextual and non-contextual Unmanned Aerial Vehicle (UAV) evapotranspiration across various pixel resolutions and soil types.

Schepers Aaron, R., Shanahan John, F., Liebig Mark, A., Schepers James, S., H., J. S., & Ariovaldo, L. J. (2004). Appropriateness of MZs for Characterizing Spatial Variability of Soil Properties and Irrigated Corn Yields across Years. *Agronomy Journal*, (96), 195–203.

Scudiero, E., Teatini, P., Manoli, G., Braga, F., Skaggs, T. H., & Morari, F. (2018). Workflow to establish time-specific zones in precision agriculture by spatiotemporal integration of plant and soil sensing data. *Agronomy*, *8*, 253.

Shi, Y., Thomasson, J. A., Murray, S. C., Pugh, N. A., Rooney, W. L., Shafian, S., et al. (2016). Unmanned aerial vehicles for high-throughput phenotyping and agronomic research. *PloS one*, *11*(7), e0159781.

Smith, G. M., & Milton, E. J. (1999). The use of the empirical line method to calibrate remotely sensed data to reflectance. *International Journal of Remote Sensing*, *20*(13), 2653–2662.

Stanislav, S. (2010). *A field-scale assessment of soil-specific seeding rates to optimize yield factors and water use in cotton. Masters Thesis.* Texas A&M University.

Taskos, D. G., Koundouras, S., Stamatiadis, S., Zioziou, E., Nikolaou, N., Karakioulakis, K., & Theodorou, N. (2015). Using active canopy sensors and chlorophyll meters to estimate grapevine nitrogen status and productivity. *Precision Agriculture*, *16*(1), 77–98.

Thomasson, J. A., & Sui, R. (2003). Mississippi cotton yield monitor: three years of field-test results. *Applied Engineering in Agriculture*, *19*(6), 631–636.

Tisseyre, B., & Leroux, C. (2017). How significantly different are your within field zones ? *Advances in Animal Biosciences: Precision Agriculture*, *8*(2), 620–624.

Torres-Rua, A. (2017). Vicarious calibration of sUAS microbolometer temperature imagery for estimation of radiometric land surface temperature. *Sensors*, *17*(7), 1499.

Triantafilis, J., Kerridge, B., & Buchanan, S. M. (2009). Digital soil-class mapping from proximal and remotely sensed data at the field level. *Agronomy Journal*, *101*(4), 841–853.

U.S. Census Bureau Trade Data. (2018). Global agricultural trade system. https://apps.fas.usda.gov/gats/default.aspx. Accessed 29 July 2019.

Webster, R., & Oliver, M. A. (1992). Sample adequately to estimate variograms of soil properties. *Journal of Soil Science*, *43*, 177–192.

Westoby, M. J., Brasington, J., Glasser, N. F., Hambrey, M. J., & Reynolds, J. M. (2012). "Structure-from-Motion" photogrammetry: A low-cost, effective tool for geoscience applications. *Geomorphology*, *179*, 300–314.

Xia, T., Kustas, W. P., Anderson, M. C., Alfieri, J. G., Gao, F., McKee, L., et al. (2016). Mapping evapotranspiration with high-resolution aircraft imagery over vineyards using one-and two-source modeling schemes. *Hydrology and Earth System Sciences*, *20*(4), 1523–1545.

Yeom, J., Jung, J., Chang, A., Maeda, M., & Landivar, J. (2018). Automated open cotton boll detection for yield estimation using unmanned aircraft vehicle (UAV) data. *Remote Sensing*, *10*(12), 1–20.

Yu, Q., Acheampong, M., Pu, R., Landry, S. M., Ji, W., & Dahigamuwa, T. (2018). Assessing effects of urban vegetation height on land surface temperature in the City of Tampa, Florida, USA. *International Journal of Applied Earth Observation and Geoinformation*, *73*, 712–720.

Zarco-Tejada, P. J., Ustin, S. L., & Whiting, M. L. (2005). Temporal and spatial relationships between within-field yield variability in cotton and high-spatial hyperspectral remote sensing imagery. *Agronomy Journal*, *97*(3), 641–653.

Zhang, C., & Kovacs, J. M. (2012). The application of small unmanned aerial systems for precision agriculture: A review. *Precision Agriculture*, *13*(6), 693–712.

Zhou, X., Zheng, H. B., Xu, X. Q., He, J. Y., Ge, X. K., Yao, X., et al. (2017). Predicting grain yield in rice using multi-temporal vegetation indices from UAV-based multispectral and digital imagery. *ISPRS Journal of Photogrammetry and Remote Sensing*, *130*, 246–255.

3. EVALUATION OF CONTEXTUAL AND NON-CONTEXTUAL UNMANNED AERIAL VEHICLE (UAV) EVAPOTRANSPIRATION ACROSS PIXEL RESOLUTIONS AND SOIL TYPES

3.1. Introduction

Farmers who utilize irrigation water face pressures in terms of competition across different sectors (e.g. oil/gas, municipal etc.) (Vanham, 2016). These farmers also face competition amongst other farmers within so-called hotspots, which refer to stresses where water is distributed unequally within the food, energy and water ecosystem (Mohtar and Daher, 2016). Thus, any water that is available to farmers should be applied towards crops in the most efficient way possible. The goals of any irrigation strategy are to minimize water use, maximize yield, and minimize agrochemical leaching or runoff (Evans and Sadler, 2008). Previous best management practices for irrigation scheduling have been conducted with soil moisture sensors, such as time-/frequency-domain reflectometers and neutron moisture meters (NMMs) (Campbell and Campbell, 1982). However, the use of soil moisture sensors for irrigation scheduling can be problematic for several reasons. First, sensor installation and upkeep can be costly, particularly within fields that exhibit soil heterogeneity (Jones, 2004). Second, selecting a uniform depth for sensor placement can be difficult, as the root zone depth varies as a function of crop development stage, soil moisture and nutrient availability (Zotarelli et al., 2009). Lastly, and perhaps most importantly, soil moisture changes are not directly tied with changes in plant response or physiology (Jones, 2007).

Alternative strategies towards irrigation management have been proposed through ET scheduling (Penman, 1952; Jensen et al., 1969). ET refers to the loss of water to the atmosphere, both from surface (i.e. leaf/soil) evaporation and from leaf transpiration. ET is a complex parameter controlled by multiple factors such as solar radiation, humidity, air temperature (T_a), wind speed, soil moisture, rooting depth, LAI, and stomatal conductance (Verstraeten et al., 2008; Fisher et al., 2017). Initial approaches towards estimating ET, such as eddy flux towers and lysimeters, while reliable, are effectively point measurements and cannot capture spatial variability within a field (Verstraeten, 2008). One alternative approach towards estimating ET has been made with remotely sensed imagery (Rajan et al., 2010). Unlike soil moisture sensors and previous ET techniques, remote sensing can characterize plant responses in a direct manner beyond point measurements. Recent reviews by Alvino and Marino (2017) and Calera et al. (2017) demonstrate positive contributions of the technology towards irrigation scheduling. Remote sensing within this context can focus on two distinct regions of the electromagnetic spectrum. First, visible and near-infrared wavelengths, or the optical region (~0.4-1.4 μm), are used to model plant reflectance properties and, therefore, growth parameters such as LAI and vegetation fraction cover (or f_c) (Rouse et al., 1974; Maas and Rajan, 2008). Second, emittance properties within the long-wave thermal-infrared radiation (~7-14 μm) are used to monitor crop stress through established relationships with stomatal conductance (Farquhar and Sharkey, 1982). Remotely sensed imagery can be obtained from a host of airborne platforms, with recent technological advancements such as UAVs providing enhanced flexibility relative to pre-existing

platforms (i.e. satellites, manned aerial vehicles), as well as finer pixel resolutions (Shi et al., 2016).

Remote sensing does not directly measure ET - instead, it is estimated using a model. One ET modelling group combines empirical relationships and physical equations under the surface energy balance (or SEB) equation (Courault et al., 2005). The SEB equation estimates ET based on the SEB equation using latent heat (or LE) as a proxy:

$$LE = R_n - G - H, \quad \text{(Eq. 3.1)}$$

where R_n is net radiation, G is soil heat flux, and H is sensible heat flux (all terms in units of W m^{-2}). Additional terms such as photosynthetic and heat storage within canopy layers are omitted from Eq. 3.1, as these terms are less than five percent of R_n within most agricultural crops (Meyers and Hollinger, 2004). ET can then be calculated from LE by dividing the latent heat of vaporization or λ (units of J kg^{-1}) and the density of water (1000 kg m^{-3} at 20° C). Within the context of SEB modelling, remotely sensed imagery is useful because it provides spatial coverage of input parameters needed in estimating surface flux components for Eq. 3.1 (Liou et al., 2014).

SEB models can be decomposed into non-contextual or contextual models. Non-contextual methods solve Eq. 3.1 using absolute measurements of T_r, as well as ground input data (e.g. T_a, wind speed, relative humidity). One example of a non-contextual model is a two-source energy balance (TSEB) model. TSEB models treat Eq. 3.1 separately with respect to canopy and soil, resulting in two separate energy balance equations (Norman et al., 1995):

$$LE_c = R_{n,c} - H_c \quad \text{(Eq. 3.2a)}$$

$$LE_s = R_{n,s} - H_s - G, \quad \text{(Eq. 3.2b)}$$

where 'c' and 's' refer to the canopy and soil components, respectively. In order to estimate all components of Eq. 3.2, multispectral and thermal imagery are needed. TSEB models decompose T_r into canopy (T_c) and soil (T_s) temperatures using a mixing model (Norman et al., 1995):

$$T_r = [f_c * T_c^4 + (1 - f_c) * T_s^4]^{1/4}, \quad \text{(Eq. 3.3)}$$

f_c is given from multispectral imagery collected alongside thermal imagery or T_r. T_c and T_s are then used to find H_c/LE_c and H_s/LE_s, respectively (Eq. 3.2). Variants of the TSEB model differ in how to extract T_c and T_s (and thus H_c and H_s, respectively). Three popular TSEB sub-models include the Priestley-Taylor iterative retrieval (TSEB-PT) model (Norman et al., 1995), dual-time-difference (TSEB-DTD) model (Norman et al., 2000), and, more recently, a hybrid (i.e. contextual + non-contextual) two-component temperature (TSEB-2T) model (Nieto et al., 2018b).

Contextual methods, in contrast, solve the SEB equation based on observations of hot and cold endmembers located within a given thermal image; therefore, fluxes are driven by relative (rather than absolute) T_r measurements. Furthermore, contextual models estimate LE by combining soil and canopy systems together, as opposed to treating them separately as in Eq. 3.2. Contextual models are especially attractive in situations where collecting thermal imagery, multispectral imagery and field data is not possible. One recent contextual ET model, called DATTUTDUT, only requires one input, namely thermal imagery (Timmermans et al., 2015). Although recent studies have additionally supplied local incoming shortwave radiation (SW_{in}) data. For example by

Brenner et al. (2018), have shown that DATTUTDUT, when supplied with SW_{in}, was slightly more accurate (14 W m^{-2}, mean not reported) than TSEB-PT within simple vegetation structures such as grasslands (Brenner et al., 2018). However, such observations have not always been extended towards other crops with more complex architectures. For example, Xia et al. (2016) found that the accuracy of DATTUTDUT within vineyards was degraded relative to TSEB-PT because the former could not account for differing heat sources (i.e. vines vs. bare soil/senescent cover crop). DATTUTDUT modelling errors also arise when dry soil and/or dense vegetation pixels are not found, particularly within extreme (i.e. arid/humid) environments (Timmermans et al., 2015). It would be interesting to determine how these conflicting reports are resolved within other unexplored crops such as cotton (*Gossypium hirsutum L.)*. DATTUTUDUT modelling studies have also not addressed the importance of local weather data (e.g. SW_{in}) in its estimations of LE, as such data is used inconsistently (Xia et al., 2016; Brenner et al., 2018).

Given the plethora of SEB models available, model selection remains a challenging task. While some research suggests non-contextual models outperform contextual models using satellites (Choi et al., 2009), the opposite has been reported with UAVs (Brenner et al., 2017). Thus, there is still debate on which SEB model is most applicable under particular environmental conditions, especially when considering parameters that regulate ET within a field such as soil moisture (Alfieri et al., 2007). Model comparisons using accepted validation techniques such as eddy covariance could help guide model selection for future applications with similar crops and environmental conditions. Eddy

covariance towers have been previously used to validate UAV fluxes, for example, within grasslands (Brenner et al., 2017), barley (Hoffmann et al., 2016), olives (Ortega-Farias et al., 2016), and vineyards (Kustas et al., 2018). Most of these validation studies have been designed over uniform soils and have not addressed the effects of soil variability on ET variability. In addition, some of these studies model ET at sub-meter resolutions, which can present problems with respect to TSEB modelling (Nieto et al., 2017; Aboutalebi et al., 2019). In such situations, UAV ET should be aggregated towards coarser pixel resolutions that align with management operation scales (i.e. 1-10 m). However, studies have not currently addressed the effect of UAV-based image aggregation on model comparison and performance.

The purpose of this study is to evaluate non-contextual (TSEB-PT, TSEB-2T, TSEB-DTD) and contextual (i.e. DATTUTDUT) model estimates of R_n, G, H, and LE (or ET) within a single field and single cotton growing season. The value of ancillary weather inputs (i.e. SW_{in}, T_a, actual vapor pressure or e_a) within DATTUTDUT modelling is included. The second main objective is to quantify how differences in soil properties affect non-contextual and contextual ET model estimates. To address both objectives, surface energy balance components are generated from UAV imagery at two different pixel resolutions, mainly those at soil-plant mixed (1.05 m) and sharpened satellite (10.05 m) pixel scales. These pixel resolutions are associated with Sentinel-3 thermal imagery sharpened to Sentinel-2 multispectral imagery (Guzinski and Nieto, 2019). The estimated fluxes obtained with these different models and resolutions are then validated with independent eddy covariance flux tower measurements across two soil types

identified within the field. Effects of soil differences are also addressed in terms of LE, T_c, and T_s model output across the entire field. DATTUDUT model performance is finally explored further in terms of LE to environmental conditions such as soil variability via temperature endmember selection.

3.2. Methods

3.2.1. Study area and management

The study site (17-ha cotton field) is located on the Texas A&M Experimental Farm located in central-eastern Texas (Fig. 3.1a). Surface soil color varies within the field, with darker and lighter soils on the left and right sides of the field, respectively (Fig. 3.1a). The spatial distribution of the soils can be explained in terms of its geological history, as clay-sized particles were deposited relatively further from the once active fluvial channel (Fig. 3.1a). Elevations are relatively constant, with an average elevation of 67.7 ± 0.3 m AGL (based on 2017 UAV digital surface models, Sect. 3.2.3). Soil surface textures include silt loam, silty clay loam, and silty clay (Stanislav, 2010), and the soils are classified as Hapluderts, Haplusteps, and Ustifluvents. Previous research by Rouze et al. (in preparation) has shown that these soils can be grouped into two disparate zones, or soil types, based on EC_a values from an electromagnetic induction survey (Fig. 3.1b). The mean of the high and low EC_a zones in Fig. 3.1b are 72 ± 20 mS m^{-1} and 43 ± 18 mS m^{-1}, respectively (± 2σ). The corresponding mean clay content within each zone, based on these EC_a values, is 391 ± 20 g kg^{-1} and 253 ± 18 g kg^{-1} (± 2σ) (Stanislav, 2010). These two regions will respectively be referred to as ‘high EC_a’ and ‘low EC_a’

zones in all further analysis. A previous study by Stanislav (2010) determined that EC_a was a significant predictor of clay content and soil water holding capacity.

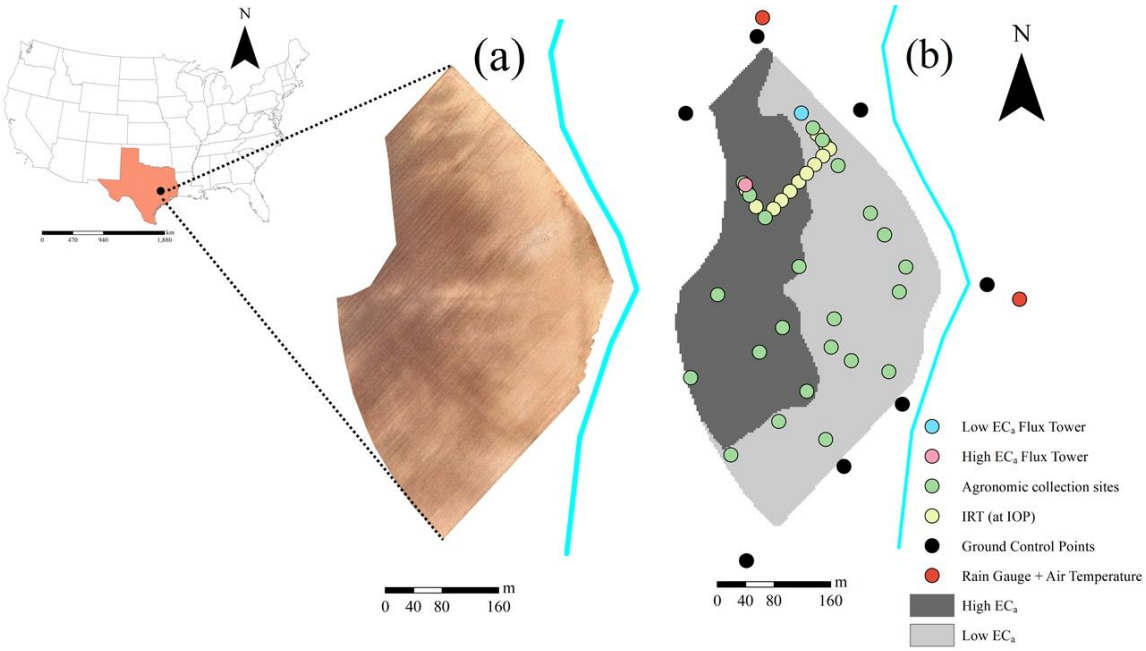

Fig. 3.1 (a) Location of study area within the United States and the state of Texas. Visual image was collected by a consumer grade digital camera aboard a UAV about two weeks before planting. The light blue line to the right of the field indicates an abandoned fluvial channel. (b) Locations of various field equipment and agronomic sites established throughout the 2017 growing season. Light and dark grey areas correspond with low and high EC_a zones, respectively (Rouze et al., in preparation). Agronomic collection sites include measured variables such as leaf area index, soil moisture, canopy height, and canopy width. Additional infrared thermography (IRT) measurements were consistently collected at the time of each UAV overpass or intense observation period (IOP) (yellow, Table 3.1).

In past seasons, the field was actively managed with conventional tillage practices and kept in a continuous crop rotation of corn (*Zea mays L.*) and cotton. In 2017, cotton (PHY 444 WRF variety) was planted at a rate of 111,200 seeds ha^{-1} and 1.02 m row

spacing on April 5, 2017 (day of year or DOY 95). Pre-emerge and post-emergence herbicides (Prowl H_2O, Cotoran 4L, Cornerstone Plus) were applied to ensure uniform stand establishment. In-season management of cotton included fertilization, plant growth regulation, and weed control based on best management practices. First flowering was observed on June 8 (64 DAP), with cutout (i.e. five NAWF) observed on July 1, 2017. Boll filling occurred approximately between June 29 and July 28 (85-112 DAP, defined here as 2 NAWF). Open bolls for about 90 % of the field occurred around September 1 (210 DAP). Defoliation occurred on September 9, 2017 (157 days after planting or DAP). Cotton harvest was conducted on October 10, 2017 (188 DAP).

Fig. 3.1b (red) shows the locations of two 1.25 m mounted tipping buckets that collected precipitation and T_a data every fifteen minutes (HOBO-RG3, Onset, Bourne, USA). Fig. 3.2a displays daily temperatures averaged across both rain gauges during vegetative growth (0-2305 growing degree days or GDD). The mean daily minimum, maximum and average temperatures during this time period were 19.0° C, 34.5° C and 26.0° C, respectively. The cotton experienced some particularly cold days during the early season, as daily minimum temperatures exceeded below the threshold for optimal growth (16° C) (0-649 GDD, Fig. 3.2a). Similarly, cotton experienced hot days during late growth (1545-2338 GDD), as daily maximum temperatures exceeded above the threshold for optimal growth (38° C).

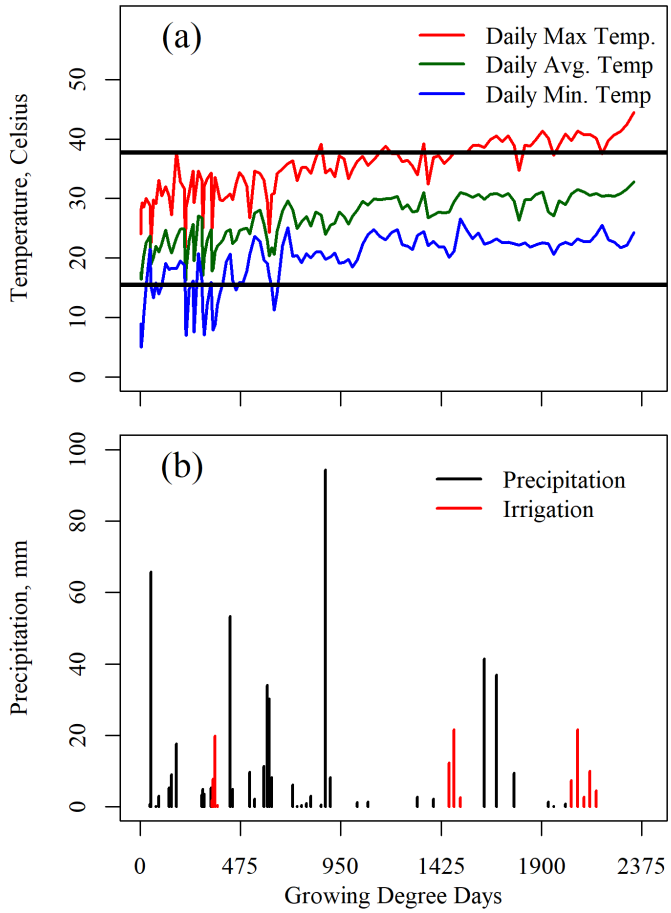

Fig. 3.2 (a) Daily temperature plotted against cotton growing degree days in 2017 based on averages from nearby rain gauges (Fig. 3.1b, red). The two horizontal lines at 16° C and 38° C refer to the thresholds beyond which cotton plants experience little to no development. (b) Daily precipitation and irrigation (black and red, respectively) also plotted by growing degree days.

Fig. 3.2b shows daily precipitation averaged across both rain gauges. The cotton field received 1248 mm of precipitation during the growing season, but only 40 % of that (491 mm) was supplied during vegetative growth. A heavy rain event (65.8 mm) occurred during cotton planting and emergence (around 51 GDD), resulting in soil crusting and some poor stands. The field operates under a central pivot irrigation system

that is about 513 m long with 10 spans, each 48 meters long. Due to the field size, each irrigation event lasted about 2.5 days. Approximately 21.5 mm of water was applied on May 4 (339 GDD), June 28 (1462 GDD), July 19 (2041 GDD), and July 21 (2100 GDD). Fig. 3.2b shows daily irrigation data provided by the company (FieldNET Lindsay Corporation, Omaha, USA).

3.2.2. UAV field campaign

Table 3.1 shows the dates, or intense observation periods (IOP), on which UAV surveys were conducted. The main growth stages selected for this study include cotton flowering and boll filling. Multispectral images were collected from a RedEdge camera (MicaSense, Seattle, USA). The RedEdge camera is a complementary metal–oxide–semiconductor (CMOS) 16-bit sensor that detects electromagnetic radiation in the blue (0.455-0.495 μm), green (0.540-0.580 μm), red (0.659-0.678 μm), near-infrared (0.800-0.880 μm), and red-edge (0.707-0.727 μm) bands. The focal length used for the Micasense camera was six mm. Thermal images were collected using a 14-bit ICI 8640-P sensor (7.0-14.0 μm), which is an uncooled focal plane array microbolometer with Vanadium Oxide film (Infrared Cameras Inc., Beaumont, USA). Thermal sensors measure brightness directional temperature by inverting Planck's blackbody equation over a specified wavelength range (Norman and Becker, 1995). The ICI camera has a reported accuracy of ± 1^{o} C based on blackbody laboratory calibration, although such reported accuracies have been shown to degrade under field conditions (Torres-Rua et al., 2017). The focal length used for the ICI 8640-P was 12.5 mm.

Table 3.1 Agronomic data, flight times, and pixel sizes for all Intense Observation Periods (IOP) dates. Agronomic information includes average nodes above white flower (or NAWF), along with growing stage and corresponding growing degree days (GDD). GDDs refer to heat accumulation units that are used to predict cotton phenology. The local times associated with each multispectral and thermal surveys are also listed, with the latter decomposed into AM and PM flights.

Date	Growing Stage	Average NAWF	GDD	PM Flight Time - Multispectral	Early AM Flight Time - Thermal	PM Flight Time - Thermal	Native Pixel Size (m)		
							Multispectral	AM Thermal	PM Thermal
June 16, 2017	Flowering	7	1161	13:48-14:10	7:57-8:15	13:00-13:15	0.07	0.23	0.15
July 1, 2017		5	1545	12:05-12:27	7:53-8:07	14:36-14:50	0.08	0.16	0.15
July 18, 2017	Boll filling	2	2013	11:05-11:23	8:15-8:28	12:29-12:42	0.08	0.16	0.15
July 26, 2017			2246	11:27-11:48	7:54-8:10	12:00-12:11	0.08	0.22	0.15

Due to platform limitations, RedEdge and 8640-P cameras were flown separately and thus at different times (Table 3.1). Both cameras were equipped aboard on a fixed wing UAV platform (Tuffwing UAV Mapper, Boerne, USA). The UAV communicated with a ground control station at a frequency of 915 MHz. Flight plans were created on auto-pilot mode within the Mission Planner software (ArduPilot Dev Team). The multispectral camera was set under manual settings, with exposure times ranging between 0.44-1 seconds depending on band. Flight control was maintained using a Pixhawk controller, which operates under the NuttX real-time operating system. In order to achieve full field coverage while minimizing cloud variability and thermal drift, multispectral and thermal surveys were flown at 65 and 60 % sidelap and overlap, respectively. Most flights were carried out under clear skies, with average winds below 4

m s^{-1}. However, on July 1, thin (but uniform) cloud cover was present. In addition to cloud cover, July 1 differed from other dates in that its survey was conducted relatively late (Table 3.1). The average flight time for the thermal and multispectral imagery was 13 and 20 minutes, respectively. All multispectral and thermal afternoon flights were conducted within ± two hours of local solar noon (13:30) (Table 3.1). However, additional morning flights were conducted to facilitate TSEB-DTD modelling (Sect. 3.2.6.2). The timing of these early morning surveys was no later than 1.5 hours after sunrise, per the recommendations by Anderson et al. (1997). The altitude at which all surveys was conducted was 120 m AGL, resulting in multispectral and thermal pixel resolutions of about 0.07 and 0.15 m, respectively (Table 3.1). All images were instantaneously geotagged using a u-blox M8N GPS module aboard the UAV platform. The reported geometric accuracy of the u-blox M8N GPS is two meters.

In order to create orthorectified maps with high positional accuracies (cm), GCPs were deployed across the perimeter of the field (black circles, Fig. 3.1b). A GCP was designed from plywood and consisted of a two-level deck, whose spatial coordinates were measured using a real time kinematic (RTK) Trimble R7/R8 GPS system (Trimble Inc., Sunnydale, CA, USA). Thermal orthomosaics were later aided by attaching aluminized polyester located on the upper level of each GCP. Each deck level on a given GCP securely housed three radiometric calibration tiles (six tiles per GCP) with known albedo values of 4, 20 and 45 % obtained from a spectral radiometer (Spectral Evolution PSR+ 3500). The size of each calibration tile was 0.61 x 0.61 m. These radiometric

calibration tiles served to later calibrate the UAV multispectral imagery. Additional information regarding these GCPs can be found in Han et al. (2018).

3.2.3. Image processing

After image collection, both multispectral and thermal images were transferred to a computer for further processing. AM and PM thermal images were first processed from 8-bit digital numbers (DNs) or radiance to 16-bit camera calibrated brightness temperature (T_{br}) using the provided software (IRFlash 2.16.4.21). T_{br} is not the same as T_r, the variable of interest, as the former contain sources of uncertainty such as atmospheric attenuation and differences in land surface emissivity (ε) within a scene (Torres Rua et al., 2017). T_r can be estimated from T_{br} at each i^{th} pixel, given ε and the background air temperature (T_{bg}) (Maes and Steppe, 2012):

$$T_{r,i} = \sqrt[4]{\frac{T_{br,i}^4 - (1-\varepsilon)T_{bg}^4}{\varepsilon_i}} \quad \text{(Eq. 3.4)}$$

Because soil and vegetation pixels were visible from thermal images at all points in time, and because these two objects were found to exhibit different ε values from field measurements, spatially distributed ε was needed to derive accurate T_r (Eq. 3.4). ε was calculated at each i^{th} pixel, therefore, by weighting soil and vegetation ε values (ε_s and ε_v, respectively) by f_c (Jimenez-Munoz et al., 2006):

$$\varepsilon_i = \varepsilon_s(1 - f_{c,i}) + \varepsilon_v f_{c.i} \quad \text{(Eq. 3.5)}$$

where ε_s was 0.96 as obtained from a box method (Fuchs and Tanner, 1966), and ε_v was set to 0.99, per recommendations from Maes and Steppe (2012). $f_{c,i}$ was derived

from NDVI imagery by scaling between maximum NDVI ($NDVI_{max}$) and soil NDVI ($NDVI_s$) (Carlson and Ripley, 1997):

$$f_{c,i} = (\frac{NDVI_i - NDVI_s}{NDVI_{max} - NDVI_s})^2 \quad \text{(Eq. 3.6)}$$

$NDVI_{max}$ was taken to be the maximum NDVI observed from the original spatial resolution (0.976). $NDVI_s$ was based off an average bare soil NDVI using UAV imagery collected before cotton squaring (0.2). T_{bg} (Eq. 3.4) was found using T_a data from an HC2S3 temperature probe (Campbell Scientific, Logan, USA).

Validation for the thermal correction approach above was assessed by comparing predicted and measured T_r obtained using a handheld sensor (MI-220, Apogee Instruments, Logan, USA). Measured T_r values refer to vegetated and bare soil surfaces during thermal image collection (Fig. 3.1a, yellow circles). Predicted temperatures were computed by first aggregating up to the field-of-view of the IRT (around 0.08 m^2).

Predicted canopy and soil temperatures were obtained by extracting the minimum and maximum temperatures within the approximate measurement area (3 m radius). Mean absolute error (MAE) values of 2.6 and 4.6 °C and mean biases (predicted-measured) of 1.9 and -2.6 °C were found for plants and soils, respectively. One possible source of error lies within the different spectral ranges between a ground thermal sensor (i.e. MI-220, Apogee Instruments, Logan, USA) and the aerial thermal sensor (i.e. ICI-8640 P) (8-14 μm and 7-14 μm, respectively).

All multispectral and afternoon PM thermal images (T_r, Eq. 3.4) collected from each survey (Table 3.1) were then used to generate orthomosaics using the commercial software Agisoft PhotoScan Pro (St. Petersburg, RU). Orthomosaic generation is based

on the structure from motion method, which is based on steps such as: 1) image alignment, 2) 3D geometry creation, 3) ortho-photo generation, and 4) digital surface model generation (Westoby et al., 2012). Orthomosaic generation was aided by GCPs (Fig. 3.1a, black) and their known locations using the RTK GPS described earlier. Thermal orthomosaic generation was additionally aided by attaching (and subsequently identifying) aluminized polyester located on the upper level of each GCP. For AM T_r images, however, a different procedure was performed, as orthomosaic generation was difficult due to a low number of matching features. Instead, a partial orthomosaic was generated within ArcGIS by orthorectifying select images using multispectral imagery as a visual guide (ESRI, Redlands, USA). The images were selected based on their location within the eddy covariance footprint (Sect. 3.2.7.4.). Because AM surveys are generally characterized by relatively lower T_r variability, an average T_r was calculated within each partial orthomosaic – this approach has precedence within literature (Hoffmann et al., 2016). Exported orthomosaics were deemed acceptable and exported as GeoTIFFs when the positional RMSE values were less than or equal to 1.5 times the pixel resolution.

Radiometric calibration was performed on multispectral orthomosaics using the empirical line method (Smith and Milton, 1999). A previous study by Iqbal et al. (2018) demonstrated that the empirical line method can be used to calibrate UAV multispectral sensors, assuming the size of the calibration targets are sufficiently large (here, 9 x 9 pixels). In this method, DNs acquired from the red and NIR bands were converted into percent reflectance using various objects located within the field. The interest in calibrating red and NIR bands was so that NDVI (NDVI = $\frac{NIR+Red}{NIR-Red}$) orthomosaics could

be derived for later use in the modelling phase. For the red band, it was observed that crop DNs were much lower than that of the five percent albedo target, resulting in artificially negative reflectance values. To get around this, a new low-end reflectance point within the red band was established within nearby tree shadows at two percent (Pristolas et al., 2016). Similar problems were encountered for the NIR band, where crop DNs were higher than the 45 % albedo target. Therefore, a new high-end reflectance point was established using the GCP plywood material, measured at 79 %. Quality control on this approach was performed by comparing the predicted red/NIR reflectance values with ground reflectance data collected at the calibration tiles. In this comparison, reflectance values agreed well independent ground-truth measurements, with a bias (bias = predicted – observed) of 0.5 % and an RMSE of 2.5 %. This accuracy is similar, if not lower, than similar analyses conducted by Berni et al. (2009) and Xia et al. (2016).

3.2.4. Agronomic data collection

Agronomic field data collected on each IOP include: 1) root zone soil moisture, 2) LAI, 3) plant width, 4) plant height, and 5) leaf width (Fig. 3.1b). Soil moisture was collected to quantify soil watser variability by EC_a zone (Fig. 3.1b), while LAI, plant width/height and leaf width were needed for later modelling of surface energy fluxes. Root zone soil moisture was measured using a CPN 503 DR NMM and sampled in 5.1-cm diameter access tubes at various depths (0.2, 0.4, 0.6, 0.8, and 1.0 m) below the soil surface (Campbell Pacific Nuclear, Concord, USA). Soil moisture properties of interest include: 1) average depth of water (mm), found by averaging volumetric water content

(θ_v) across the entire root zone depth (here 1 m based on inspection of NMM data), and 2) percentage of available water depleted (AWD) from field capacity:

$$AWD = \frac{(\theta_{FC,i} - \theta_{i,t})}{(\theta_{FC,i} - \theta_{PWP,i})} * 100, \quad \text{(Eq. 3.7)}$$

where *i* is a given sampling location, *t* is the sampling date, θ_{FC} is volumetric water content at field capacity (i.e. first sampling date), and θ_{PWP} is volumetric water content at permanent wilting point established through clay content calibrations with EC_a (Stanislav, 2010). LAI measurements were taken with a LAI-2200C sensor (LI-COR, Lincoln, NE, USA), either one hour before sunrise or one hour before sunset. All LAI campaigns were collected in a two-day span from a UAV thermal overpass (Table 3.1). LAI measurements were taken approximately in an area spanning three meters by three rows (~1.02 x 1.02 m). All LAI observations were collected directly underneath cotton plants along a row, and one-fourth, one-half, and three-fourths distance from the cotton row using a 270° lens cap, in accordance with LICOR recommendations. All height and width measurements were visually observed across ten different plants each site using measuring tape. Plant height was visually observed from the cotyledon to the apical meristem using a tape measurer. Leaf width was measured as the from the widest point on select leaves on each plant.

3.2.5. Eddy covariance data

Ground fluxes were quantified by installing one eddy covariance flux tower in each EC_a zone (pink and blue circles, Fig. 3.1b). The EC_a values immediately around the high EC_a and low EC_a flux towers are 88 and 52 mS m^{-1}, respectively, resulting in clay content values of 466 and 296 g kg^{-1}, a difference of 170 g kg^{-1} or 17 % (Stanislav,

2010). All equipment installed on the eddy towers were the same at both locations, and sensor details are given in Table 3.2. High frequency data includes a three dimensional sonic anemometer to measure 3D wind velocity components, and an infrared gas analyser to measure water concentrations. LE (in W m^{-2}) from the eddy flux towers are calculated over a given sampling interval using the following equation:

$$LE = \lambda(\rho\overline{w'c'}) \quad \text{(Eq. 3.8)}$$

where ρ is the density of air (kg m^{-3}), and $\overline{w'q'}$ is the covariance between vertical wind speed (w, m s^{-1}) and the mass fraction of vapor flux (c, kg water kg^{-1} air). H (in W m^{-2}) is similar to Eq. 3.8 except it calculates the covariance between w and sonic temperature (T), the latter of which is a proxy for T_a (in Kelvin or K):

$$H = \rho C_p \overline{w'T'} \quad \text{(Eq. 3.9)}$$

where ρC_p is the volumetric heat capacity of air (J m^{-3} K^{-1}). Note from Table 3.2 that the heights of the net radiometer and gas analyzer/anemometer shifted on June 30, 2017 because the latter sensors at the high EC_a zone were interfering with the irrigation system. The direction of the anemometer at both EC_a sites was 160 degrees from true North, which reflects the prevailing wind direction based on previous weather station data (data not shown). Soil moisture values were calculated from a custom calibration developed within each EC_a zone (Leo Rivera, METER Group, personal communication, 2017). Surface G flux was calculated by correcting the subsurface heat flux for storage in the soil layer above the plates using nearby temperature and moisture sensors (Evett et al., 2012).

Table 3.2 Measurands from the eddy covariance systems, along with their associated manufacturers.

Observed variable	Height/depth of measurand	Logging interval	Instrument
	Height (m)		
Wind speed and direction Water vapor concentration	High EC_a: 2.84 (before 6/30); 2.77 (after 7/1) ; Low EC_a 2.77	20 Hz	CSAT-3; Campbell Scientific, Logan, UT LI-7500; LI-COR, Lincoln, NE
Net radiation	High EC_a: 2.52 (before 6/30); 2.37 (after 7/1) ; Low $EC_{a:}$ 2.35		NR01, Hukseflux, The Netherlands
Air temperature and relative humidity	2.26	15 minutes	HC2S3, Campbell Scientific
	Depth (cm)		
Soil temperature	2, 6		105E; Campbell Scientific
Soil heat flux	8		HFT3-L; Campbell Scientific
Soil moisture	4, 5		GS1, METER Group Inc., Pullman, WA

High frequency raw data collected by the eddy covariance towers were then post-processed within eddyPro software version 6.2.1 (LI-COR). Processing was performed using eddyPro basic settings to quality check raw data, remove potential outliers, and apply corrections (Sharma et al., 2019). After eddyPro processing, turbulent fluxes were corrected by an additional 10 %, based on recent findings of underestimates in vertical velocity using a non-orthogonal CSAT-3 anemometer such as the case here (Kochendorfer et al., 2012; Frank et al., 2013). The average energy balance closure for each tower before and after correction is shown in Table 3.3. The average closure across all dates and towers after the correction methods above was 0.90. Across all dates and

towers, energy closure after correction was above 80 %, and this falls in line with closures reported from previous studies (Chávez et al., 2005; Xia et al., 2016).

Table 3.3 Closure ratio (i.e. $\frac{LE+H}{Rn-G}$) before and after applying corrections (i.e. LE * 1.1, H * 1.1) to EddyPro fluxes. July 18 fluxes at the high EC_a site are omitted here, as the anemeometer within the high EC_a zone was "looking at" a poorly vegetated part of the field.

Date	Closure Ratio - unclosed		Closure Ratio - closed with 1.1	
	High EC_a	Low EC_a	High EC_a	Low EC_a
June 16, 2017	0.86	0.85	0.94	0.93
July 1, 2017	0.80	0.94	0.88	0.98
July 18, 2017	N/A	0.78	N/A	0.85
July 26, 2017	0.82	0.77	0.91	0.94

3.2.6. Model formulations

3.2.6.1. TSEB-PT

TSEB-PT models were developed out of a need to estimate T_c from coarse (i.e. > 60 m) satellite pixel resolutions (Kustas et al., 2004). Primary equations used in TSEB-PT include Eq. 3.3, along with an initial approximation of LE_c based on the Priestley and Taylor (1972) transpiration equation:

$$LE_c = \alpha_{PT} f_g \frac{\Delta}{\Delta + \gamma} R_{n,c}, \quad \text{(Eq. 3.10)}$$

where α_{PT} is Priestley–Taylor parameter with an initial value of 1.26, Δ is the slope of the saturation vapor pressure-temperature curve (Pa K^{-1}) and γ is the psychrometric constant (Pa K^{-1}). A more detailed description of this model can be found from Norman

et al. (1995) and Kustas and Norman (1999). After LE_c is initialized using Eq. 3.10, H_c is then found by rearranging Eq. 3.2a (assuming $R_{n,c}$ is calculated via ground truth info). With an initial H_c estimate obtained, T_c is found by rearranging the initial formulation for H_c (Norman et al., 1995):

$$H_c = \rho C_p \frac{T_c - T_a}{r_a} \rightarrow T_c = \frac{H_c r_a}{\rho C_p} + T_a, \quad \text{(Eq. 3.11)}$$

where r_a is the aerodynamic resistance to momentum and heat transfer (s m^{-1}), ρC_p is the volumetric heat capacity of air (J m^{-3} K^{-1}). With an initial T_c from Eq. 3.11, T_s is then obtained by rearranging Eq. 3.3. Note that, in order to obtain an initial T_c value, f_c (Eq. 3.3) is calculated from Campbell and Norman (1998):

$$f_c(\theta) = 1 - \exp\left[\frac{-0.5\Omega(\theta)LAI}{\cos(\theta)}\right], \quad \text{(Eq. 3.12)}$$

where Ω is a vegetative clumping factor calculated at a given sensor viewing angle θ (Kustas and Norman, 1999), and *LAI* is calculated from multispectral imagery (Sect. 3.2.7.1).

A check on these T_c (Eq. 3.11) and T_s (Eq. 3.3) values is then performed by applying the newly found T_s values towards H_s:

$$H_s = \rho C_p \frac{T_s - T_a}{r_s + r_a}, \quad \text{(Eq. 3.13)}$$

where r_s is the soil resistance to momentum and heat transfer (s m^{-1}). Finally, LE_s is found from Eq. 3.2b, given H_s (Eq. 3.13). A valid solution is reached when LE_s is positive – this is because, during the daytime (i.e. when a flight occurs), moisture is expected to move from the soil/canopy to the atmosphere. If LE_s is not positive, α_{PT} is

iteratively reduced until LE_s is zero or positive. If a valid solution is found, LE and H fluxes from both canopy and soil sources are respectively added together to compute the LE and H terms shown in Eq. 3.1.

3.2.6.2. TSEB-DTD

One documented issue with TSEB-PT is that T_r measurements can be negatively affected by sources of error such as radiometric calibration, the influence of sensor temperature, vignetting, non-uniformity noise, correction for atmospheric effects, target ε, and distance from the target (Kelley et al., 2019). The TSEB-DTD model, developed by Anderson et al. (1997), and refined by Norman et al. (2000), was formulated to eliminate dependence on absolute T_r measurements. TSEB-DTD is similar to the TSEB-PT formulation in that H_c is calculated similar to the steps in Sect. 3.2.6.1. However, instead of finding H_s using single measurements of T_s (Eq. 3.13), H_s is instead found by rearranging the H equation:

$$H_s = H - H_c, \qquad \text{(Eq. 3.14)}$$

H is calculated by utilizing relative temperature difference between an AM thermal survey and mid-day time thermal survey collected on the same day (Norman et al., 2000):

$$H_i = \rho c_p \left[\frac{(T_{r,i}(\theta) - T_{r,0}(\theta)) - (T_{a,i} - T_{a,0})}{\left(1 - f_c(\theta)\right)\left(r_{a,i} + r_{s,i}\right)}\right] + H_{c,i}\left[1 - \frac{f_c(\theta)}{1 - f_c(\theta)}\frac{r_{a,i}}{r_{a,i} + r_{s,i}}\right], \qquad \text{(Eq. 3.15)}$$

where the subscripts '*i*' and '*0*' refer to the surveys collected at the daytime and morning, respectively. Thus, T_a and T_r are needed shortly after sunrise in order calculate

H_s to complete the two-component energy balance equations (Eq. 3.2). The standard time to collect AM surveys is about 1.5 hours after sunrise, while mid-day surveys should be collected about 5.5 hours after sunrise; however, the selection of these two times is not a steadfast rule and can be seasonally dependent (Anderson et al., 1997).

3.2.6.3. TSEB-2T

A recent model developed within the TSEB suite is the hybrid TSEB for component temperature estimation model (or TSEB-2T, Nieto et al., 2018b). The motivation for TSEB-2T was made possible through developments in UAV technology, as T_c and T_s could be directly extracted, as opposed to estimated via the assumptions from TSEB-PT. TSEB-2T, unlike TSEB-PT, uses no initial assumptions of LE_c, and, unlike TSEB-DTD, uses absolute (instead of relative) temperatures. However, running the model under the TSEB scheme requires knowledge of both T_c and T_s for each pixel, and such temperatures are not likely to exist within a single pixel. In this case, canopy and soil temperatures are obtained by searching for pure vegetation and soil pixels in a contextual spatial domain - that is, within a specified search window, pixels identified as canopy and soil are respectively averaged to find T_c and T_s. Pixels are classified as soil and canopy based on thresholds associated with $NDVI_s$ or $NDVI_{max}$. $NDVI_s$ was obtained by performing a supervised classification on the NDVI image obtained shortly after planting (May 15) – then, all NDVI pixels classified as soil were averaged. However, because the field contains soil variability (Fig. 3.1b), the mean plus two standard deviations was used to obtain an upper threshold for $NDVI_s$ (0.310). The $NDVI_{max}$ threshold value was the mean value of pixels classified as pure vegetation using a

supervised classification of the NDVI imagery obtained around the peak vegetation growth (July 18, 0.916). Further discussion regarding derivation and implementation of TSEB-2T can be found from Nieto et al. (2018b).

3.2.6.4. DATTUTDUT

The DATTUTDUT is an energy balance model created by Timmermans et al. (2015) that primarily estimates Eq. 3.1 using T_r, and thus thermal imagery, as input. Model formulation for each component of Eq. 3.1 will be provided here. R_n is the difference between all incoming and outgoing radiation:

$$R_n = (1 - \rho_0) * R_{sd} + \varepsilon_0 * \varepsilon_a * \sigma * T_a^4 - \varepsilon_0 * \sigma * T_r^4, \quad \text{(Eq. 3.16)}$$

where ρ_0 is the surface albedo (unitless), ε_0 is the surface emissivity (unitless), ε_a is the atmospheric emissivity (unitless), and σ is the Stefan–Boltzmann constant (5.67×10^{-8} W m^{-2} K^{-4}). SW_{in} is modelled within DATTUTDUT using sun-earth geometry relationships, although recent formulations have also used local net radiometer (i.e. SW_{in}) data (Brenner et al., 2018). ε_0 in the model is assumed to equal unity or one. T_a is usually assumed to be the minimum temperature value unless local data are supplied. ε_a is estimated differently depending on whether direct T_a measurements are supplied (Brutsaert et al., 1982; Timmermans et al., 2015). G is a fraction of R_n and is linearly related with T_r, based on scaling between its minimum (0.05 within full vegetated areas) and maximum (0.45 for bare soils):

$$G = R_n * \left[0.05 + 0.4 * \left(\frac{T_r - T_{r,min}}{T_{r,max} - T_{r,min}}\right)\right], \quad \text{(Eq. 3.17)}$$

$T_{r,max}$ refers to the hottest pixel (defined here as 100th percentile), and $T_{r,min}$ to the temperature at the 0.5th percentile (Timmermans et al., 2015). LE is found through the evaporative fraction (EF) or $T_{r,max}$ and $T_{r,min}$, with the assumption that the energy balance equation is properly conserved:

$$EF = \frac{LE}{LE + H} = \frac{LE}{R_n - G} = \frac{T_{r,max} - T_r}{T_{r,max} - T_{r,min}}, \quad \text{(Eq. 3.18a)}$$

LE is then found by rearranging Eq. 3.18a as

$$LE = \left(\frac{T_{r,max} - T_r}{T_{r,max} - T_{r,min}}\right) * (R_n - G), \quad \text{(Eq. 3.18b)}$$

Assuming R_n, G, and LE have been found using Eq. 3.16, 3.17, and 3.18b, respectively, H is then obtained as a residual by rearranging Eq. 3.1.

3.2.7. Model inputs and processing

Model outputs were generated at 1.05 m, and 10.05 m. The 1.05 m scale refers to the minimum pixel resolution that permits the use of TSEB modelling, while the 10.05 pixel resolution corresponds with the spatial scale of management operations such as central pivot irrigation (Smith et al., 2009). Ancillary image inputs (described below) are assumed to be aggregated from the original UAV resolutions (Table 3.1) using simple linear averaging. Agronomic and weather inputs at the times of each overpass are listed in Table 3.4.

Table 3.4 Agronomic and weather data collected at the IOPs listed in Table 3.1. f_g, or green fraction, was assumed to be equal to 1 for all dates of interest. The view zenith angle was also to be equal to 0 in all cases. T_a – air temperature; u – wind speed; S_{dn} – downward incoming solar radiation; VPD – vapor pressure deficit; RH – relative humidity.

Date	Field Average LAI	Canopy height	Canopy width	Thermal AM T_a	Thermal PM T_a	u	Wind direction	S_{dn}	VPD	RH
	$m^2\ m^{-2}$	(m)	(m)	K	K	m/s	°	$W\ m^{-2}$	hPa	
June 16, 2017	1.03	0.44	0.43	298.9	306.1	3.88	205	1014	24.0	0.49
July 1, 2017	1.72	0.61	0.66	300.4	306.4	3.50	162	801	22.9	0.50
July 18, 2017	2.37	0.78	0.92	301.1	305.9	1.00	256	1053	20.5	0.50
July 26, 2017		0.80	0.93	299.3	306.0	2.75	176	963	21.5	0.49

3.2.7.1. Image inputs

Image inputs refer to spatially variable inputs beyond T_r, such as f_c and LAI. f_c and LAI were needed for TSEB modelling. f_c was derived from NDVI imagery by scaling between maximum NDVI ($NDVI_{max}$) and soil NDVI ($NDVI_s$) (Carlson and Ripley, 1997):

$$f_c = \left(\frac{NDVI - NDVI_s}{NDVI_{max} - NDVI_s}\right)^2 \quad \text{(Eq. 3.19)}$$

$NDVI_{max}$ was taken to be the maximum NDVI observed from the native pixel resolution (0.976). $NDVI_s$ was based off average NDVI values at a time before squaring occurred (0.2). LAI maps were then generated by regressing in situ LAI (Fig. 3.1b) against these newly generated f_c maps. UAV-based LAI maps were then compared with hand measured LAI values from a select holdout sample (n = 5) across all IOPs. These five samples were located nearby the two eddy flux towers. The average percent error between predicted and measured LAI was 7.3 %. Field canopy height and width values

were obtained by averaging spatially distributed field measurements (Fig. 3.1b) at each IOP. Green vegetation fraction was set to one for all model runs.

3.2.7.2. Non-image inputs

Weather data was collected using 15-minute averaged data obtained across both eddy flux towers. Weather parameters include: 1) T_a (K), 2) wind speed (m s^{-1}), 3) barometric pressure (mbar), 4) e_a (mbar), 5) SW_{in} (W m^{-2}) and 6) incoming longwave radiation (LW_{in}) (W m^{-2}). Leaf spectral properties were obtained using local ground-truth reflectance data. Leaf angle distribution was calculated from leaf tip angle measurements collected alongside LAI data (Wang et al., 2007). Modelled G flux was assumed to be a constant ratio between G and soil net radiation ($R_{n,s}$), the latter of which was calculated using formulations provided by Kustas and Norman (1999). The use of a constant $G/R_{n,s}$ was based on the observation that that most PM thermal UAV surveys were collected around solar noon - Kustas and Daughtry (1990) suggest that the use of a constant ratio is appropriate for several hours around solar noon, after which a time lag exists between R_n and G.

3.2.7.3. Model runs

All non-contextual or hybrid models (i.e. TSEB-PT, TSEB-DTD, TSEB-2T) were run within the Python package pyTSEB, version 2.0 (Nieto et al., 2019). The DATTUTDUT model was coded and run using a custom-made function within the R software program (R Core Team, 2018), given the formulations from Timmermans et al. (2015). Because previous studies have used varying degrees of weather inputs for DATTUTDUT modelling (Brenner et al., 2018), DATTUTDUT model versions were

separated into those without inputs and those with all inputs, where inputs are defined in terms of SW_{in}, e_a and $T_a - e_a$ and T_a were also included because these parameters are collected concurrently with SW_{in}.

3.2.7.4. Footprints

The footprint of the fluxes measured by the eddy covariance tower describes the source area of the fluxes depending on parameters such as wind direction, wind speed, and atmospheric stability (Burba and Anderson, 2010). In order to effectively compare the UAV and eddy tower fluxes, footprints need to be generated in two-dimensional coordinate space. In this study, footprints were calculated using the 2-D footprint models developed by Detto et al. (2006). UAV predicted fluxes were averaged within each footprint using the source weighted scheme proposed by Li et al. (2008):

$$\overline{UAV\ Flux} = \frac{\sum_{i=1}^{n} f(x_i, y_i, z_m) FLUX(x_i y_i)}{\sum_{1}^{n} f(x_i, y_i, z_m)}, \quad \text{(Eq. 3.20)}$$

where *i* is a given pixel with location x_i, y_i, given the flux tower height z_m. Note that each i^{th} pixel has an associated weight (i.e. $f(x_i,y_i,z_m)$) dependent on lateral diffusion characteristics (Schmid, 1994) and the original 1-D footprint model from Hsieh et al. (2000).

3.2.8. Model evaluation

Agreement between modelled and measured R_n, G, H and LE were compared in terms of MAE, mean absolute percent error (MAPE), mean bias error (MBE) and mean bias percent error (MBPE):

$$MAE = \frac{1}{n}\sum_{j=1}^{n}|\hat{y} - y| \quad \text{(Eq. 3.21a)}$$

$$MAPE = \frac{100}{n}\sum_{j=1}^{n}\left|\frac{\hat{y} - y}{y}\right| \quad \text{(Eq. 3.21b)}$$

$$MBE = \frac{1}{n}\sum_{j=1}^{n}\hat{y} - y \quad \text{(Eq. 3.21c)}$$

$$MBPE = 100\frac{\sum_{j=1}^{n}\hat{y} - y}{\sum_{j=1}^{n} y} \quad \text{(Eq. 3.21d)}$$

where $\hat{y}$ and y are the UAV modelled and eddy covariance fluxes, respectively. In the case of MBE, positive and negative values mean overestimation and underestimation, respectively.

In addition to the above performance statistics, UAV flux estimates were evaluated with respect to soil type (i.e. EC_a zone). The question that is being addressed is as follows: does modelled LE (either using TSEB or DATTUTDUT) significantly differ by soil type? An ANOVA was conducted comparing two specific models:

$$Modelled\ LE \sim LAI : Water\ Depth, \quad \text{(Eq. 3.22a)}$$

$$Modeled\ LE \sim LAI : Water\ Depth : EC_a\ Zone, \quad \text{(Eq. 3.22b)}$$

These two models were generated at all pixel resolutions using an independent set of sample observations (select green circles, Fig. 3.1b) consisting of LAI and water depth measurements collected throughout the growing season. Differences between models were deemed significant when the ANOVA p-values were less than 0.05.

3.3. Results and discussion

3.3.1. Agronomic, soil moisture, and remotely sensed data

Figs 3.3 is a plot from data collected at the agronomic collection sites throughout the growing season. Fig. 3.3 shows biomass variations by IOP and EC_a flux tower. The maximum LAI observed within source footprints was 2.87 m^2 m^{-2} on July 26. During flowering (i.e. June 16), the mean LAI near the low EC_a flux tower was slightly higher than within the high EC_a tower (1.13 and 1.05 m^2 m^{-2}, respectively). During cutout (i.e. July 1), the mean LAI values were similar across both EC_a zones. The mean LAI values on 18 to July 26 were relatively large within the high EC_a zone, indicating canopy growth in this zone lagged slightly behind that of low EC_a. High EC_a LAI zone measurements were consistently characterized by larger standard deviations throughout the growing season.

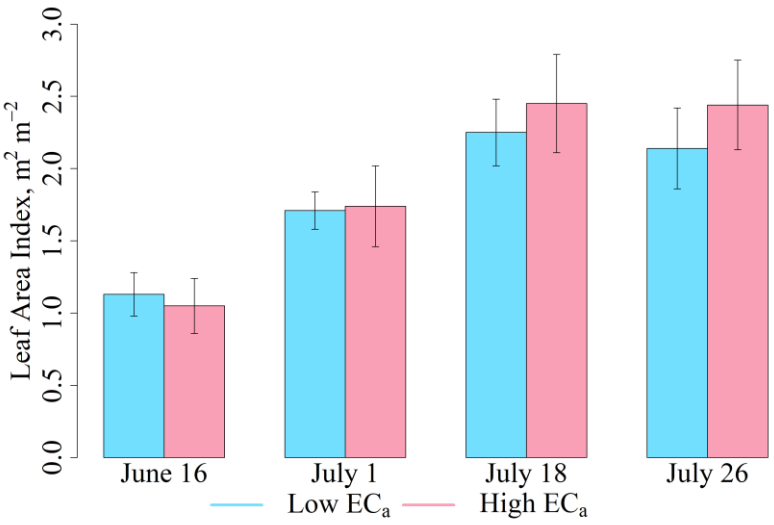

Fig. 3.3 Source area LAI (m^2 m^{-2}) by date. Source area refers to the footprint defined by the flux towers on each intense observation period.

Fig. 3.4 shows the depths of soil water averaged within each EC_a zone. NMM soil moisture measurements are based on all point samples located within each EC_a zone (Fig. 3.1b). The initial depths of water within the high and low EC_a zones were 324 and 267 mm per 100 cm soil depth, respectively. The differences in water depth between EC_a zones were most pronounced at the end of the growing season, notably on July 26. Overall, the difference in depth of soil water at both high and low EC_a sites was 49 mm and 80 mm, respectively over the entire season. A two-sample t-test found that the depth of soil water was significantly different between both EC_a groups ($p < 0.001$).

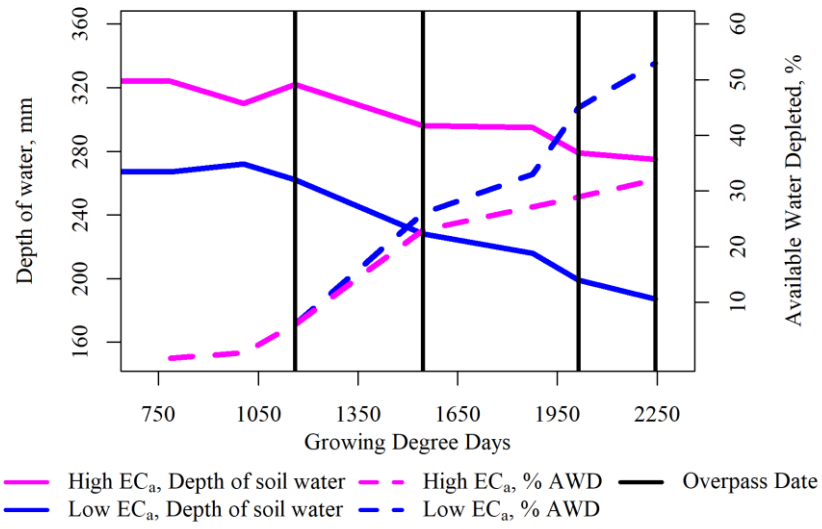

Fig. 3.4 Depth of soil water (in mm, left y-axis) and percent available water depletion (in %, right y-axis, Eq. 3.3) averaged within different EC_a zones (Fig. 3.1b) by growing degree days. Vertical black lines correspond to the Intense Observation Period (IOP) dates listed in Table 3.1.

Fig. 3.4 also shows estimates of AWD (Eq. 3.7). AWD begins at zero percent on the first of measurements (786 GDD, May 31) and ends at 32 or 53 % on the last set of measurements (2246 GDD, July 26). During June 16 to July 1 (1161-1545 GDD), AWD was similar across both EC_a zones, most likely because of lower vegetative demand for water. After July 1, or cutout, a divergence in the AWD curves can be observed. In particular, the amount of soil water (i.e. high AWD) within low EC_a was lower than that from high EC_a, even though its absolute amount (i.e. depth of water) was relatively low. The reason for these results may stem from differences in clay content (and thus water holding capacities) observed between both EC_a zones (Sect. 3.2.1).

3.3.2. Eddy covariance data

Before investigating the modelled outputs, it was deemed important to first inspect the quality of the eddy covariance data. Most winds were sourced around the anemometer orientation (160 degrees), and almost half of the winds were at two spokes centered either at 135 (112.5-157.5) or at 180 (157.5-202.5) degrees. Within these two spokes, around half of the winds had speeds were sourced between 2-4 m s^{-1}, which suggests the fluxes are sufficiently turbulent, one key assumption of the method (i.e. > 1 m s^{-1}, Monin and Obukhov, 1954; Burba and Anderson, 2010). Based on observations of turbulent fluxes, as well as previously reported closure results (Table 3.3), the eddy covariance towers used in this study can be used as a reliable source for validating UAV-based fluxes.

Fig. 3.5 shows diurnal fluxes as measured from the eddy covariance towers on the given IOP dates from Table 3.1. On the left column, the available energy (plus SW_{in}) is presented, and on the right column the turbulent fluxes (LE, H) plus the evaporative fraction ($EF = \frac{LE}{LE+H}$) are presented. The July 18 fluxes within the low EC_a site are not included in Fig. 3.5 because its source area was located within sparsely covered vegetation – a low EC closure ratio supports this finding (0.64). The maximum SW_{in} observed across these four IOP dates was 1100 W m^{-2} on July 18. The jaggedness of both SW_{in} and R_n diurnal curves can be observed on most IOP dates, indicating partly cloudy conditions (Fig. 3.5a, 5c, 5e, 5f). This variability in cloud cover, therefore, influenced the decision to validate UAV fluxes at 15 minutes instead of the more commonly used 30 minutes (Foken et al., 2008). UAV surveys were conducted under

sunny skies except on July 1, and a dip in SW_{in} supports this observation (Fig. 3.5c). The clouds were thin, but consistent, throughout the UAV thermal survey on this date. However, the presence of these clouds did not significantly affect the energy closure compared with other IOPs, as the energy closure ratio was still above 0.80 for both flux towers even before the correction was applied (Table 3.3).

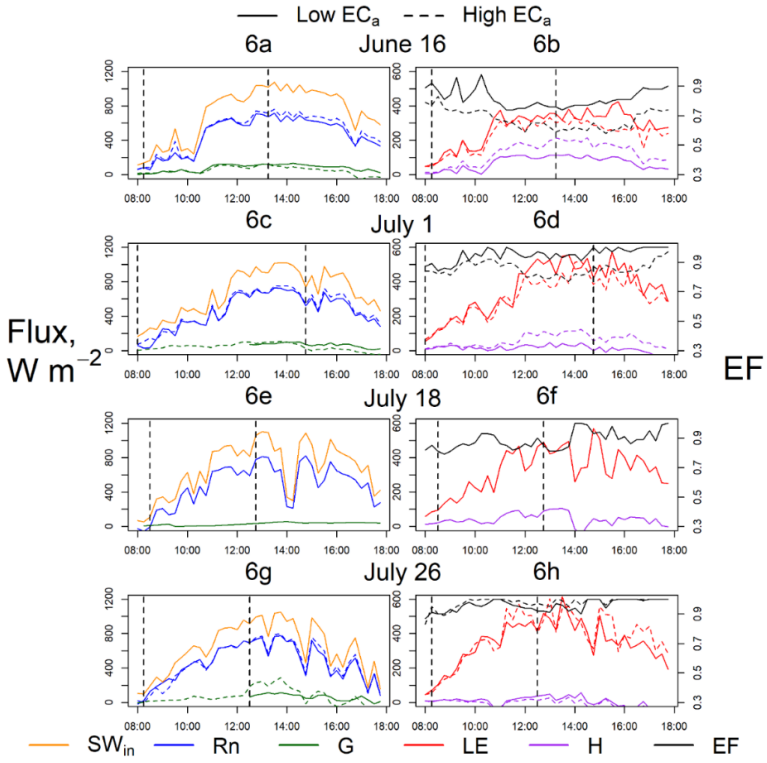

Fig. 3.5 Diurnal fluxes obtained from eddy covariance towers across all intense observation periods. Left and right y-axis values express fluxes in terms flux density (W m^{-2}) and evaporative fraction (EF, unitless). Vertical black lines correspond to the Intense Observation Period (IOP) dates listed in Table 3.1. The available energy plots (first column) are displayed on a different scale than the turbulent fluxes (second column). July 18 fluxes at the high EC_a zone are omitted, as the eddy towers were "looking at" a poorly vegetated part of the field. Some of the soil heat flux data was unavailable in the early morning due to sensor malfunction.

In comparing the diurnal fluxes by EC_a flux tower, several patterns emerge. Across all dates, the daytime R_n was slightly higher within the high EC_a tower. These differences were prominent, for example, during flowering (June 16), as the peak R_n values within the low and high EC_a towers were 716 W m^{-2} and 759 W m^{-2}, respectively (Fig. 3.5a). The reason for this result can be explained by differences in albedo, where peak albedo measured within high and low EC_a sites were 0.17 and 0.22, respectively. With time in the growing season, however, the difference in R_n magnitude by towers diminished, most likely due to increased vegetation growth and lessening influence of the soil background Fig. 3.3, Fig. 3.5c, 3.5e, 3.5g). The overall magnitude of G was relatively low and do not appear to significantly lag behind that of the R_n diurnal curves. Median G/R_n shifted from 0.17 (June 16) to 0.05 (July 18) at the low EC_a site, while median G/R_n only changed from 0.12 (June 16) to 0.11 (July 18) at the high EC_a.

As expected, the partitioning of diurnal turbulent fluxes shifted in time due to changes in the vegetation cycle (Fig. 3.5b, 3.6d, 3.6f, 3.6h). Relative to other dates, H during early flowering stages (i.e. June 16) were close with LE in magnitude, corresponding with EF values as low as 0.6 (Fig. 3.5b). The maximum LE recorded from these four IOP dates was ~ 600 W m^{-2} on July 26 (Fig. 3.5h). This period was characterized by relative drought (1161-1425 GDD, Fig. 3.2b), a time probably driven more by availability of soil moisture than energy (Gevaert et al., 2018). During boll filling and initial boll opening stages (July 18 and July 26), the EF was at a maximum across all dates (0.90 or greater) (Fig. 3.5f, 3.6h). Diurnal H was greater within high than

low EC_a on June 16 and July 1 (Fig. 3.5b, 3.6d), and this trend was flipped on July 26. A similar set of patterns emerge with respect to EF, although this time high EC_a EF would eventually surpass that of low EC_a (Fig. 3.5b, 3.6d, 3.6h). However, the differences in EF by EC_a flux tower are lower on July 26 than those on June 16 or July 1 (Fig. 3.5b, 3.6d, 3.6h).

3.3.3. Comparison of model estimates and tower data

3.3.3.1. UAV vs. flux towers, across EC_a zones

The purpose of this section is to: 1) compare non-contextual and contextual model estimates with respect to eddy flux towers, 2) address the effect of increasingly coarse pixel resolutions on flux estimations, and 3) quantify the effect of adding local weather inputs to DATTUTDUT models. Table 3.5 shows the MAE and bias errors for R_n, G, and H across all TSEB and DATTUTDUT models, both at 1.05 and 10.05 m pixel resolution. Fig. 3.6 shows plots of UAV (at 1.05 m) versus eddy covariance for R_n (triangles), G (squares), and H fluxes (diamonds) fluxes, either by pooling (i.e. high EC_a/low EC_a, left column) or separating (right column) analysis points by EC_a zone. The July 18 results are only from the low EC_a tower and are only included, therefore, in Fig. 3.6a, 3.6c, 3.6e, 3.6g, and 3.6i – July 18 high EC_a fluxes are not shown in this study because of poor flux closure at that flux tower. Turbulent eddy flux measurements (i.e. H, LE) are assumed to be closed using the 1.1 correction factor described earlier (Sect. 3.3.2.5.).

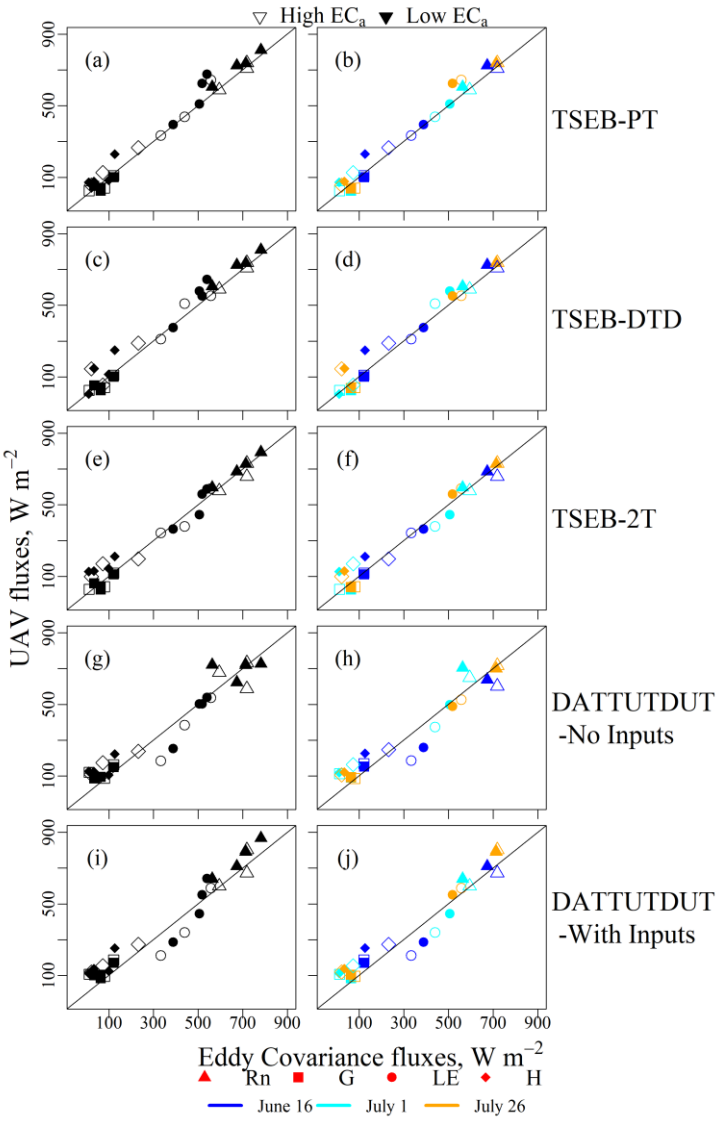

Fig. 3.6 UAV modeled latent heat (LE) fluxes (y-axis) at 1.05 m pixel resolution against eddy covariance LE fluxes (x-axis) across all intense observation periods.

Table 3.5 R_n, G, and H flux error assessment between eddy covariance and UAV modeled fluxes, either from non-contextual or contextual models (in W m^{-2}). Values in parentheses are MAE and bias, respectively, as percentage (%) of measured fluxes. Metrics are reported from pooling analysis from low and high EC_a zones and measurement days (n = 7). All metrics except for percent error, and MSE_u/MSE are assumed to be in units of W m^{-2}.

Resolution (m)	R_n - MAE	R_n - Bias	G - MAE	G - Bias	H -MAE	H -Bias
			TSEB-PT			
1.05	26 (4)	22 (3)	25 (52)	-16 (-22)	50 (> 100)	45 (53)
10.05	26 (4)	23 (3)	25 (52)	-16 (-22)	47 (> 100)	42 (49)
			TSEB-DTD			
1.05	26 (4)	22 (3)	24 (52)	-15 (-22)	65 (> 100)	58 (69)
10.05	27 (4)	23 (3)	25 (52)	-16 (-22)	60 (> 100)	52 (61)
			TSEB-2T			
1.05	23 (3)	2 (0)	22 (55)	-10 (-14)	79 (> 100)	69 (81)
10.05	24 (4)	8 (1)	23 (58)	-9 (-13)	105 (> 100)	81 (96)
			DATTUTDUT - No Inputs			
1.05	59 (9)	46 (7)	50 (> 100)	50 (71)	83 (> 100)	83 (97)
10.05	74 (11)	-10 (-2)	63 (> 100)	63 (89)	80 (> 100)	80 (74)
			DATTUTDUT - All Inputs			
1.05	71 (11)	4 (1)	43 (> 100)	43 (60)	72 (> 100)	72 (85)
10.05	71 (11)	0 (0)	58 (> 100)	58 (82)	97 (> 100)	97 (> 100)

In terms of R_n, TSEB-PT, TSEB-DTD, and TSEB-2T R_n MAE errors were very similar and between 2-27 W m^{-2} or 0-4 % (Table 3.5). DATTUTDUT models, on the other hand, had higher R_n errors (between 59-74 W m^{-2} or between 9-11 %, Table 3.5). The model that produced the highest amount of R_n bias was DATTUTDUT without inputs at 1.05 m (46 W m^{-2} or 7 % bias, Table 3.5, Fig. 3.6i-3.6.j). Errors in DATTUTDUT R_n have previously been attributed to simplifications, for example, of surface albedo and ε (Xia et al., 2016). MAPE values were similar between DATUTTDUT models when adding or removing weather inputs, for both pixel resolutions (9-11 %, Table 3.5). Adding weather inputs to DATTUTDUT, however, did

reduce R_n bias at 1.05 m (from 46-4 W m^{-2}). Outside of individual models, R_n MAPE and MBPE values were generally under 10 % across all pixel resolutions and did not change very much with increased pixel size (outside of the DATTUTDUT – No Inputs model, Table 3.5). Relative to G and H, R_n produced the lowest MAPE and MBPE values across all models and resolutions. This result may have occurred because R_n is more sensitive to solar radiation than vegetation and soil objects (Sridhar et al., 2003). As a result, most of the UAV R_n estimates were close to the 1:1 line for all models (Fig. 3.6, triangles).

Out of all the components estimated from Eq. 3.2, H had the highest MAE and highest biases (Table 3.5). Other studies have also observed H to be a difficult energy balance component to estimate as well (Ortega-Farias et al., 2016; Brenner et al., 2017). H errors often result from inequalities between radiometric (i.e. sensor) and aerodynamic (i.e. model) temperatures, especially when soils are much warmer than canopies (up to 42 °C difference from field data here) (Norman and Becker, 1995; Chehbouni et al., 1996; Kustas et al, 2004). While R_n errors were fairly similar between non-contextual and contextual models, such was not the case for H. For example, at 1.05 m, the models in terms of H MAE errors were (from smallest to largest): TSEB-PT (50 W m^{-2}), TSEB-DTD (65 W m^{-2}), DATTUTDUT with inputs (72 W m^{-2}), and TSEB-2T (79 W m^{-2}), and DATTUTDUT without inputs (83 W m^{-2}). In general, TSEB models were better predictors of H than both DATTUTDUT models, although all models had MAPE values over 100 %.

G flux errors generally lie in between that of R_n and H, and TSEB G errors, like H, were lower than that from both DATTUTDUT models (Table 3.5). G fluxes were consistently underestimated and overestimated for TSEB and DATTUTDUT models, respectively (-9 to -16 W m^{-2}, 43-58 W m^{-2} Table 3.5). The most likely source of G error is from differences in measurement areas and, therefore, soil physical properties between the UAV and eddy covariance methods (Foken et al., 2008). Another source of error in G could be from differences in heat conduction between the soil and air in G response, relative to instantaneous UAV measurements (Gentine et al., 2012; Hoffmann et al., 2016).

Fig. 3.6 shows also plots of UAV versus eddy covariance LE fluxes at 1.05 m (circles). Table 3.6, like Table 3.5, quantifies the pooled results from Fig. 3.6, except this time for LE. The reported MAE errors across all models and pixel resolutions range from 40-150 W m^{-2}, or 8-37 % (Table 3.6). The reported bias values range from -107-52 W m^{-2} or -24-11 %. TSEB-PT and TSEB-DTD models overestimated LE, while DATTUTDUT models underestimated LE (Fig. 3.6, Table 3.6). TSEB and DATTUTDUT models performed better in modelling LE than H and G, based on comparison of MAPE values from Tables 3.5 and 3.6. In the case of TSEB models, this may have occurred because G and H behave in an inverse manner before estimating LE (Eq. 3.2), where G and H were underestimated and overestimated, respectively (Table 3.5). The G and H errors within the DATTUDUT model, however, do not necessarily cancel out, as the model instead estimates H last (instead of LE, Sect. 3.2.6.4.).

Table 3.6 LE flux error assessment between eddy covariance and UAV modeled fluxes, either from non-contextual or contextual models. Metrics are reported from pooling analysis from low and high ECa zones (n = 7). All metrics except for percent error, and MSE_u/MSE are assumed to be in units of W m^{-2}. TSEB-2T model results at native resolution are not available because the model requires aggregated imagery.

Resolution (m)	MAE	Bias
TSEB-PT		
1.05	49 (9)	49 (10)
10.05	53 (10)	53 (11)
TSEB-DTD		
1.05	46 (10)	35 (7)
10.05	53 (11)	43 (9)
TSEB-2T		
1.05	40 (8)	-2 (0)
10.05	81 (18)	-9 (-2)
DATTUTDUT - No Inputs		
1.05	54 (14)	-54 (-12)
10.05	99 (24)	-99 (-21)
DATTUTDUT - All Inputs		
1.05	78 (18)	-31 (-7)
10.05	150 (37)	-107 (-24)

The average MAPE values across all models were 12 and 20 % at 1.05 m and 10.05 m pixel resolutions, respectively. These average errors are just as accurate as those reported with the eddy covariance technique (5-20 %, Foken, 2008), and are in line with results reported from previous studies (Neale et al., 2012; Ortega-Farias et al., 2016; Xia et al., 2016). Model results also suggest that LE modelled fluxes were robust to uniformly cloudy conditions from the July 1 thermal survey (Table 3.1), as little scatter was observed on that date (Fig. 3.6b, 3.6d, 3.6f, 3.6h, 3.6j). One reason why these

positive results may have occurred across all models is because UAV thermal surveys were collected under a relatively short acquisition period (~13 minutes), implying generally constant radiative conditions. In fact, most models had MAPE values less than 20 % (Table 3.6). One exception to this generalization, however, was observed from DATTUTDUT models at 10.05 m, which most likely occurred from uncertainty in endmember selection (Section 3.3.4.).

The most accurate model(s) towards estimating LE depended on the pixel resolution in question. For example, at 1.05 m the most accurate models were TSEB-PT, TSEB-DTD, and TSEB-2T models (around 40-49 W m^{-2} or 8-10 %), followed by the DATTUTDUT models (54-78 W m^{-2} or 14-18 %, Table 3.6). At 10.05 m, the model accurate models were TSEB-PT and TSEB-DTD (53 W m^{-2} or 10-11 %), TSEB-2T (81 W m^{-2} or 18 %), DATTUTDUT without inputs (99 W m^{-2} or 24 %), and finally DATTUTDUT with inputs (150 W m^{-2} or 37 %). Relative scatter for LE flux estimation across both DATTUTDUT models can be observed (Fig. 3.6). The LE bias for TSEB models were greatest and smallest within TSEB-PT and TSEB-2T models, respectively. For example, at 10.05 m the percent bias error for TSEB-PT and TSEB-2T was ten and zero percent, respectively (Table 3.6). Despite some biases within TSEB models, however, they generally outperformed DATTUTDUT in terms of estimating LE. This result likely occurred because TSEB models (relative to DATTUTDUT) provide a better physical depiction of energy and radiative exchange for crops and soils (Xia et al., 2016).

3.3.3.2. UAV vs. flux towers, by EC_a zones

One additional objective in this study was evaluate how differences in spatially variable soil properties affect UAV-based ET flux estimates. The main soil property of interest here is soil moisture, which is moisture that can potentially evaporate within the root zone (Verstraeten et al., 2008). Soil moisture is characterized in terms of soil water depth from NMM data, expressed by EC_a zone and IOP (Fig. 3.4, Table 3.7). Differences in soil water depth by EC_a zone across IOP dates range from 60-88 mm (Table 3.7), and more water was used within the low EC_a zone than the high EC_a zone throughout the growing season (Fig. 3.4, dashed lines).

Table 3.7 Soil moisture differences expressed by depth of water and difference between EC_a zones using the data shown in Fig. 3.4.

Date	Depth of water (mm)	Water depth difference (mm)	EC_a Group
	262		Low
6/16/2017	322	60	High
	228		Low
7/1/2017	296	68	High
	199		Low
7/18/2017	279	80	High
	187		Low
7/26/2017	275	88	High

UAV modelled LE at each EC_a flux tower increased throughout the growing season and reached a peak on July 26 (Fig. 3.6, open/filled circles), which is due to increasing growth or LAI up to that point (Table 3.4). High EC_a modelled LE fluxes (open circles)

were only greater than low EC_a fluxes (closed circles) on July 26 (Fig. 3.6, right column). Both DATTUTDUT and TSEB models were not biased by soil type, given the limited sample size. For example, on June 16 and July 1 DATTUTDUT models underestimate LE similarly at both EC_a flux towers (Fig. 3.6h, 3.6j, open/filled circles).

In order to compare the modelling errors by soil type, LE results (Fig. 3.6) were combined to estimate MAPE by EC_a zone, as shown in Fig. 3.7. Note that the results from Fig. 3.7 refer to TSEB models only because these models were shown to outperform DATTUTDUT across both pixel resolutions (Table 3.6) – DATTUTDUT LE results will be separately discussed in Section 3.3.4. For both pixel resolutions, the MAPE values were lower within the high EC_a tower than the low EC_a tower, and this was particularly noticeable at 10.05 m (Fig. 3.7). While Fig. 3.7 indicates differences in accuracies between the two EC_a zones, it does not address whether these differences are statistically different. Therefore, ANOVA models were constructed to test this hypothesis (Sect. 3.2.8), and these results are provided in Table 3.8. At 1.05 m and 10.05 m, the p-values for all models are less than 0.05, indicating significant different models based on the soil type (or the EC_a zone) parameter. Therefore, there is initial evidence to suggest that TSEB LE model estimates (and thus ET) vary by soil EC_a zone, which could be due to differences in soil moisture use across time (Fig. 3.4, Table 3.7). This hypothesis would certainly support previous notions that spatial heterogeneity of soils, in particular soil water holding capacity, can affect the spatial pattern of LE within a given production field (Hatfield and Preuger, 2011).

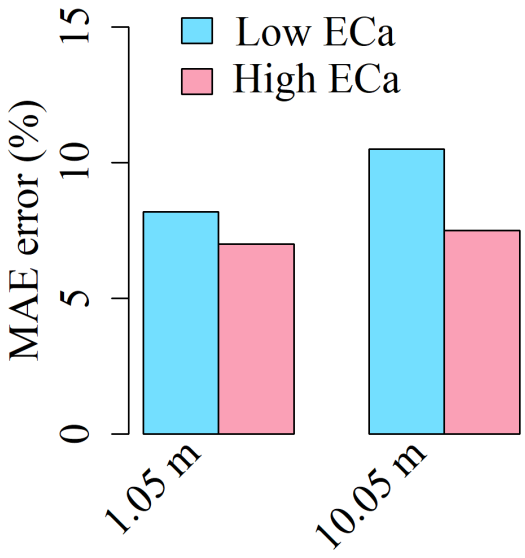

Fig. 3.7 MAPE values of TSEB UAV LE estimates at various pixel sizes. Different colors represent the high EC_a and low EC_a zones (Fig. 3.1b). Values were obtained by averaging TSEB-PT, TSEB-DTD, and TSEB-2T model results within each EC_a zone (Table 3.5).

Table 3.8 p-values from ANOVA models testing the significance of EC_a information, and thus soil type, in predicting LE. ANOVA models were applied across different models and pixel resolutions.

Model	Resolution (m)	p-value
PT	1.05	< 0.01
	10.05	< 0.01
DTD	1.05	< 0.01
	10.05	< 0.01
2T	1.05	0.02
	10.05	0.02
DATTUTDUT - with inputs	1.05	< 0.01
	10.05	0.01
DATTUTDUT - without inputs	1.05	< 0.01
	10.05	0.01

In addition to model comparisons relative to eddy flux towers (Fig. 3.6-3.7), soil variability was also examined by comparison of spatial patterns in UAV LE fluxes across the entire field. Fig. 3.8 shows LE frequency histograms at 1.05 m, both within the low EC_a zone (first row) and the high EC_a zone (second row), at the beginning and ending dates of vegetation growth (June 16 and July 26, respectively). The median values (i.e. vertical lines) presented in Fig. 3.8 are given in Table 3.9 for further discussion. Results are first provided for June 16 or partial vegetation cover. Across both EC_a zones, the median LE of DATTUTDUT with inputs (black lines, Fig. 3.8) was greater than DATTUTDUT without inputs (red lines, Fig. 3.8) (Table 3.9). On June 16, the DATTUTDUT distributions within the low EC_a zone and the high EC_a zone both have a lower median (186-288 W m^{-2}) relative to the TSEB models (around 350-404 W m^{-2}) (Table 3.9). On June 16, TSEB model distributions were pretty similar to each other across both EC_a zones, although the average median values were greater within low EC_a than high EC_a (347 vs. 298 W m^{-2}, respectively, Table 3.9).

On July 26 (Fig. 3.8b, 3.8d), differences between DATTUTDUT and TSEB spatial patterns decreased across both EC_a zones (Fig. 3.8b, 3.8d). Unlike June 16, the median values of TSEB models were greater within high EC_a than low EC_a zones (651 vs. 568 W m^{-2}, respectively, Table 3.9). These trends appear to match those at the eddy flux towers (Fig. 3.6) – in other words, LE at the low EC_a site was initially greater than the high EC_a site on June 16, but these trends were reversed on July 26 (Fig. 3.6). These trends are also similar to those observed with the LAI data over time (Fig. 3.3), suggesting likely soil moisture and vegetation interactions. These results collectively

indicate that soil type or variability result in different LE spatial patterns values with respect to DATTUTDUT and TSEB models.

Table 3.9 Median LE values from the entire field histograms plotted in Fig. 3.8.

Date	Soil Type	Model	Median LE (W m^{-2})
June 16, 2017	Low EC_a	TSEB-PT	399
		TSEB-2T	390
		TSEB-DTD	404
		DATTUTDUT-All Inputs	288
		DATTUTDUT-No Inputs	253
	High EC_a	TSEB-PT	350
		TSEB-2T	378
		TSEB-DTD	363
		DATTUTDUT-All Inputs	213
		DATTUTDUT-No Inputs	186
July 26, 2017	Low EC_a	TSEB-PT	630
		TSEB-2T	578
		TSEB-DTD	575
		DATTUTDUT-All Inputs	553
		DATTUTDUT-No Inputs	504
	High EC_a	TSEB-PT	696
		TSEB-2T	684
		TSEB-DTD	620
		DATTUTDUT-All Inputs	657
		DATTUTDUT-No Inputs	600

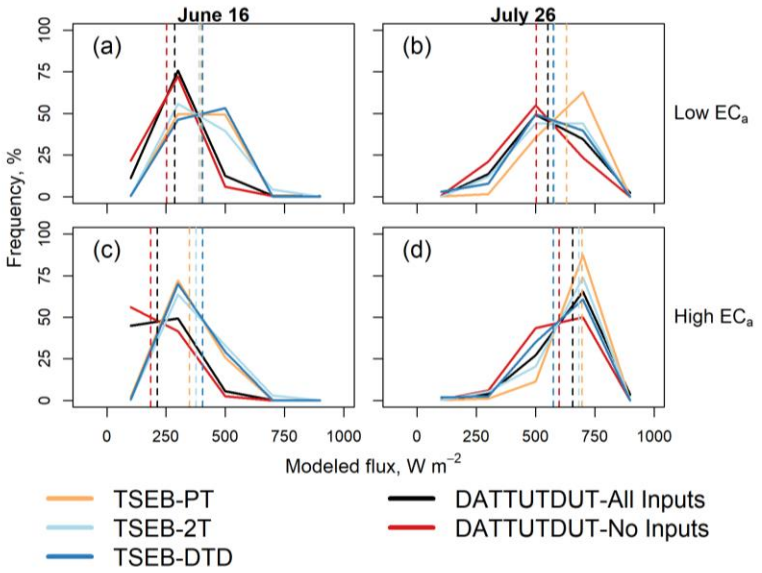

Fig. 3.8 Full field model output at 1.05 m for TSEB-PT (orange), TSEB-2T (light blue), TSEB-DTD (dark blue), DATTUTDUT with inputs (black), and DATTUTDUT without inputs (red). (a) and (b) refer to the low EC_a area on June 16 and July 26, respectively, while (c) and (d) refer to the high EC_a area on June 16 and July 26, respectively. Vertical bars represent the median values obtained from each date-model-EC_a zone combination. Values are expressed in terms of percent frequency within a given EC_a zone.

3.3.4. Behavior of DATTUTDUT

The mechanics of the DATTUDUT model were explored further to address why it did not estimate LE as well as TSEB (Table 3.6). DATTUTDUT model results appear to be affected by pixel resolution (Table 3.6), and Fig. 3.9 reinforces this idea. Fig. 3.9 shows that the bias and accuracy increases and decreases with pixel resolution, respectively. The observation that DATTUTDUT results vary as a function of pixel resolution has been previously reported by Brenner et al. (2018) and Xia et al. (2016). At 1.05 m, adding weather inputs decreased the absolute bias from 12-7 %. While the nature of this bias is not entirely addressed in this paper, Timmermans et al. (2015)

suggest that DATTUTDUT underestimates of LE can be caused by underestimation of R_n (based on T_a, ε_a and SW_{in}). While DATTUTDUT without weather inputs was slightly more accurate than DATTUTDUT with weather inputs, it was more negatively biased across all pixel resolutions. These results suggest that adding local weather information to DATTUTDUT modelling schemes may not entirely be necessary, especially if one is only interested in LE spatial patterns alone (and not magnitudes, Xia et al., 2016).

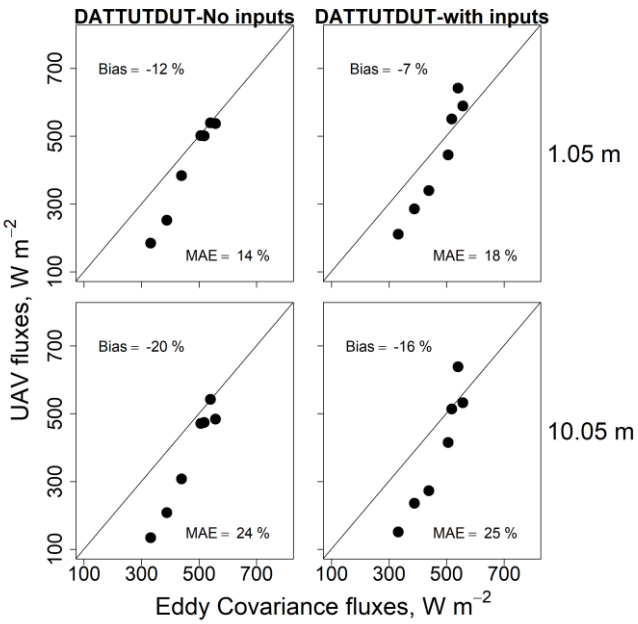

Fig. 3.9 UAV predicted fluxes using DATTUTDUT either with or without ancillary inputs at 1.05 m, and 10.05 m resolutions. Similar to Fig. 3.7, each point represents LE fluxes modelled from both EC_a towers.

Image aggregation likely affected DATTUTDUT modelling results (Fig. 3.9) in terms of the hot and cold temperature endmembers (Eq. 3.18b). Fig. 3.10 shows the

locations of these cold (i.e. $T_{r,min}$) and hot (i.e. $T_{r,max}$) pixels from various DATTUTDUT model runs (with inputs) laid over IOP-specific T_r imagery. Hot pixels ($T_{r,max}$ light blue) were generally associated with bare soil, located within poorly vegetated areas (Fig. 3.10a) or from exposed soil via the irrigation wheel tracks (Fig. 3.10b-3.10.d). On June 16, cold objects ($T_{r,min}$, dark blue) were located under bare soil in the high EC_a zone (Fig. 3.10a). On July 1, cold pixels were located at various edges of the field – within these particular regions, dense vegetation was observed from inspection of multispectral imagery (Fig. 3.10b). On July 18 and July 26, the locations of these cold pixels generally shift from the field edges into various densely vegetated areas within the field.

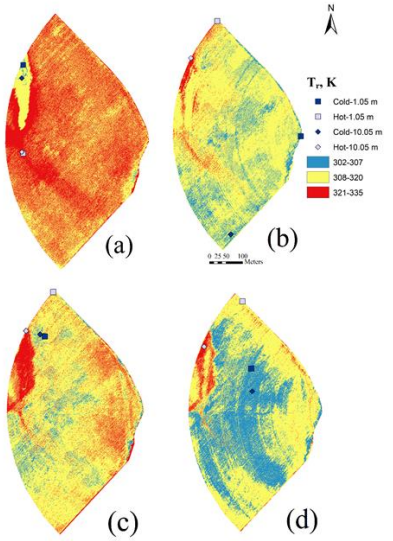

Fig. 3.10 UAV 1.05 m orthomosaics of T_r on the following dates: (a) June 16, (b) July 1, (c) July 18, (d) July 26. Also plotted are the locations of cold (i.e. $T_{r,min}$, dark blue) and hot (i.e. $T_{r,max}$, light blue) pixels on their respective dates at 1.05 m (squares) and 10.05 m (diamonds).

In addition to time, the locations of these cold and hot endmembers shifted by pixel resolution. This can be observed with cold pixels, for example, on July 1, as endmembers shift to different regions associated with high canopy cover (Fig. 3.11b, dark blue diamond and square). Except for June 16, $T_{r,max}$ pixels similarly shifted to different areas associated with patches of bare soil. The reason for this may be explained as follows - if endmembers have features with sharply contrasting temperatures, image aggregation will result in endmembers that are likely a mixture of hot and cold temperatures. This probably explains why endmembers shifted, for example, from field edges, as objects of contrasting temperatures were present near each other at 1.05 m (e.g. bare soil, cotton plants). The spatial distribution of cold endmembers appears to be relatively more stable than hot endmembers, and the latter are located within patchy vegetated areas, especially on June 16 (Fig. 3.10a). Therefore, T_{max} and T_{min} selection are likely affected by the degree of local homogeneity within the T_r imagery.

Because many of the $T_{r,max}$ endmembers were located within the high EC_a zone, it was hypothesized that DATTUTUT model output would be affected by soil type or T_{max}. Therefore, a simple sensitivity analysis was conducted to test the effects of $T_{r,max}$ on the LE scaling parameter (i.e. $\frac{T_{r,max}-T_r}{T_{r,max}-T_{r,min}}$, Eq. 3.18b) across various T_c values (Fig. 3.11). Fig. 3.11 plots the scaling parameter as a function of various $T_{r,max}$ representative of soils (310-340 K) and various T_r values representative of cotton canopies (300-310 K) (Wanjura et al., 2004). When T_r = 300 K, $\frac{T_{r,max}-T_r}{T_{r,max}-T_{r,min}}$ stays constant at one because T_r = $T_{r,min}$ (Fig. 3.11). With increasing T_r, however, $\frac{T_{r,max}-T_r}{T_{r,max}-T_{r,min}}$ changes, showing larger

sensitivity as T_r increases and as $T_{r,max}$ decreases. This simple analysis suggests that DATTUTDUT is less sensitive towards modelling LE when T_{max} values are relatively high. This finding has implications especially within the context of soil variability - lighter soils (or relatively low $T_{r,max}$) may show greater sensitivity to model output than darker colored soils (or higher $T_{r,max}$), depending upon canopy T_r. Future studies may want to keep this point in mind when interpreting DATTUTUDUT output where soil variability exists within a single production field, as it will likely determine T_{max} and, therefore, EF and L (Eq. 3.18).

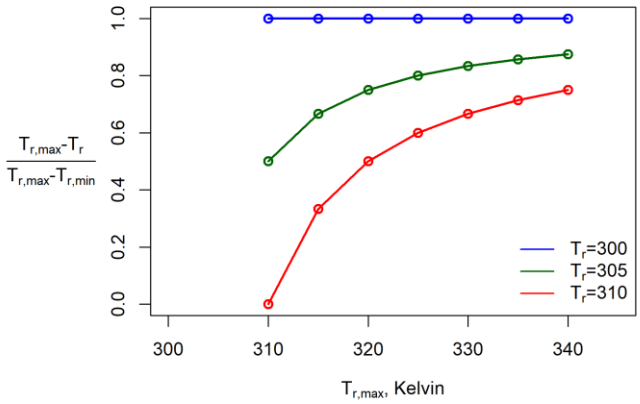

Fig. 3.11 Sensitivity analysis of the DATTUTDUT LE scaling factor (i.e. $\frac{T_{r,max}-T_r}{T_{r,max}-T_{r,min}}$, Eq. 3.18b) to changes in the $T_{r,max}$ endmember as well as typical T_0 values measured from crop canopies.

3.4. Conclusions

In this study, flux components from the energy balance equation were modelled using multispectral and thermal imagery collected from a UAV throughout a single

cotton growing season. The energy balance models evaluated included various non-contextual (TSEB) and contextual (DATTUTDUT) models. These models were applied at various aggregated pixel resolutions (1.05 m and 10.05 m) and evaluated against eddy covariance data across two soil types using apparent electrical conductivity data. Non-contextual (i.e. TSEB) models were more accurate in estimating all energy balance components relative to contextual models (i.e. DATTUTDUT). At 1.05 m, TSEB models behaved similarly in estimating LE relative to eddy flux towers. At 10.05 m, however, TSEB-PT and TSEB-DTD were the most accurate models, with the latter producing lower biases presumably due to reduction of T_r biases. TSEB-PT models overestimated LE the most within the TSEB suite, and this could be due to violated assumptions of full water availability throughout the season. When local weather data was added to DATTUTDUT, the bias in LE estimates was reduced. However, the accuracies were similar, if not worse, than when DATTTUDUT models were run with only thermal information. Finally, DATTUTDUT model performance degraded with coarsening pixel resolutions. It is hypothesized that these results occurred because the range in temperature endmembers, and thus sensitivity, decreased with coarsening pixel resolutions.

With respect to soil type, LE model performance within the high clay content soil (~ 30 %) was slightly better than that from the higher clay content soil (~ 47%), both at 1.05 and 10.05 m. A comparison of spatial LE patterns across the entire field showed that low and high EC_a zones behaved differently with respect to the individual energy balance models. These results were consistent both at cotton flowering and boll

production. Across both soil EC_a zones, DATTUTDUT LE fluxes were most dissimilar with TSEB during cotton flowering.

A discussion on the performance of TSEB relative to DATTUTDUT is in order. Model results for LE were generally more accurate when using TSEB (i.e. TSEB-PT, TSEB-DTD, TSEB-2T) than DATTUTDUT models. Previous UAV-based SEB studies have confirmed these findings (Xia et al., 2016). TSEB-DTD models, in contrast, performed the best, especially on the operational scale (10.05 m). Kelly et al. (2019) provide recommendations for main sources of error in TIR cameras such as radiometric calibration, the influence of sensor temperature, non-uniformity noise, target ε and distance from target. Correction of absolute temperature can be particularly challenging. Furthermore, the sources discussed by Kelly et al. (2019) often conflict with one another. For example, there is a trade-off between flying slowly (i.e. to minimize image blurring) while minimizing temperature drift and limiting cloud variability, and such tradeoffs are affected by the field size. Within this context, therefore, TSEB-DTD models show favor from an accuracy standpoint because absolute T_r measurements are not needed. It is hypothesized that TSEB-PT and TSEB-2T results could be improved by refining the method for deriving absolute T_r measurements. One example of such an improvement could be made by considering an ambient temperature blackbody before each flight, as well the use of rigorous atmospheric models (e.g. MODTRAN) (Torres-Rua et al., 2017). However, these approaches are relatively new and have not been addressed beyond that study. Furthermore, these tools were not available for this study due to limited resources.

While UAV survey quality affects both DATTUTDUT and TSEB models, TSEB present additional challenges in terms of needed inputs, especially if they are image-based. NDVI, in particular, requires considerable effort in terms of equipment costs and the manpower needed towards radiometric calibration. Furthermore, TSEB-DTD models require the design and implementation of UAV surveys both in the morning and in the afternoon. Within this study, therefore, three different surveys were needed for TSEB-DTD models, two with the thermal camera and one with the multispectral camera. The number of flights needed in this scenario provides more financial resources and logistics than say with DATTUTDUT, whereby only one flight would be needed. There are only two main operational challenges for DATTUTDUT modelling: 1) to generate a positionally accurate and seamless orthomosaic, and 2) an approach to convert T_{br} into T_r. If spatial patterns alone are required, DATTUTDUT may serve as a viable alternative to TSEB, although the results here suggest that it may not be the most accurate model.

It is recommended that future studies explore intercomparisons between TSEB and DATTUTDUT further for cotton, particularly within other climatic regions presented here. These studies should provide UAV imagery at spatial and temporal resolutions required by users. For example, a recent survey found that that about 40 % of users of ET maps prefer spatial resolutions between 1-10 m, while 60 % prefer ET maps greater than 10 meters (Nieto et al., 2018b). Additionally, about 45 % of users would request daily ET maps, while 55 % would request hourly, monthly or weekly ET maps. In addition to user requirements, the performance of DATTUTDUT within different environments, particularly arid landscapes, warrants further examination. Allen et al.

(2007) suggest that contextual models that estimate LE using the EF fraction can behave poorly in these areas, primarily when instantaneous fluxes are upscaled to daily fluxes. Furthermore, future DATTUTDUT development needs to incorporate estimates of LE_c instead of LE, assuming pixel resolutions are fine enough to capture such information. This approach was not adopted here because validation tools for soil evaporation (e.g. micro-lysimeters) and plant transpiration (e.g. sap flow sensors) were not available (Kool et al. 2014). Based on a recent user survey report (Nieto et al., 2018a), future models should aim to achieve an ET uncertainty no worse than 10 W m^{-2} or 0.35 mm day^{-1}. Thus, from a modelling perspective it is important to perform model intercomparisons to fully quantify the uncertainty associated with ET estimations.

3.5. References

Aboutalebi, M., Torres-Rua, A. F., Kustas, W. P., Nieto, H., Coopmans, C., & McKee, M. (2019). Assessment of different methods for shadow detection in high-resolution optical imagery and evaluation of shadow impact on calculation of NDVI, and evapotranspiration. *Irrigation Science*, *37*(3), 407–429.

Alfieri, J. G., Blanken, P. D., Yates, D. N., & Steffen, K. (2007). Variability in the environmental factors driving evapotranspiration from a grazed rangeland during severe drought conditions. *Journal of Hydrometeorology*, *8*(2), 207–220.

Allen, R. G., Tasumi, M., & Trezza, R. (2007). Satellite-based energy balance for mapping evapotranspiration with internalized calibration (METRIC) - model. *Journal of Irrigation and Drainage Engineering*, *133*(4), 380–394.

Alvino, A., & Marino, S. (2017). Remote sensing for irrigation of horticultural crops. *Horticulturae*, *3*(2), 40.

Anderson, M. C., Norman, J. M., Diak, G. R., Kustas, W. P., & Mecikalski, J. R. (1997). A two-source time-integrated model for estimating surface fluxes using thermal infrared remote sensing. *Remote Sensing of Environment*, *60*(2), 195–216.

Berni, J. A. J., Zarco-Tejada, P. J., Suarez, L., & Fereres, E. (2009). Thermal and narrowband multispectral remote sensing for vegetation monitoring from an

unmanned aerial vehicle. *IEEE Transactions on Geoscience and Remote Sensing*, *47*(3), 722–738.

Brenner, C., Thiem, C. E., Wizemann, H. D., Bernhardt, M., & Schulz, K. (2017). Estimating spatially distributed turbulent heat fluxes from high-resolution thermal imagery acquired with a UAV system. *International Journal of Remote Sensing*, *38*, 1–24.

Brenner, C., Zeeman, M., Bernhardt, M., & Schulz, K. (2018). Estimation of evapotranspiration of temperate grassland based on high-resolution thermal and visible range imagery from unmanned aerial systems. *International Journal of Remote Sensing*, *39*(15–16), 5141–5174. doi:10.1080/01431161.2018.1471550

Brutsaert, W. (1982). *Evaporation into the atmosphere: theory, history and applications*. Springer Science+Business Media Dordrecht.

Burba, G., & Anderson, D. (2010). *A Brief practical guide to eddy covariance flux measurements: principles and workflow examples for scientific and industrial applications*. Lincoln, NE, USA: LI-COR Biosciences.

Calera, A., Campos, I., Osann, A., D'Urso, G., & Menenti, M. (2017). Remote sensing for crop water management: From ET modelling to services for the end users. *Sensors*, *17*(5), 1104.

Campbell, G. S., & Campbell, M. D. (1982). Irrigation scheduling using soil moisture measurements: theory and practice. In D. Hillel (Ed.), *Advances in Irrigation*. New York, USA: Academic Press.

Campbell, G. S., & Norman, J. M. (1998). *An Introduction to environmental biophysics* (2nd ed.). New York, USA: Springer Science+Business Media B.V.

Carlson, T. N., & Ripley, D. A. (1997). On the relation between NDVI, fractional vegetation cover, and leaf area index. *Remote Sensing of Environment*, *62*(3), 241–252.

Chávez, J., Neale, C. M. U., Hipps, L. E., Prueger, J. H., & Kustas, W. P. (2005). Comparing aircraft-based remotely sensed energy balance fluxes with eddy covariance tower data using heat flux source area functions. *Journal of Hydrometeorology*, *6*(6), 923–940.

Chehbouni, A., Lo Seen, D., Njoku, E. G., & Monteny, B. M. (1996). Examination of the difference between radiative and aerodynamic surface temperatures over sparsely vegetated surfaces. *Remote Sensing of Environment*, *58*(2), 177–186.

Choi, M., Kustas, W. P., Anderson, M. C., Allen, R. G., Li, F., & Kjaersgaard, J. H. (2009). An intercomparison of three remote sensing-based surface energy balance algorithms over a corn and soybean production region (Iowa, U.S.) during SMACEX. *Agricultural and Forest Meteorology*, *149*(12), 2082–2097.

Courault, D., Seguin, B., & Olioso, A. (2005). Review on estimation of evapotranspiration from remote sensing data: From empirical to numerical modeling approaches. *Irrigation and Drainage Systems*, *19*, 223–249.

Detto, M., Montaldo, N., Albertson, J. D., Mancini, M., & Katul, G. (2006). Soil moisture and vegetation controls on evapotranspiration in a heterogeneous Mediterranean ecosystem on Sardinia, Italy. *Water Resources Research*, *42*(8), 1–16.

Evans, R. G., & Sadler, E. J. (2008). Methods and technologies to improve efficiency of water use. *Water Resources Research*, *44*(7), W00E04.

Evett, S. R., Agam, N., Kustas, W. P., Colaizzi, P. D., & Schwartz, R. C. (2012). Soil profile method for soil thermal diffusivity, conductivity and heat flux: comparison to soil heat flux plates. *Advances in Water Resources*, *50*, 41–54.

Farquhar, G. D., & Sharkey, T. D. (1982). Stomatal conductance and photosynthesis. *Annual Review of Plant Physiology*, *33*(1), 317–345.

Fisher, J. B., Melton, F., Middleton, E., Hain, C., Anderson, M., Allen, R., et al. (2017). The future of evapotranspiration: Global requirements for ecosystem functioning, carbon and climate feedbacks, agricultural management, and water resources. *Water Resources Research*, *53*, 2618–2626.

Foken, T. (2008). The energy balance closure problem: an overview. *Ecological Applications*, *18*(6), 1351–1367.

Frank, J. M., Massman, W. J., & Ewers, B. E. (2013). Underestimates of sensible heat flux due to vertical velocity measurement errors in non-orthogonal sonic anemometers. *Agricultural and Forest Meteorology*, *171–172*, 72–81.

Fuchs, M., & Tanner, C. B. (1966). Infrared thermometry of vegetation. *Agronomy Journal*, *58*, 597–601.

Gentine, P., Troy, T. J., Lintner, B. R., & Findell, K. L. (2012). Scaling in Surface Hydrology: Progress and Challenges. *Journal of Contemporary Water Research & Education*, *147*(1), 28–40.

Gevaert, A. I., Miralles, D. G., de Jeu, R. A. M., Schellekens, J., & Dolman, A. J. (2018). Soil moisture-temperature coupling in a set of land surface models. *Journal of Geophysical Research: Atmospheres*, *123*(3), 1481–1498.

Guzinski, R., & Nieto, H. (2019). Evaluating the feasibility of using Sentinel-2 and Sentinel-3 satellites for high-resolution evapotranspiration estimations. *Remote Sensing of Environment*, *221*, 157–172.

Han, X., Thomasson, J. A., Bagnall, G. C., Pugh, N. A., Horne, D. W., Rooney, W. L., et al. (2018). Measurement and calibration of plant-height from fixed-wing UAV images. *Sensors*, *18*, 4092.

Hatfield, J. L., & Prueger, J. H. (2011). Spatial and temporal variation in evapotranspiration. In G. A. Gerosa (Ed.), *Evapotranspiration from measurements to agricultural and environmental applications* (pp. 3–16). London: InTech.

Hoffmann, H., Nieto, H., Jensen, R., Guzinski, R., Zarco-Tejada, P., & Friborg, T. (2016). Estimating evaporation with thermal UAV data and two-source energy balance models. *Hydrology and Earth System Sciences*, *20*, 697–713.

Hsieh, C. I., Katul, G., & Chi, T. W. (2000). An approximate analytical model for footprint estimation of scalar fluxes in thermally stratified atmospheric flows. *Advances in Water Resources*, *23*(7), 765–772.

Iqbal, F., Lucieer, A., & Barry, K. (2018). Simplified radiometric calibration for UAS-mounted multispectral sensor. *European Journal of Remote Sensing*, *51*(1), 301–313.

Jensen, M. E., Robb, D. C. N., & Franzoy, C. E. (1969). Scheduling irrigations using climate-crop data. *Journal of the Irrigation and Drainage Division. Division of the American Society of Civil Engineers*(IR1), *96*, 25–38.

Jiménez-Muñoz, J. C., Sobrino, J. A., Gillespie, A., Sabol, D., & Gustafson, W. T. (2006). Improved land surface emissivities over agricultural areas using ASTER NDVI. *Remote Sensing of Environment*, *103*(4), 474–487.

Jones, H. G. (2004). Irrigation scheduling: advantages and pitfalls of plant-based methods. *Journal of Experimental Botany*, *55*(407), 2427–2436.

Jones, H. G. (2007). Monitoring plant and soil water status: established and novel methods revisited and their relevance to studies of drought tolerance. *Journal of Experimental Botany*, *58*(2), 119–130.

Kelly, J., Kljun, N., Olsson, P.-O., Mihai, L., Liljeblad, B., Weslien, P., et al. (2019). Challenges and best practices for deriving temperature data from an uncalibrated UAV thermal infrared camera. *Remote Sensing*, *11*(5), 567.

Kochendorfer, J., Meyers, T. P., Frank, J., Massman, W. J., & Heuer, M. W. (2012). How well can we measure the vertical wind speed? Implications for fluxes of energy and mass. *Boundary-Layer Meteorology*, *145*(2), 383–398.

Kool, D., Agam, N., Lazarovitch, N., Heitman, J. L., Sauer, T. J., & Ben-Gal, A. (2014). A review of approaches for evapotranspiration partitioning. *Agricultural and Forest Meteorology*, *184*, 56–70.

Kustas, W. P., & Norman, J. M. (1999). Evaluation of soil and vegetation heat flux predictions using a simple two-source model with radiometric temperatures for partial canopy cover. *Agricultural and Forest Meteorology*, *94*(1), 13–29.

Kustas, W. P., & Daughtry, C. S. T. (1990). Estimation of the soil heat flux/net radiation ratio from spectral data. *Agricultural and Forest Meteorology*, *49*, 205–223.

Kustas, W. P., Li, F., Jackson, T. J., Prueger, J. H., MacPherson, J. I., & Wolde, M. (2004). Effects of remote sensing pixel resolution on modeled energy flux variability of croplands in Iowa. *Remote Sensing of Environment*, *92*(4), 535–547.

Kustas, W. P., Anderson, M. C., Alfieri, J. G., Knipppper, K., Torres-Rua, A., Parry, C. K., et al. (2018). The Grape Remote sensing Atmospheric Profile and Evapotranspiration EXperiment. *Bulletin of the American Meteorological Society*, *99*(9), 1791–1812.

Li, F., Kustas, W. P., Anderson, M. C., Prueger, J. H., & Scott, R. L. (2008). Effect of remote sensing spatial resolution on interpreting tower-based flux observations. *Remote Sensing of Environment*, *112*, 337–349.

Liou, Y. A., & Kar, S. K. (2014). Evapotranspiration estimation with remote sensing and various surface energy balance algorithms-a review. *Energies*, *7*(5), 2821–2849.

Maas, S. J., & Rajan, N. (2008). Estimating ground cover of field crops using medium-resolution multispectral satellite imagery. *Agronomy Journal*, *100*(2), 320–327.

Maes, W. H., & Steppe, K. (2012). Estimating evapotranspiration and drought stress with ground-based thermal remote sensing in agriculture: a review. *Journal of Experimental Botany*, *63*(13), 4671–4712.

Meyers, T. P., & Hollinger, S. E. (2004). An assessment of storage terms in the surface energy balance of maize and soybean. *Agricultural and Forest Meteorology*, *125*(1–2), 105–115.

Mohtar, R. H., & Daher, B. (2016). Water-Energy-Food nexus framework for facilitating multi-stakeholder dialogue. *Water International*, *41*(5), 655–661.

Monin, A. S., & Obukhov, A. M. (1954). Basic laws of turbulent mixing in the surface layer of the atmosphere. *Tr. Akad. Nauk SSSR Geophiz. Inst.*, *24*, 163–187.

Neale, C. M. U., Geli, H. M. E., Kustas, W. P., Alfieri, J. G., Gowda, P. H., Evett, S. R., et al. (2012). Soil water content estimation using a remote sensing based hybrid evapotranspiration modeling approach. *Advances in Water Resources*, *50*, 152–161.

Nieto, H., Bellvert, J., Kustas, W. P., Alfieri, J. G., Gao, F., Prueger, J., & Hipps, L. E. (2017). Unmanned airborne thermal and multispectral imagery for estimating evapotranspiration in irrigated vineyards. In *Geoscience and Remote Sensing Symposium* (pp. 5510–5513). Fort Worth, TX: Institute of Electrical and Electronics Engineers.

Nieto, H., Kustas, W. P., Torres-Rúa, A., Alfieri, J. G., Gao, F., Anderson, M. C., et al. (2018a). Evaluation of TSEB turbulent fluxes using different methods for the retrieval of soil and canopy component temperatures from UAV thermal and multispectral imagery. *Irrigation Science*, 1–18.

Nieto, H., Sandholt, I., Rasmussen, M. O., Guzinski, R., Bellvert, J., Hansen, L. H., et al. (2018b). *Review of remote sensing evapotranspiration models*.

Nieto, H., Guzinski, R., Kustas, W. P., & Andreau, A. (2019). A python Two Source Energy Balance model for estimation of evapotranspiration with remote sensing data.

Norman, J. M., Kustas, W. P., Prueger, J. H., & Diak, G. R. (2000). Surface flux estimation using radiometric temperature: A dual-temperature-difference method to minimize measurement errors. *Water Resources Research*, *36*(8), 2263–2274.

Norman, J. M., Kustas, W. P., & Humes, K. S. (1995). A two-source approach for estimating soil and vegetation energy fluxes from observations of directional radiometric surface temperature. *Agricultural and Forest Meteorology*, *77*, 263–293.

Norman, J. M., & Becker, F. (1995). Terminology in thermal infrared remote sensing of natural surfaces. *Agricultural and Forest Meteorology*, *77*, 153–166.

Ortega-Farías, S., Ortega-Salazar, S., Poblete, T., Kilic, A., Allen, R., Poblete-Echeverría, C., et al. (2016). Estimation of energy balance components over a drip-irrigated olive orchard using thermal and multispectral cameras placed on a helicopter-based unmanned aerial vehicle (UAV). *Remote Sensing*, *8*(638), 1–18.

Penman, H. L. (1952). The physical bases of irrigation control. *International Horticultural Congress*, *2*, 913–924.

Priestley, C. H. B., & Taylor, R. J. (1972). On the assessment of surface heat flux and evaporation using large-scale parameters. *Weather Review*, *100*(2), 81–92.

Pritsolas, J., Pearson, R., Connor, J., & Kyveryga, P. (2016). Challenges and successes when generating in-season multi-temporal calibrated aerial imagery. In *Proceedings of the 13th International Conference on Precision Agriculture* (pp. 1–15).

R Core Development Team (2018). R: A Language and Environment for Statistical Computing. Vienna, Austria.

Rajan, N., Maas, S. J., & Kathilankal, J. C. (2010). Estimating crop water use of cotton in the Texas High Plains. *Agronomy Journal*, *102*(6), 1641–1651.

Rouse, J. W., Haas, R. H., Schell, J. A., & Deering, D. W. (1973). Monitoring vegetation systems in the Great Plains with ERTS. NASA SP-351 I. In *Third ERTS Symposium* (pp. 309–317).

Rouze, G., Neely, H. L., & Morgan, C. L. (in preparation). Evaluating Unmanned Aerial Vehicle (UAV) Imagery as an Alternative Tool Towards Cotton Site-Specific Management.

Schmid, H. P. (1994). Source areas for scalars and scalar fluxes. *Boundary-Layer Meteorology*, *67*, 293–318.

Sharma, S., Rajan, N., Cui, S., Maas, S., Casey, K., Ale, S., & Jessup, R. (2019). Carbon and evapotranspiration dynamics of a non-native perennial grass with biofuel potential in the southern U.S. Great Plains. *Agricultural and Forest Meteorology*, *269–270*, 285–293.

Shi, Y., Thomasson, J. A., Murray, S. C., Pugh, N. A., Rooney, W. L., Shafian, S., et al. (2016). Unmanned aerial vehicles for high-throughput phenotyping and agronomic research. *PloS one*, *11*(7), e0159781.

Smith, G. M., & Milton, E. J. (1999). The use of the empirical line method to calibrate remotely sensed data to reflectance. *International Journal of Remote Sensing*, *20*(13), 2653–2662.

Smith, R. J., Raine, S. R., Mccarthy, A. C., & Hancock, N. H. (2009). Managing spatial and temporal variability in irrigated agriculture through adaptive control. *Australian Journal of Multi-disciplinary Engineering*, *7*(1), 79–90.

Sridhar, V., Elliott, R. L., & Chen, F. (2003). Scaling effects on modeled surface energy-balance components using the NOAH-OSU land surface model. *Journal of Hydrology*, *280*(1–4), 105–123.

Stanislav, S. (2010). *A field-scale assessment of soil-specific seeding rates to optimize yield factors and water use in cotton. Masters Thesis.* Texas A&M University.

Timmermans, W. J., Kustas, W. P., & Andreu, A. (2015). Utility of an automated thermal-based approach for monitoring evapotranspiration. *Acta Geophysica*, *63*(6), 1571–1608.

Torres-Rua, A. (2017). Vicarious calibration of sUAS microbolometer temperature imagery for estimation of radiometric land surface temperature. *Sensors*, *17*(7), 1499.

Vanham, D. (2016). Does the water footprint concept provide relevant information to address the water-food-energy-ecosystem nexus? *Ecosystem Services*, *17*, 298–307.

Verstraeten, W. W., Veroustraete, F., & Feyen, J. (2008). Assessment of evapotranspiration and soil moisture content across different scales of observation. *Sensors*, *8*, 70–117.

Wang, W. M., Li, Z. L., & Su, H. B. (2007). Comparison of leaf angle distribution functions: effects on extinction coefficient and fraction of sunlit foliage. *Agricultural and Forest Meteorology*, *143*(1–2), 106–122.

Wanjura, D. F., Maas, S. J., Winslow, J. C., & Upchurch, D. R. (2004). Scanned and spot measured canopy temperatures of cotton and corn. *Computers and Electronics in Agriculture*, *44*(1), 33–48.

Westoby, M. J., Brasington, J., Glasser, N. F., Hambrey, M. J., & Reynolds, J. M. (2012). "Structure-from-Motion" photogrammetry: A low-cost, effective tool for geoscience applications. *Geomorphology*, *179*, 300–314.

Xia, T., Kustas, W. P., Anderson, M. C., Alfieri, J. G., Gao, F., McKee, L., et al. (2016). Mapping evapotranspiration with high-resolution aircraft imagery over vineyards using one-and two-source modeling schemes. *Hydrology and Earth System Sciences*, *20*(4), 1523–1545.

Zotarelli, L., Scholberg, J. M., Dukes, M. D., Muñoz-Carpena, R., & Icerman, J. (2009). Tomato yield, biomass accumulation, root distribution and irrigation water use efficiency on a sandy soil, as affected by nitrogen rate and irrigation scheduling. *Agricultural Water Management*, *96*(1), 23–34.

4. EVALUATING UP-SCALING TECHNIQUES OF UAV-BASED COTTON LATENT HEAT FLUX MAPS WITHIN AN IRRIGATED PRODUCTION FIELD

4.1. Introduction

Global populations are expected to rise by 2.4 billion people by the year 2050 (United Nations Department of Economic and Social Affairs Population Division, 2015). Therefore, the demand for food resources is only set to increase for future generations. This existential challenge has been partially alleviated with irrigated agriculture (Carruthers et al., 1997; Ozdogan et al., 2010). However, water use is not strictly limited to agriculture, as competition exists between other sectors (e.g. oil/gas) across spatial (and sometimes political) scales (e.g. field, farm, state, national etc.) (Strzepek and Boehlert, 2010; Flörke et al., 2018). In order for farmers to secure their claim on pre-existing water resources, irrigation management will need to produce 'more crop per drop' for future food production (Morison et al., 2008).

One way to optimize irrigation practices is to monitor crop water status via plant physiological responses (Jones, 2004). Plants that experience extreme drought stress, for example, will keep their stomata closed to prevent water loss, resulting in reduced transpiration rates and increased leaf temperatures (Jarvis, 1976). Irrigation management is also affected by soil evaporation, which occurs into atmosphere controlled and soil moisture controlled stages (Brutsaert, 2014). These insights have towards the use of thermal infrared data to estimate evapotranspiration (ET, in mm per unit time) or, the energy equivalent term latent energy flux (LE, in W m^{-2}) (Jackson, 1977). ET and LE

refer to water vapor transferred to the atmosphere, by surface evaporation and/or plant transpiration (Verstraeten et al., 2008). Because of these processes described above, ET plays a primary role in linking ecosystem functioning, as well as carbon/hydrologic cycle feedbacks (Fisher et al., 2017).

ET has been estimated using thermal and multispectral imagery located from sensors located aboard non-commercial geostationary and polar-orbiting satellites (or SATs) (Courault et al., 2005). SAT remote sensing, unlike other previous point methods (e.g. eddy covariance), can characterize ET across multiple spatial scales (Verstraeten et al., 2008). While SAT-based ET estimates have proven useful towards irrigation applications focused on the long-term (e.g. water rights negotiations, Allen et al., 2005), there are mixed perspectives regarding their utility towards applications on the short term, such as in-season crop monitoring. Knipper et al. (2019), for example, demonstrated that daily SAT ET estimates at 30 m can be very useful in many operational water management applications. From a practical perspective, however, SAT LE retrievals are problematic because images are collected only twice a month (at best) and even then are not guaranteed to be cloud-free (Hunt and Daughtry, 2018). Furthermore, even ET at the highest SAT pixel resolution (currently 30 m) may not be sufficient to detect crop and soil variability within a single production field. New studies by Vanino et al. (2018) and Guzinksi and Nieto (2019) suggest that 5-day ET maps at 10-meter pixel resolution maybe possible with Sentinel SATs, but its imagery has not been collected long enough to test this hypothesis. While alternative platforms such as commercial SATs and manned aerial vehicles (MAVs) can provide enhanced spatial and

temporal information within a single production field, both can have high acquisition costs, as companies require a minimum area for coverage in order to at least break-even (Matese et al., 2015).

Unmanned aerial vehicles (UAVs) have been proposed as an alternative to monitor ET, and thus improve irrigation efficiencies, within a given production field (Hoffmann et al., 2016). This is because, relative to MAVs and commercial/non-commercial SATs, users have the most control over image collection (Matese et al., 2015). UAV flights are even expected to become even cheaper soon and fly longer with continual improvements in sensors and UAV platforms (Manfreda et al., 2018). UAVs can offer additional advantages in terms of spatial detail, with imagery as fine as 0.05 m (pixel area = 0.0025 m^2) having been reported (Brenner et al., 2018). The value of such high pixel resolutions can be appreciated within certain applications, such as crop scouting (Hunt Jr. and Daughtry, 2018). In other applications, such as irrigation management, however, this extra spatial detail can become unnecessary or even unwise (Jones and Sirault, 2014). Mismatches can exist between the observation scale at which UAV images are collected, and the application scale where decisions are implemented. Drip irrigation systems, for example, operate on a spatial scale from 1-10 m^2, central pivots on 100 m^2, and furrow irrigation on 1000 m^2 (Smith et al., 2009). If UAV imagery is more detailed than is necessary, prolonged processing times can even delay the delivery of the end product. A recent customer survey report by Nieto (2017) indicates that most users require ET maps less than a day after image acquisition, a demand that can be met with UAV systems, given the proper data.

In addition to the application scale, UAV images can also present discrepancies with respect to the ET modeling scale. In particular, mismatches may result between the defined modelling scale and processes that define these models such as shear-driven turbulence (Raupach and Finnegan, 1995). These discrepancies are most apparent within LE algorithms such as the two-source energy balance (TSEB) model. TSEB models were initially developed and applied at pixel resolutions associated with non-commercial SATs (e.g. 60-120 m pixel resolution) (Kustas et al., 2003; Kustas et al., 2004; Li et al., 2005). Under TSEB, canopy and soil temperatures (T_c and T_s, respectively) are estimated at each pixel, which are then used to find LE as a residual from the energy balance equation ($LE = R_n - G - H$). The assumption behind TSEB models, therefore, is that each pixel contains both vegetation and soil components. However, such assumptions are not always met with UAV imagery, where pixel resolutions can be fine enough to capture only one of these components. Under these conditions, TSEB models, therefore, may not provide reliable estimates of LE, since the model algorithms were not designed to operate at that particular scale.

Discussion from previous paragraphs suggest that the scale at which UAV images are collected (or observation scale) are often at odds with the management (or application) and/or modelling scales, and this issue is actually quite common within remote sensing studies (Wu and Li, 2009). Discrepancies between observation, management, and modelling scales can be mitigated by transferring information using scaling techniques (Woodcock and Strahler, 1997). In the case of UAVs, one such

scaling technique can be performed through up-scaling, or aggregating, images to a coarser pixel resolution (Hassan-Esfahani et al., 2017).

Initial studies quantifying the effects of aggregation on ET (or LE) modeling have been primarily confined to pixel resolutions associated with SAT imagery (Su et al., 1999; McCabe and Wood, 2006). Sharma et al. (2016), for example, aggregated Landsat 5/7 thermal/optical imagery from their original resolutions to various pixel resolutions (60, 90, 120, 150, 240, 360, 480, 600, 750, 900, 990 m), and then ran contextual Surface Energy Balance System (SEBS) ET models at each resolution, a process called input aggregation. In their results, they reported relative canopy ET (or ET_c) pixel scale errors ranging from 25-60 %, which they attributed to changes in sensible heat (H), specifically roughness length for heat and momentum (z_{oh} and z_{om}, respectively). Hong et al. (2009) suggest that input aggregation is detrimental when model parameters (such as z_{oh} and z_{om}) behave in a non-linear fashion. Sharma et al. (2016) also found that pixel scale ET_c errors were reduced when the fluxes were modeled at the initial Landsat resolution, and then aggregated, an alternative process called output aggregation.

Bahir et al. (2017) recently suggested that errors from input-aggregated SEBS fluxes could be reduced by applying alternative aggregation rules (e.g. for linear, harmonic, geometric roughness length averaging). For example, Ershadi et al. (2013) tested various LE average schemes (simple averaging, nearest neighbor, bilinear, cubic convolution) from SEBS and found that simple averaging was the best choice for aggregating or upscaling Landsat 5 imagery. However, the optimal averaging rule has rarely been analyzed in terms of non-contextual ET models such as TSEB. TSEB can be favorable

over SEBS and contextual models in general because it eliminates the need for empirical corrections of excess resistance (i.e. z_{om}, z_{oh}) (Liou et al., 2014). In one of the few papers on the topic, Bahir et al. (2017) showed that, at least with ASTER SAT imagery, ET fluxes using TSEB models were more conservative across spatial scales (i.e. 0.1-1 km) than contextual models such as SEBS.

While the topic of image aggregation has been primarily limited to SAT platforms, a recent study by Ramírez-Cuesta et al. (2019) extended this analysis towards high resolution manned airborne imagery (~0.5 m). In their methodology, a contextual model called the Mapping EvapoTranspiration at high Resolution with Internalized Calibration (or METRIC) was applied at various resolutions (5-1000 m) using input aggregation. In their results, they found that the turbulent fluxes (i.e. latent and sensible heat), behaved in a non-linear manner at resolutions higher than 30 m, with substantial aggregation errors (up to 23 %). However, such studies have not been extended towards UAV imagery, where image quality can vary depending on weather conditions (e.g. wind, rain, temperature etc.) and/or sensor quality (Manfreda et al., 2018).

While Sharma et al. (2016) previously discovered SAT imagery was affected by surface roughness length, it is by no means the only source of aggregation errors for LE aggregation. Moran et al. (1997) suggest that additional sources of error from both SAT and manned aircraft imagery include surface heterogeneity and atmospheric stability. Surface heterogeneity, or vegetation patchiness, was cited as the main driver of TSEB-based ET estimates when aggregating high resolution (i.e. 90 m) ASTER imagery (Bahir et al., 2017). If a landscape is relatively homogenous, less errors are expected when

aggregating UAV fluxes to coarser resolutions, and this will determined by crop phenology or growth stage (McCabe and Wood, 2006). Site heterogeneity is also a function of time of day, time of year, sensor spatial resolution, wind speed, and surface roughness properties (Moran et al., 1997; Kustas and Norman, 2000). The effects of such errors are often found within the sensible heat (H) component of the energy flux equation (Ramirez-Cuesta et al., 2019).

Even if UAV images were collected or aggregated to the proper application scale, it is not quite clear how such imagery compares with that collected from other platforms (i.e. UAVs vs. MAVs, UAVs vs. SATs). Within this context, platform selection towards ET modeling remains an open question, as UAVs, MAVs, and SATs each have their set of pros and cons (Matese et al., 2015). While some have argued that UAVs, MAVs, and SATs can work in a complementary manner (https://www.expouav.com/news/latest/drones-vs-SATs-competitive-complimentary/; https://www.expouav.com/news/latest/drones-vs-manned-aircraft/), it will not always be possible, or even necessary, to acquire imagery across all three platforms. This is especially true in situations where UAV processing times are too cumbersome, MAV costs are too high, and/or SAT images are unavailable or of poor quality. Therefore, it is worth investigating how UAV ET maps compare with MAV and SAT ET maps, in terms of aggregation and accuracy relative to established LE techniques whenever possible (Kustas et al., 2004).

The purpose of this study is to investigate the scaling properties of UAV-based LE estimates from a TSEB model. In particular, the interest is in comparing the different

modes of UAV aggregation (i.e. input vs. output, linear vs. non-linear averaging) at partial and full canopy cover conditions from a cotton row crop. There is additional interest in determining the contributing sources of error that result from these different aggregation modes. Finally, UAV maps are compared with those obtained from manned aircraft vehicles and SATs.

4.2. Materials and Methods

4.2.1. Study area and management

The study site (17-ha, 30.531° N, -96.431° W) is located on the Texas A&M Experimental Farm in central-eastern Texas (Fig. 4.1). The region has a humid subtropical climate according to the Köppen climate classification system (Cfa code). Soil color varies within the field, with darker and lighter soils on the left and right sides of the field, respectively. Soil surface textures include silt loam, silty clay loam and silty clay (Stanislav, 2010) and are classified as Vertisols, Inceptisols and Entisols (Jurena, 2005). The soils are actively forming on floodplains from primarily eolian parent materials once sourced from the Texas High Plains region (Sidwell, 1940). Elevations are relatively constant, with an average elevation of 67.7 ± 0.3 m above ground level. Total in-season precipitation and average daily air temperatures based on local rain gauges (red circles, Fig. 4.1), was 495 mm and 26.0 °C, respectively.

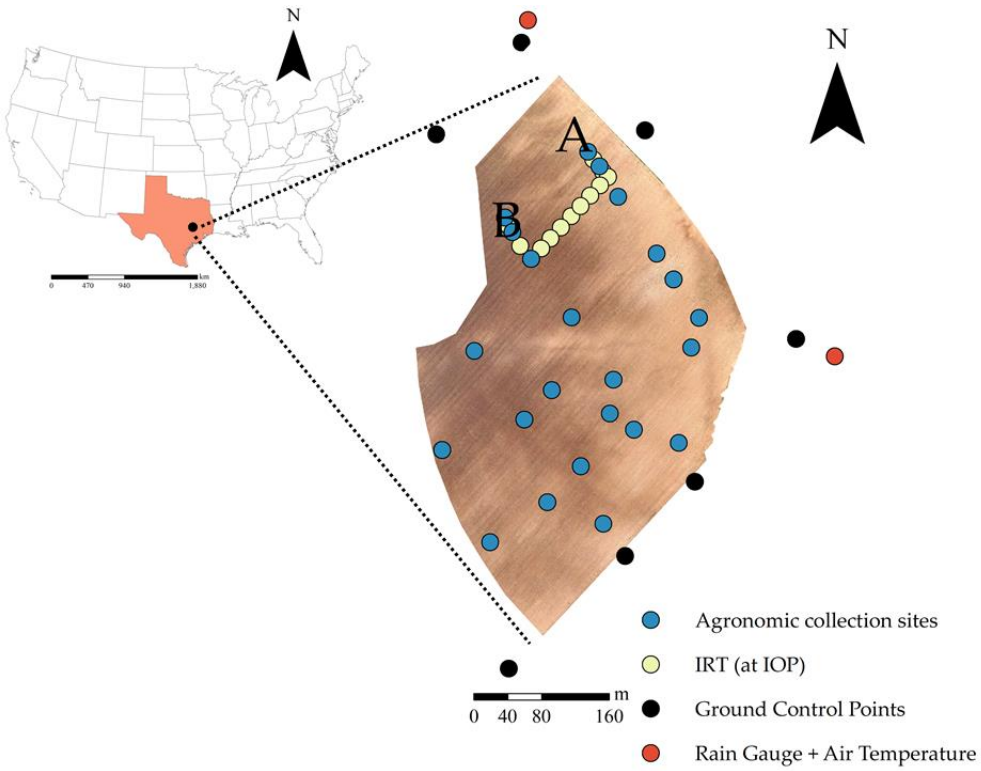

Fig. 4.1 Location of study area within the United States and the state of Texas. The letters 'A' and 'B' refer to two different eddy covariance towers installed during the 2017 field season (ref. Section 4.2.5.). Visual image was obtained by a consumer grade digital camera aboard a UAV about two weeks before planting (April 5, 2017). Also shown are locations of various field equipment and agronomic data deployed throughout the 2017 growing season. Agronomic collection sites include measured variables such as leaf area index (LAI), canopy height, and canopy width. Additional infrared thermography (IRT) measurements were consistently collected at the time of each UAV overpass or intense observation period (IOP) (yellow) for UAV temperature validation.

In past seasons, the field was actively managed with conventional tillage practices and kept in a continuous crop rotation with alternate years of corn (*Zea mays L.*) and cotton (*Gossypium hirsutum L.*). On April 5, 2017, cotton (variety PHY 444 WRF) was planted at a rate of 111,200 seeds ha^{-1}, and at 1.02 m row spacing (DOY 95). Pre-emerge and post-emergence herbicides (Prowl H_2O, Cotoran 4L, Cornerstone Plus) were applied

to ensure uniform stand establishment. In-season management of cotton included fertilization, plant growth regulation, and weed control. Based on field measurements, first flowering was observed on June 8 (64 days after planting or DAP), with cutout (i.e. 5 nodes above white flower or NAWF) observed on July 1, 2017. Boll filling occurred approximately between June 29 and July 28 (85-112 DAP, defined here as 2 NAWF). Open bolls for about 90 % of the field occurred around September 1 (210 DAP). Defoliation occurred on September 9, 2017 (157 days after planting or DAP), and harvest was conducted on October 10, 2017 (188 DAP).

4.2.2. Image acquisition

One of the objectives of this study was to compared UAV aggregated LE imagery with those from MAV and SAT platforms. Table 4.1 shows the dates of intense observation periods (IOP) when UAV, MAV and SAT surveys were conducted over the field in the 2017 growing season. The images collected at these dates and times form the basis of images for this study. SAT in this study refers to Landsat 8, a satellite that operates in sun-synchronous, near-polar orbit. SAT thermal images are initially collected at 100 m but resampled to 30 m resolution via cubic convolution immediately after image acquisition (Roy et al., 2014). SAT multispectral bands are defined at 30 m resolution. The main growth stages selected for this study include cotton flowering and boll filling. Note that UAV multispectral and thermal surveys were conducted separately due to platform limitations. Survey altitudes for UAVs, MAVs, and SATs were approximately 0.12, 1.37, and 705 km, respectively (Table 4.1).

Table 4.1 Fight times and pixel resolutions for all Intense Observation Periods (IOP) dates. The local times associated with each multispectral and thermal surveys are also described by survey platform (i.e. UAV – Unmanned Aerial Vehicle; MAV – Manned Aerial Vehicle; SAT – Landsat 8), along with its reported altitudes and native or original pixel resolutions for each sensor.

Growing Stage	Platform	Altitude (km)	PM Flight Time - Multispectral	PM Flight Time - Thermal	Native Pixel Resolution (m)	
					MS	Thermal
			June 16, 2017			
Flowering	UAV	0.12	13:48-14:10	13:00-13:15	0.07	0.15
	MAV	1.37	13:58-14:10		0.48	1.32
	SAT	705	11:57		30	100
			July 26, 2017			
Boll filling	UAV	0.12	11:27-11:48	N/A	0.08	N/A
			July 28, 2017			
	UAV	0.12	No flight	14:46-15:00	N/A	0.15
	MAV	1.37	15:17-15:31		0.48	1.31

The lag time between the UAV and SAT surveys on June 16, 2017 was about one hour. Previous attempts were made to conduct a UAV thermal survey at the time of the SAT overpass (i.e. 11:57, Table 4.1) to ensure similar radiative conditions between platforms. However, cloud variability was present during the survey, and partial cloud cover was observed from the SAT imagery (Fig. A1). SAT images were not available on July 26 or July 28 (i.e. UAV thermal and multispectral surveys, Table 4.1) because the next overpass date was not until August 3, 2017. Both multispectral and thermal images were necessary to facilitate TSEB-PT modeling (Sect. 4.2.5.).

Relative to SAT, MAV surveys were conducted much closer in time to UAV thermal surveys. The average flight time for MAV surveys at 1.37 km was 13 minutes. All multispectral and thermal afternoon flights were conducted within ± two hours of solar noon, which is defined here as 13:30 (Table 4.1). The pixel resolutions from the multispectral camera was 0.48 m, while those from the thermal camera was 1.31 m (Table 4.1). Both multispectral and thermal sensors equipped on the MAV platform were flown at the same time. On July 26, 2017, only a UAV multispectral survey was conducted so that the TSEB-PT model could be run from UAV thermal surveys on July 28 (ref. Sect. 4.2.5.) – no UAV multispectral survey was conducted on July 28.

4.2.2.1. UAV sensors

Previous discussion of UAV flight preparation and execution can be found from Rouze et al. (in preparation). However, some additional details for sensors equipped aboard the Tuffwing UAV platform (Boerne, USA) are given in Table 4.2. The multispectral camera used in this study was the Micasense RedEdge (MicaSense, Seattle, USA). The RedEdge camera is a complementary metal–oxide–semiconductor sensor that detects visible and near-infrared radiation. Thermal images were collected using an ICI 8640-P sensor (Infrared Cameras Inc., Beaumont, USA, https://infraredcameras.com/). The 8640-P is an uncooled focal plane array microbolometer with Vanadium Oxide film. Previous use of the RedEdge and the ICI 8640-P sensors towards vegetation monitoring and plant phenotyping have been documented (Duan et al., 2017; Sagan et al., 2019).

Table 4.2 Remote sensing platform and sensor characteristics used in the study.

Characteristic	Multispectral Sensors			Thermal sensors		
	UAV	Manned Aircraft	Satellite	UAV	Manned Aircraft	Satellite
Platform	Tuffwing UAV Mapper	Cessna 206	Landsat 8	Tuffwing UAV Mapper	Cessna 206	Landsat 8
Sensor	Micasense Rededge	Nikon D810	Operational Land Image (OLI)	ICI 8640-P	FLIR SC660	Thermal Infrared Sensor (TIRS)
Number of channels	5 (RGB + NIR + Red Edge)	4 (RGB + NIR)	9 (RGB, NIR, SWIR)	1	1	2
Notable spectral wavebands (μm)	0.46-0.50 (Blue)	0.40-0.50 (Blue)	0.45-0.51 (Blue)	7.0-14.0	7.50-13.00	10.6-11.19 (used)
	0.54-0.58 (Green)	0.51-0.59 (Green)	0.53-0.59 (Green)			
	0.66-0.68 (Red)	0.60-0.70 (Red)	0.64-0.67 (Red)			
	0.80-0.88 (NIR)	0.83-1.00 (NIR)	0.85-0.88 (NIR)			
Resolution (px)	1280 x 960	7360 x 4912	7541 x 7691	640 x 512	640 x 480	7541 x 7691
Pixel pitch (μm)	3.8	4.9	?	17	25?	?
Focal length (mm)	5.5	20	886	12.5	37.6	178
FOV (°)	47.9	83.9	15	78	24	15
Output data	16-bit	16-bit	12-bit	14-bit	16-bit	12-bit
Ground image dimension (m)	106 x 79	1204 x 805 2462 x 1646	185000 x 180000	84 x 104	285 x 213 584 x 437	185000 x 180000

4.2.2.2. MAV sensors

MAV multispectral images were collected with a Nikon D810 camera (Melville, USA, http://www.nikonusa.com). Thermal images were collected using a FLIR SC660 sensor, which, like the ICI 8640-P, is an uncooled focal plane array microbolometer

(Wilsonville, USA, https://www.flir.com/). The FLIR SC660 has a slightly smaller range for detecting thermal radiation (7.5-13 μm) than the ICI 8640-P (7.0-14.0 μm, Table 4.2). The D810 multispectral sensor was set under manual settings, with an exposure time of 0.001 seconds. The D810 and SC660 also have previous applications in monitoring crop water status (Garcia-Tejero et al., 2018; Wu et al., 2018).

4.2.2.3. SAT sensors

Landsat 8 SAT imagery was obtained on June 16, 2017 from multispectral and thermal sensors aboard the platform, namely the Operational Land Imager (OLI) and the Thermal Infrared Sensor (TIRS), respectively. The OLI was manufactured by Ball Aerospace & Technologies Corporation, while the TIRS was built by the NASA Goddard Space Flight Center. More detailed information on the characteristics of these two sensors beyond Table 4.2 can be found elsewhere in literature (Knight and Kvaran, 2014; Reuter et al., 2015). While Landsat has two thermal bands, only band 10 (i.e. 10.6-11.19 μm) was used, as band 11 (11.5-12.51 μm) has stray light issues (Wang and Ientilucci, 2018).

4.2.3. Image post-processing

Previous discussion of UAV post-processing, including geometric/radiometric corrections, can be found from Rouze et al. (in preparation) and is omitted for the sake of brevity.

4.2.3.1. MAV

The goal of orthomosaicking MAV imagery was to only analyze images that cover the area spanned by the eddy covariance tower footprints for LE flux comparisons.

While the entire field was captured in a single shot with MAV multispectral imagery, such was not the case with the thermal imagery. Because thermal images define the ET modeling domain (Sect. 4.2.5.), and to simplify processing times, therefore, all MAV analysis was only conducted over these smaller portions of the field (Fig. A2).

After data acquisition, multispectral images were first corrected from RAW to 16-bit tiff files using the provided software (Capture NX-D 1.2.1). Because the multispectral sensor captured the entire field in one shot, mosaicking was not needed. Instead, only geo-referencing was needed using known coordinates of objects identified within the image. RGB and NIR images were first geo-referenced separately and then stacked together within ArcGIS (ESRI, Redlands, USA).

Multispectral radiometric calibrations were conducted using the empirical line calibration in order to obtain surface reflectance (Smith and Milton, 1999). The main interest was in estimating red and NIR reflectance (ρ_{Red}, ρ_{NIR}) only so that Normalized Difference Vegetation Index ($NDVI = \frac{\rho_{NIR}-\rho_{,Red}}{\rho_{NIR}+\rho_{Red}}$) could be calculated for later use in the LE modelling phase (Section 4.2.5). Ground-truth reflectance measurements were obtained with a Handheld 2 spectroradiometer instrument, which has a spectral range 325-1075 nm, a spectral resolution of < 3 nm, and a 25° FOV (ASD Inc., Boulder, USA). Four 8 x 8 m tarpaulins were used for radiometric calibration, with reported nominal reflectance values of 4, 16, 32, and 48 % (Zhang et al., 2017). The Handheld 2 collected reflectance data from these tarps during each MAV IOP, as well as measurements of soil and cotton reflectance for validation. In addition to measured

reflectance values, raw sensor information (i.e. digital numbers or DNs) were extracted from a 9 x 9-pixel box within each tarp in order to perform empirical line calibration.

All images collected by the thermal FLIR SC660 sensor were first processed to generate camera calibrated temperatures using the provided software (ExaminIR, FLIR). The settings supplied in ExaminIR were the same as those from the UAV processing software, mainly: 1) emissivity or $\varepsilon = 1.00$, 2) transmissivity or $\tau = 1.00$, and 3) air temperatures or T_a. At 1.37 km altitude, most of the field was captured in one shot (Fig. A2); therefore, like the multispectral imagery, image registration was only required, and this was done using the geo-referenced multispectral imagery as a visual aid. MAV thermal radiometric corrections, like UAV corrections from previous work (Rouze et al., in preparation), were performed at each pixel by calculating emissivity values weighted bed vegetation fraction cover (ε, Jimenez-Muñoz et al., 2006), followed by estimation of T_r from brightness temperature (T_{br}) and background air temperature (or T_{bg}, via local weather data) (Maes and Steppe, 2012).

4.2.3.2. SAT

Surface reflectance data from the visible/near-infrared wavelengths was obtained through the Landsat Ecosystem Disturbance Adaptive Processing System (LEDAPS). Raw thermal DNs was first obtained from the level 1 product using the United States Geological Survey (USGS) Global Visualization Viewer (GLOVIS, https://glovis.usgs.gov/). Raw DNs, along the surface reflectance data, were used to estimate T_r - detailed information regarding conversion of SAT DN to T_r can be found in Appendix A.

4.2.4. Model formulation

The purpose of this study is to evaluate how UAV LE fluxes change as a function of coarsening pixel resolution, and how such information compares with those from MAVs and SATs. Within this context, LE fluxes need to be obtained across the entire production field. To do this, LE fluxes were estimated using a combination of remote sensing and energy balance modeling techniques. The energy balance model used here was the TSEB model (Norman et al., 1995). Contextual energy balance models, while popular (Allen et al., 2007; Brenner et al., 2018; Ramirez-Cuesta et al., 2019), were hypothesized as unfavorable in this study because satellites were not expected to properly identify hot/cold temperature endmembers within the small study area (17-ha or 0.17 km^2).

The general approach to TSEB models estimate LE as a residual of the energy balance equation, which is based on the difference between available energy (R_n-G) and sensible heat (H). H is expressed from both soil and vegetation components as follows:

$$H = \rho C_p \frac{T_0 - T_a}{r_a} \quad \text{(Eq. 4.1)}$$

where ρC_p is the volumetric capacity of air (J m^{-3} K^{-1}), T_0 is the aerodynamic temperature (K), T_a is the air temperature (K), and r_a is the resistance to heat transport or aerodynamic resistance (s m^{-1}). In practice, T_0 is unknown and replaced with T_r, although this approach can result in an overestimation of H fluxes (Kustas and Norman, 2000). In this study, the sub-model used to estimate LE was the TSEB Priestley Taylor approximation model (TSEB-PT). Unlike other TSEB sub models (e.g. TSEB-DTD), the TSEB-PT model allows for comparisons between UAV, MAV and SAT LE fluxes

because it requires instantaneous thermal imagery at one point in time (Table 4.1). The model begins with an initial approximation of LE_c based on the Priestley and Taylor (1972) transpiration equation:

$$LE_c = \alpha_{PT} f_g \frac{\Delta}{\Delta + \gamma} R_{n,c}, \quad \text{(Eq. 4.2)}$$

where αPT is Priestley–Taylor parameter with an initial value of 1.26, Δ is the slope of the saturation vapor pressure-temperature curve (Pa K^{-1}) and γ is the psychrometric constant (Pa K^{-1}). After LE_c is initialized using Equation 1, H_c is then found, which then allows for T_c to be found as follows:

$$H_c = \rho C_p \frac{T_c - T_a}{r_a} \rightarrow T_c = \frac{H_c * r_a}{\rho C_p} + T_a, \quad \text{(Eq. 4.3)}$$

Where r_a is the aerodynamic resistance to momentum and heat transfer (s m^{-1}), ρ is the air density (kg m^{-3}), C_p is the specific heat of air (J kg^{-1} K^{-1}), and T_a is the air temperature at the time of overpass (K). With an initial T_c from Equation 3, T_s is found from a mixing model weighted by the vegetation fraction cover (f_c), and Tr values obtained from the sensor (Norman et al., 1995):

$$T_r = [f_c * T_c^4 + (1 - f_c) * T_s^4]^{1/4}, \quad \text{(Eq. 4.4)}$$

Note that, in order to obtain an initial T_c value, the fractional vegetation cover (f_c, Eq. 5) is calculated from Campbell and Norman (1998):

$$f_c(\theta) = 1 - \exp\left[\frac{-0.5\Omega(\theta)LAI}{\cos(\theta)}\right], \quad \text{(Eq. 4.5)}$$

where Ω is a vegetative clumping factor calculated at a given sensor viewing angle θ (Kustas and Norman, 1999), and *LAI* is calculated from multispectral imagery (see

Section 4.2.5.). A check on these T_c and T_s values is then performed by applying these newly found T_s values to find H_s:

$$H_s = \rho C_p \frac{T_s - T_a}{r_s + r_a}, \quad \text{(Eq. 4.6)}$$

where r_s is the soil resistance to momentum and heat transfer (s m^{-1}). Finally, LE_s is found from the energy balance of the soil ($LE_s = R_{n,s} – G – Hs$). A valid solution is reached when LE_s is positive. If a valid solution is found, the latent and sensible fluxes from both canopy (i.e. $LE_c = R_{n,c} – H_c$) and soil sources are respectively added together to compute the LE and H terms. A more detailed description of this model can be found from Norman et al. (1995) and Kustas and Norman (1999).

4.2.5. Model inputs and processing

In order to run TSEB-PT models for UAV MAV, and SAT imagery, both image and non-inputs need to be generated. Image inputs refer to spatially varying parameters such as T_r (ref. Sect. 4.2.3.), f_c, and LAI. Non-image inputs refer to constant parameters such as weather data and agronomic data such as canopy height (h_c) and canopy width (w_c). The following sections detail the derivation of this information separately.

4.2.5.1. Image inputs

All further discussion of input derivation applies to UAV, MAV, and SAT platforms. f_c was derived from NDVI imagery by scaling between the ‘infinite’ NDVI ($NDVI_\infty$) and soil NDVI ($NDVI_s$) (Carlson and Ripley, 1997):

$$f_c = \left(\frac{NDVI - NDVI_s}{NDVI_\infty - NDVI_s}\right)^2 \quad \text{(Eq. 4.7)}$$

$NDVI_\infty$ was taken to be the maximum NDVI observed from the native pixel size (0.976). $NDVI_s$ was based off average NDVI values at a time before squaring occurred (0.2). LAI maps were then generated by regressing in situ LAI (Fig. 4.1) against the f_c maps generated from above. LAI measurements were taken with a LAI-2200C sensor (LI-COR, Lincoln, USA), either one hour before sunrise or one hour before sunset. All LAI campaigns were collected in a two-day span from a UAV thermal overpass (Table 4.1). LAI measurements were taken approximately in an area spanning three meters by three rows. All LAI observations were collected directly underneath cotton plants along a row, and one-fourth, one-half, and three-fourths distance from the cotton row in accordance with LICOR recommendations. Table 4.3 shows field average characteristics of agronomic data collected at site locations shown in Fig. 4.1 (dark blue circles). The field average LAI values on June 16 and July 28 were 1.03 ± 0.22 and 2.37 ± 0.34 m^2 m^{-2}, respectively.

Table 4.3 Agronomic and weather data collected at the IOPs listed in Table 4.1, along with their units. Abbreviations are as follows: 1) LAI – leaf area index; 2) h_c – canopy height; 3) w_c – canopy width; 4) T_a – air temperature; 5) u – wind speed; 6) S_{dn} – downward incoming solar radiation; 7) VPD – vapor pressure deficit

Date	Time	Associated Platform	LAI	h_c	w_c	T_a	u	Wind direction	S_{dn}	VPD
			m^2 m^{-2}	m	m	K	m/s	°	W m^{-2}	kPa
June 16, 2017	11:57	SAT				304.3	3.78	213	878	1.79
June 16, 2017	13:00-13:15	UAV	1.03	0.44	0.14	306.1	3.88	205	1014	2.40

Table 4.3 Continued

Date	Time	Associated Platform	LAI	h_c	w_c	T_a	u	Wind direction	S_{dn}	VPD
			m^2 m^{-2}	m	m	K	m/s	°	W m^{-2}	kPa
June 16, 2017	13:21-13:47	MAV				306.3	3.32	197	1015	2.48
June 16, 2017	13:58-14:10	MAV				306.7	3.11	191	998	2.58
July 28 2017	14:46-15:00	UAV				309.6	1.84	166	945	3.55
July 28 2017	14:45-15:09	MAV	2.37	0.8	0.92	309.7	1.52	163	924	3.64
July 28 2017	15:17-15:31	MAV				310.1	1.77	189	898	3.73

4.2.5.2. Non-image inputs

Weather data was collected using 15-minute averaged sensor data obtained across both eddy flux towers. Weather parameters include (but are not limited to): 1) air temperature (T_a, K), 2) wind speed (u, m s^{-1}), 3) vapor pressure deficit (VPD, kPa), 4) incoming shortwave radiation (S_{dn}, W m-2) and 5) longwave radiation (L_{dn}, W m-2). Specific weather data on June 16 and July 28 (Table 4.1) are shown in Table 4.3.

Field agronomic information was obtained by averaging spatially distributed field measurements at each IOP (Fig. 4.1). Relevant information includes canopy height, canopy width, leaf width, leaf spectral properties, and leaf angle distribution. All canopy height and width measurements were visually observed across ten different plants each site using measuring tape. Leaf width was visually observed from the widest points between select leaves on each plant. Leaf spectral properties were obtained using local

ground-truth reflectance data. Leaf angle distribution was calculated from leaf tip angle measurements collected alongside LAI data (Wang et al., 2007).

Soil heat flux was calculated assuming a constant ratio between G and $R_{n,s}$, the latter of which was calculated using formulations provided by Kustas and Norman (1999). The use of a constant $G/R_{n,s}$ was based on the observation that that most PM thermal UAV surveys were collected around solar noon - Kustas and Daughtry (1990) suggest that the use of a constant ratio is appropriate for several hours around solar noon, after which a time lag exists between net radiation and soil heat flux. Green vegetation fraction was set to one for all model runs. View zenith angle was set to nadir or zero degrees.

4.2.6. General design of the experiments

The purpose of this study was to address the effect of UAV aggregation on LE flux estimations. The overall methodology used to address this question is shown in Fig. 4.2. Two basic aggregation rules, either from the input imagery or output fluxes, were applied to UAV imagery. Before these aggregation rules were applied, however, all image inputs (e.g. T_r, LAI, f_c) were first aggregated to a pixel resolution of 1.33 m – this step was performed so that assumptions of TSEB modeling (i.e. > 1 m) were satisfied. The choice of 1.33 m, in particular, was based on the nearest multiple of UAV thermal imagery relative to MAV (Table 4.1). Next, an input aggregation scheme was applied, whereby the initially aggregated imagery (at 1.33 m) were aggregated again to a coarser pixel resolution (5 m, 10 m, 30 m, 90 m), followed by a TSEB-PT model run at each resolution. To address the effect of different input image aggregation schemes, only one set of image inputs can be modified at a time. Therefore, initial analyses focused on

identifying the most sensitive image input parameter (i.e. T_r, f_c) via field histograms. The two candidate inputs variables were T_r and f_c. The 30 m resolution reflects satellite T_r disaggregation approaches using concurrent multispectral imagery (Kustas et al., 2003). The 90 m resolution reflects Landsat 8 thermal imagery satellite images aggregated to the closest multiple of its original resolution (i.e. 100 m) – this approach has precedence within literature (Cho et al., 2018).

The other aggregation scheme tested in this study was output flux aggregation, whereby the fluxes were first modeled at 1.33 m, followed by flux aggregation to the desired pixel resolution. The output aggregated flux resolution was aggregated to the same values as those from input aggregated approaches. This experimental design is like other studies addressing aggregation properties from satellite sensors (Su et al., 1999; Hong et al., 2009; Sharma et al., 2016).

Within a given aggregation scheme (i.e. input/output), additional sub-schemes were used to address the effect of field statistical distributions on aggregation. First, a simple mean or arithmetic average was calculated, with the assumption that image inputs or outputs behave linearly (labelled as SA in Fig. 4.2a). Second, a non-linear scheme was addressed by using a Box-Cox approach, whereby values where transformed to an optimal transformation power, arithmetically averaged, and subsequently backtransformed to obtain values in the original units (labelled as BC in Fig. 4.2a) – further description of the BC approach is given in Appendix B. Collectively, four individual aggregation schemes were tested for a given IOP date (hereafter referred to as In-SA, In-BC, Out-SA, and Out-BC in Fig. 4.2a). All TSEB-PT models were run within

the Python package pyTSEB, version 2.0 (https://github.com/hectornieto/pyTSEB, Source: Hector Nieto). Examples of UAV Out-SA LE images across both IOP dates are shown in Fig. 4.3.

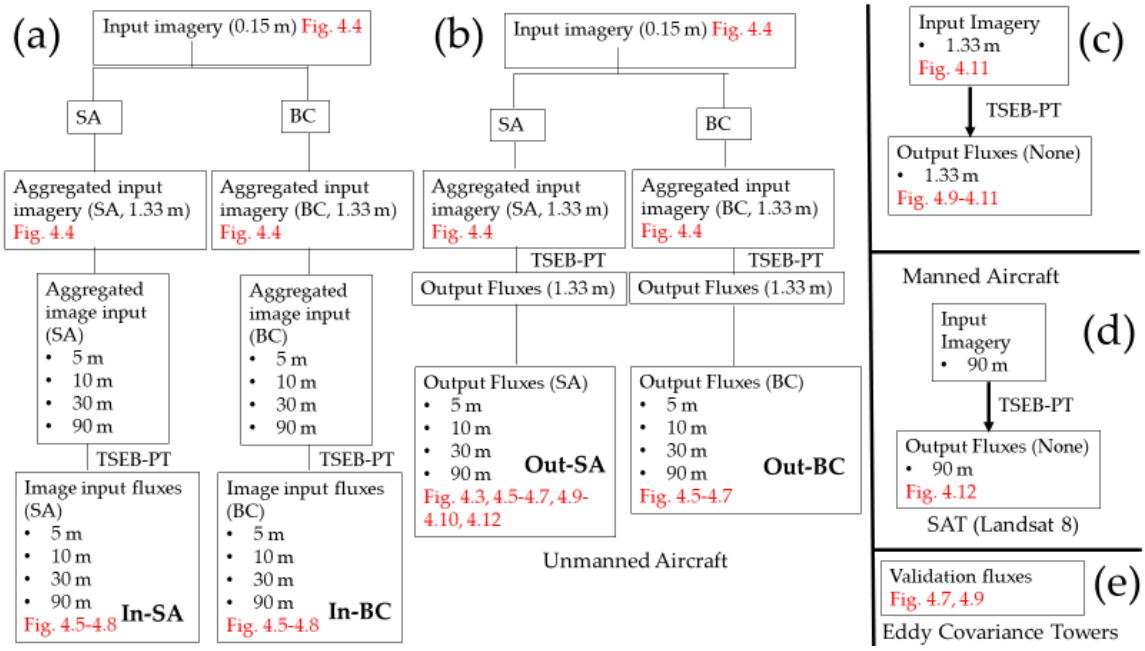

Fig. 4.2 Workflow for this study. Different processing steps applied to unmanned aerial vehicle (UAV) imagery (Fig. 4.2a-4.2b), manned aerial vehicle (MAV) imagery (Fig. 4.2c), satellite (SAT) imagery (Fig. 4.2d), and d) eddy covariance flux towers (Fig. 4.2e). The steps outlined in Fig. 4.2a apply to the different processing routes from a single set of multispectral and thermal IOP images. Within Fig. 4.2a, two different aggregation methods referred to as input aggregation (Fig. 4.2a) or output aggregation (Fig. 4.2b). Image inputs refer to f_c, LAI, and T_r (e.g. 0.15, 1.33 m, 30.0 m, 90 m from Fig. 4.2a). Output fluxes refer to R_n, G, H and LE modeled using TSEB-PT. SA – simple (arithmetic) average; BC – Box-Cox averaging. In-SA: Input aggregation using arithmetic mean; In-BC: Input aggregation using Box-Cox transformation; Out-SA: Output aggregation using arithmetic mean; Out-BC: Output aggregation using Box-Cox transformation. Boxes designated with figure numbers (in red) should be used to interpret figures presented in the paper.

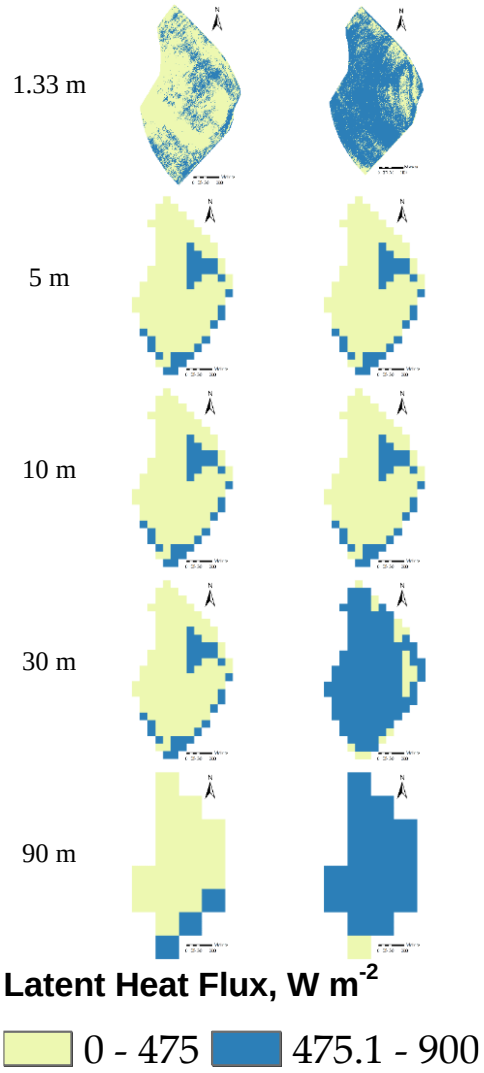

Fig. 4.3 Output flux aggregation (Out-BC, Fig. 4.2) for latent heat fluxes on June 16 (left side), and July 28 (right side).

One of the primary goals of this study was to address which aggregation scheme (i.e. In-SA, In-BC, Out-SA, Out-BC) produced the lowest: 1) pixel-scale errors, and 2) prediction errors (with respect to eddy flux towers). First, pixel scale relative errors were

calculated, which compare the value at the selected aggregated resolution against the individual pixels from which it is comprised. Relative error (R_e) is calculated as R_e=RMSE/μ (Kalma et al., 2008), where RMSE is the root-mean-square error difference between the coarse resolution pixel and its constituent fine resolution pixels, and μ is the spatial mean value of all the fine resolution pixels. Second, the modelled fluxes (i.e. In-SA, In-BC, Out-SA, Out-BC) were compared eddy covariance towers installed within the field during each IOP (Fig. 4.1). Quality of fit was assessed in terms of mean absolute percentage error (MAPE):

$$MAPE = \frac{100}{n}\sum_{j=1}^{n}\left|\frac{\hat{y} - y}{y}\right| \quad \text{(Eq. 4.8)}$$

where $\hat{y}$ and y are the UAV/MAV modelled and eddy covariance LE fluxes, respectively. Description of flux tower data is given in Rouze et al. (in preparation). Appendix C provides the method used to obtained remotely sensed weighted fluxes within the footprint of each eddy tower, as well as the extraction of energy balance components from the flux towers.

4.3. Results

4.3.1. Comparing UAV aggregation approaches

The purpose of this study is to evaluate the different aggregation approaches (In-SA, Out-SA, In-BC and Out-BC, Fig. 4.2), in terms of: 1) R_e on the pixel-scale, and 2) absolute errors with respect to eddy flux towers. Analysis begins by first presenting histograms for T_r and f_c on different dates and resolutions as shown in Fig. 4.4. Because LAI is derived from f_c (Section 4.2.5.1.), it is omitted here for the sake of brevity. The

purpose here is to determine the relative sensitivity of these parameters to aggregation, as this will determine which parameter will then be tested in terms of averaging rules (e.g. In-SA, In-BC, Fig. 4.2). Each panel in Fig. 4.4 has the distribution of f_c and T_r at the native resolution as black lines (i.e. 0.07 and 0.15 m, respectively, Table 4.1), as well as the aggregated resolution, either using SA (green lines) or BC (pink lines) averaging approaches.

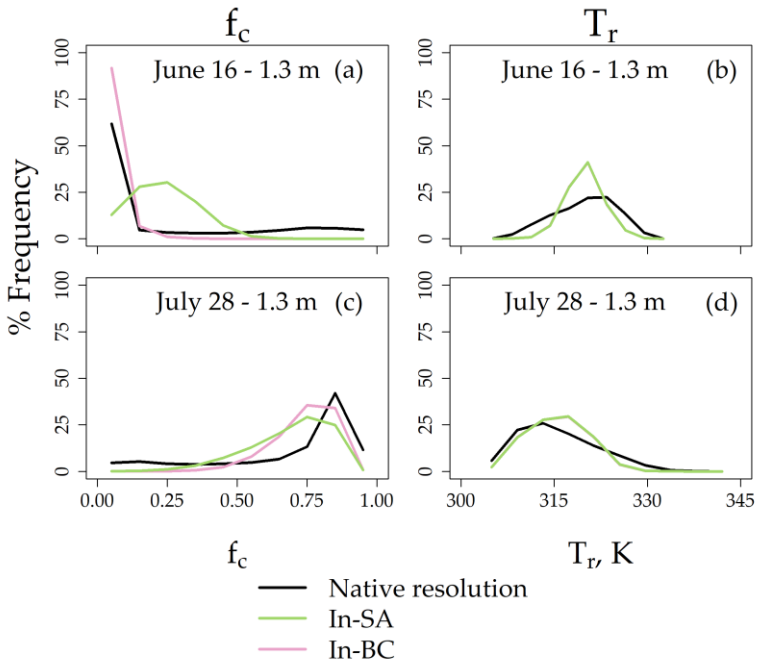

Fig. 4.4 Line histograms for f_c and T_r imagery on June 16 (Fig. 4.4a-4b), and July 28 (Fig. 4.4c-4.4d), expressed in terms of percent frequency. The histograms are calculated over pixels across the entire field. For the sake of brevity, the line histograms at 5, 10, 30 meters and 90 meters are not provided here.

One observation that can be made from Fig. 4.4 is that the distribution of the f_c and T_r curves for the native and aggregated images shift in time. For example, on June 16 the f_c curves are primarily right-skewed (Fig. 4.4a), while on July 28 these f_c curves shift to left-skewed distributions (Fig. 4.4c). On June 16, T_r curves were approximately normal (Fig. 4.4b), while on July 28 these distributions shifted towards right-skewed distributions (Fig. 4.4d). These shifts in f_c and T_r correspond with the increased vegetative cover (and decreased soil exposure) during the two sampling dates (Table 4.3). On July 28, the distributions from f_c and T_r behave in a somewhat inverse manner, as both show left- and right-skewed distributions, respectively (Fig. 4.4c, 4.4d), most likely because of changes in crop phenology.

In comparing distributions within and across aggregation methods, several observations can be made. On June 16, and to a lesser degree July 28, f_c-SA (green line) and f_c-BC (pink line) field distributions are visually different from each other, particularly for the low-medium values of f_c (0-0.5, Fig. 4.4a). In particular, the f_c-SA distribution on June 16 contains a greater amount of f_c pixels between 0.1-0.5 than the f_c-BC or f_c-native imagery (Fig. 4.4a). Moving from June 16 to July 28, f_c differences between SA/BC and native resolution (0.15 m) become less noticeable, although both aggregated distributions are shifted slightly to the left from the native distribution (Fig. 4.4c). In particular, f_c-SA shows a greater proportion of pixels associated with vegetation than that of f_c-BC (Fig. 4.4c). This result may have occurred because In-SA effectively mixes high and low end values (from vegetation and soil, respectively), while In-BC

weights values more towards high values (based on the greater proportion of vegetation via the transformation power, Appendix B).

Unlike f_c, differences in T_r distributions by aggregation rule were not observed. On June 16, for example, the T_r distributions for both SA and BC aggregation were almost identical (Fig. 4.4b), and this was also observed on July 28 (Fig. 4.4d). From these observations, two main points can be made. First, the sensitivity of f_c to aggregation rule (i.e. SA vs. BC) was greater during partial than full vegetation coverage. Second, f_c was more sensitive to the selected aggregation rule than T_r, and this may have occurred because f_c is expressed on a much smaller scale relative to T_r (i.e. 0-1). For this reason, all further results for input aggregation will be discussed in terms of f_c (and LAI) input aggregation only. In other words, In-SA and In-BC refer to aggregation techniques from f_c (and LAI) imagery only (Fig. 4.2).

Fig. 4.5 shows histograms from LE fluxes across the field at two different pixel resolutions (5 m, 10 m) and IOP dates. Within each panel, field distributions at initial aggregation level (1.33 m, black) are plotted alongside input (i.e. f_c) aggregated images (blue) and output flux aggregated images (orange). Note that the T_r arithmetic averaging was consistently used for all aggregation schemes. The peak LE flux encountered on June 16 and July 28 was around 400 W m^{-2} and 500 W m^{-2}, respectively. On June 16, LE histograms become generally narrower as the pixel resolution is aggregated from its native counterpart (Fig. 4.5a, 4.5b). The most likely reason for this result is that soil and vegetation pixels are being increasingly averaged when pixel resolutions become greater than the width of the soil row (~0.5 m), resulting in less variation relative to the finer

resolution imagery. When moving from June 16 to July 28, the LE field histograms across native and aggregation types shift from approximately normal to left-skewed, indicating greater vegetation coverage (Fig. 4.5a vs. 4.5c, Fig. 4.5b vs. 4.5d). A general trend that persists across all aggregation distributions on July 28, relative to the native distribution, is that the former has a larger proportion of pixels in the mid-range (i.e. 400-600 W m^{-2}), presumably due to averaging of vegetation and soil pixels, regardless of aggregation/averaging approach.

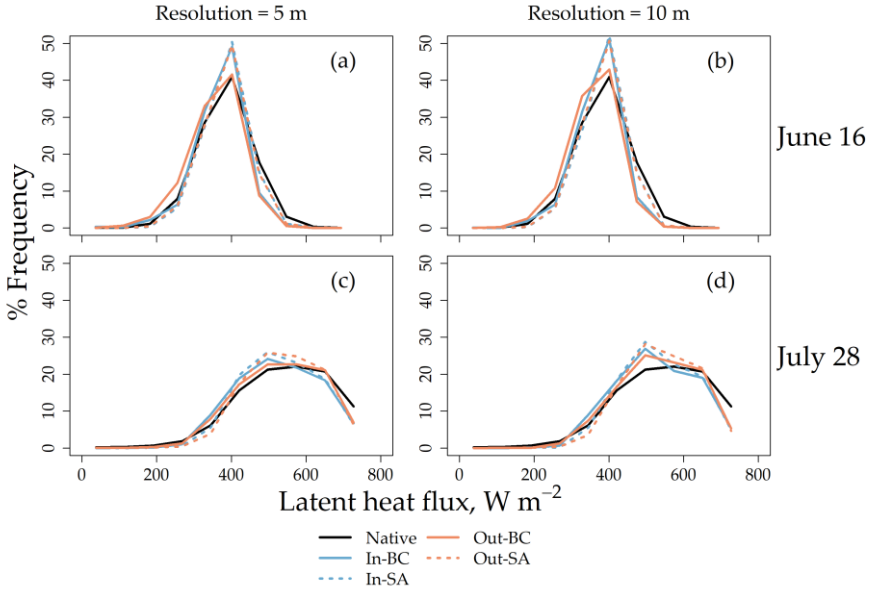

Fig. 4.5 Line histograms of latent energy (LE) fluxes using TSEB-PT across different IOP dates and times: a) June 16 at 0.74 m; b) June 15 at 1.33 m; c) July 28 at 0.74 m; d) July 28 at 1.33 m. Different colors and line types are assigned to In-BC (bold blue), In-SA (dashed blue), Out-BC (bold orange), and Out-SA (dashed orange) fluxes at various pixel resolutions. Native fluxes (~0.15 m, black) are also plotted as reference. Refer to red arrows for discussion in-text.

Unlike the f_c field distributions (Fig. 4.4a, 4.4c), the LE field distributions by aggregation and averaging methods (In-BC, Out-BC, In-SA, Out-SA) are pretty similar to each other on both sampling dates (Fig. 4.5). While this may suggest that the selection of correct aggregation and averaging approach is diminished, high differences (as much as 100 W m^{-2}) were visually observed between the approaches on a per-pixel basis (not shown here). Further visual inspection revealed that these differences were more prevalent within less densely vegetated areas. In other words, the selection of aggregation and averaging approach is mostly relevant to heterogenous surfaces, and this observation is in line with previous findings (Moran et al., 1997).

Based on these observations, as well as Fig. 4.5, further insights into LE aggregation behavior were quantified by calculating R_e for each of the scenarios shown in Fig. 4.2. In particular, LE pixel scale errors (R_e=RMSE/μ, Sect. 4.2.6) are plotted as a function of four different pixel resolutions (5 m, 10 m, 30 m, 90 m) in Fig. 4.6, and these errors are given in Table 4.4. As expected, the magnitude of relative error, regardless of aggregation method, increased with increasing pixel resolution - this is because the signal/noise ratio is diminished as the pixel size increases relative to the sensed objects (i.e. crops/soils) (Jones and Sirault, 2014). R_e values for all aggregation methods were lower on July 28 (Fig. 4.6b) than on June 16 (Fig. 4.6a), as the median R_e from Table 4.4 was 0.16 and 0.20, respectively. Differences between the 25th and 75th percentiles of different aggregation methods are more noticeable on June 16 than on July 28 as well (Fig. 4.6). These results most likely occurred because of the relatively high R_e errors on June 16 from both In-BC and Out-BC (Fig. 4.6a).

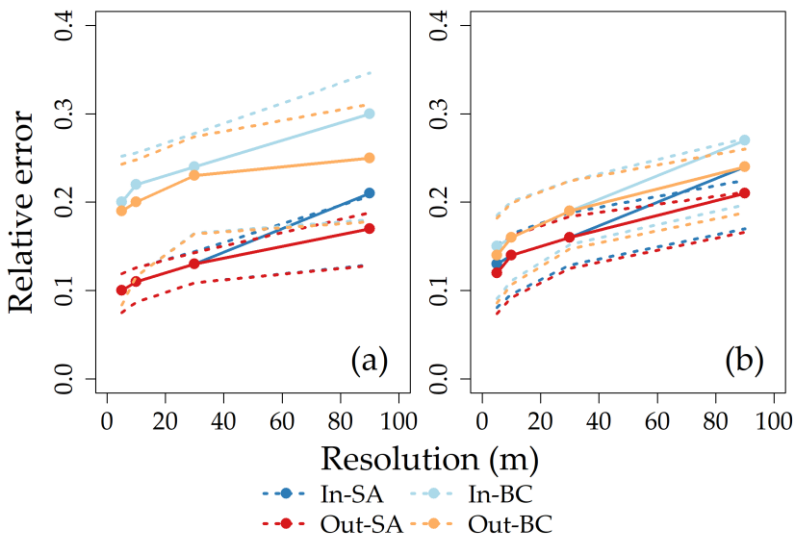

Fig. 4.6 Pixel-scale latent energy (LE) relative errors (R_e=RMSE/μ) plotted as a function of pixel resolution on a) June 16, 2017, and b) July 28, 2017. Plots are divided into In-SA (red), Out-SA (blue), In-BC (light blue), and Out-BC (orange). Within each aggregation configuration, mean relative errors (circle + bold line) are plotted as well as the 25th and 75th relative error percentiles (lower and upper dashed lines, respectively).

Table 4.3 Mean pixel scale relative errors from plots shown in Fig. 4.6 (scaled between 0-1).

Resolution	June 16, 2017				July 28, 2017			
	In-SA	In-BC	Out-SA	Out-BC	In-SA	In-BC	Out-SA	Out-BC
5	0.10	0.20	0.10	0.19	0.13	0.15	0.12	0.14
10	0.11	0.22	0.11	0.20	0.14	0.16	0.14	0.16
30	0.13	0.24	0.13	0.23	0.16	0.19	0.16	0.19
90	0.21	0.30	0.17	0.25	0.24	0.27	0.21	0.24
Average	0.14	0.24	0.13	0.22	0.17	0.19	0.16	0.18

R_e differences were exhibited not only across dates, but within dates as well. For a given sampling date, differences in relative errors between SA vs. BC transformation were smaller than those between input vs. output aggregation (Table 4.4). In order words, aggregated LE fluxes were more sensitive to selection of averaging rule than selection of aggregation method. In terms of comparison, relative errors from simple averaging (i.e. Out-SA, In-SA) were generally lower than BC (i.e. Out-BC, In-BC). For example, the median relative error for SA on June 16 was 0.14, while for BC it was 0.20. Within respect to the individual models, the magnitude of R_e were (from lowest to highest): Out-SA < In-SA < In-BC < Out-BC (Fig. 4.6, Table 4.4). Thus, output flux aggregation produced lower pixel-scale errors than using input aggregation with respect to SA. These trends are particularly apparent on June 16 (Fig. 4.6a), although differences are diminished on July 28 (Fig. 4.6b), presumably because of more homogenous (vegetated) surfaces. Therefore, it can be concluded that SA averaging (preferably with output flux aggregation) was the best aggregation approach towards upscaling UAV imagery, despite the apparent non-normal distributions presented in the inputs (Fig. 4.4c, 4.4d) and output fluxes (Fig. 4.5c, 4.5d).

The second criteria used to determine which aggregation method was optimal was through comparisons with from eddy flux towers. Fig. 4.7 shows plots of UAV aggregated LE fluxes (i.e. In-SA, In-BC, Out-SA, Out-BC) against the LE flux measured by the eddy covariance based LE fluxes, across both towers and dates (n = 4). Table 4.5 provides the MAPE values from each configuration and is expressed as error from the mean LE flux (467 W m^{-2}). One consistent result that appeared across all resolutions was

that the errors from output flux aggregation (i.e. Out-SA, Out-BC) were lower than that from input LAI aggregation (i.e. In-SA, In-BC). For example, at 5 meters the MAPE for In-SA was 7.2 %, while for Out-SA it was 6.0 % (Table 4.5). When comparing SA vs. BC averaging, the former were more accurate relative to eddy fluxes - the average BC MAPE for input aggregation was 8.2 %, while for SA it was 6.8 % (Table 4.5). In fact, the trends in MAPE are the same as the relative errors from Table 4.4: MAPE (Out-SA) < MAPE (In-SA) < MAPE (In-BC) < MAPE (Out-BC). Output aggregation approaches had slightly lower median MAPE values than input approaches (7.2 vs. 7.8 %, respectively).

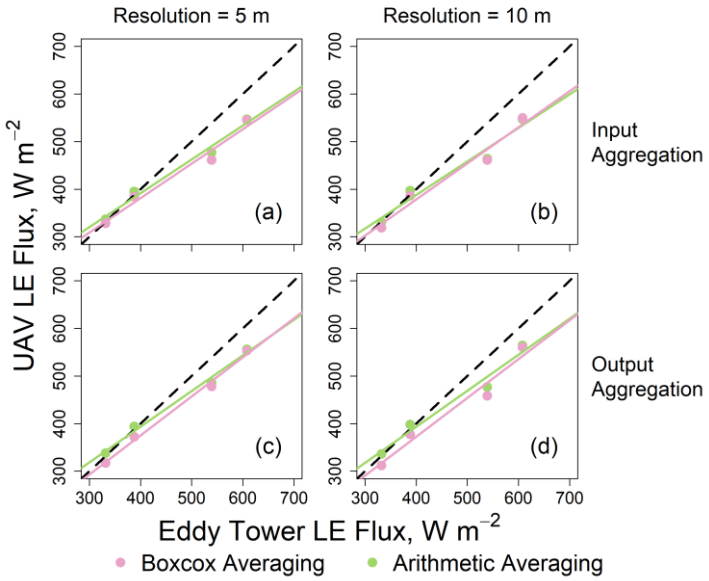

Fig. 4.7 UAV-based LE fluxes (y-axis) plotted against eddy covariance-based LE fluxes. Panels are then subdivided by aggregation method at various pixel resolutions. Note that each point represents a tower (Fig. 4.1) and IOP date combination. In-SA and In-BC are plotted in Figs. 4.7a-4.7b, while Out-SA and Out-BC are plotted in Figs. 4.7c-4.7d.

Table 4.4 Mean absolute percent errorsof different LE aggregated flux configurations between UAV and eddy flux towers.

Resolution (m)	In-SA	In-BC	Out-SA	Out-BC
5	7.2	8.0	6.0	7.9
10	7.8	8.1	6.2	8.6

Therefore, it was concluded that aggregating using SA (with output aggregation) was the best approach to upscale LE from 1.33 m, and this is in agreement with the pixel-scale results reported earlier (Fig. 4.6, Table 4.4). Input image aggregation can be dangerous if all inputs do not present similar statistical distributions, as was shown here (Fig. 4.4). Considering that many previous papers have opted for the input aggregation approach (Xia et al., 2016, Brenner et al., 2018), the use of output aggregation may need to be considered for future UAV aggregation studies.

4.3.2. Aggregation properties of UAV In-SA

Because input aggregation schemes, on average, underperformed relative to output aggregation schemes (Sect 4.3.1.), possible sources of aggregation errors were explored, with respect to both fluxes and model parameters. Input image parameters (T_r, f_c) and output ancillary parameters (r_a, u^*) were investigated by plotting R_e values as a function of pixel resolution (i.e. 5 m, 10 m, 30 m, 90 m). r_a and u^* were included in this study because they have been cited as contributing sources in regard to aggregation (Moran et al., 1997).

R_e values from the same set of inputs and outputs are provided in Fig. 4.8. The data presented in Fig. 4.8 are parameters obtained from arithmetic averaging (i.e. In-SA). R_n-G errors were less than 10 % across resolutions and were very low relative to the turbulent fluxes (i.e. LE/H, Fig. 4.8a, 4.8b). This finding has been observed across both non-contextual and contextual models, as R_n is affected more by solar properties than vegetation/soil properties (Bahir et al., 2017; Ramirez-Cuesta et al., 2019). The LE relative error values were similar on June 16 (partial vegetation cover) and July 28 (full vegetation cover) (Fig. 4.8c-4.8d). Because LE is calculated as a residual from R_n-G and H, it stands to reason that H errors are contributing to LE aggregation errors, and this was in fact observed from the data, particularly on July 28 (Fig. 4.8f). The effect of this H error on July 28 resulted in greater LE R_e values ranging from 2-5 %.

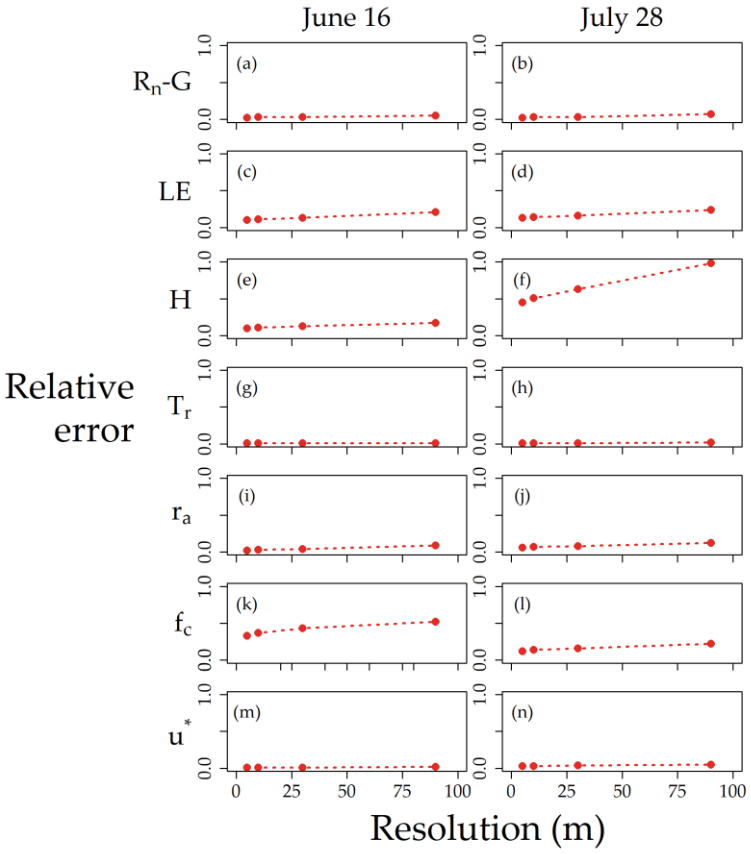

Fig. 4.8 Relative errors (scaled from 0-1) for the same variables as Fig. 4.8, plotted by pixel resolution on June 16 (left column) and July 28 (right column). Note that R_n, G, H and LE refer to images obtained via the In-SA aggregation method.

With respect to model parameters, r_a errors were relatively low, ranging from 1-5 % (Fig. 4.8i, 4.8j). f_c relative errors were much higher than r_a, although these errors decreased from June 16 to July 28 (Fig. 4.8k, 4.8l). u^* relative errors were lower than both r_a and LAI, although its errors similarly decreased in time (Fig. 4.8m, 4.8n). T_r relative errors were low and constantly close to zero across both dates (Fig. 4.8g, 4.8h). Thus, f_c appears to the main source of aggregation error during partial canopy and full canopy stages, as was the case in previous studies (Bahir et al., 2017). These findings

reaffirm the importance of f_c as stated by the original model creators (Norman et al., 1995). However, given that input image aggregation was not the best approach in this study (Fig. 4.6, 4.7), f_c (and LAI) errors can be avoided through the use of output flux aggregation, preferably by first choosing a pixel resolution suitable for TSEB-PT modeling (> 1 m, Raupach and Finnegan, 1995).

4.3.3. UAV aggregation as compared with MAV and SAT imagery

Next, the interest is in comparing one UAV aggregated technique (In-SA, Fig. 4.2) with those from MAV and SAT. This is first shown in Fig. 4.9, where UAV In-SA and MAV LE fluxes (at its resolution, Table 4.1) are plotted against eddy covariance LE fluxes. Fig. 4.9 shows that, across both sampled MAV altitudes, UAV Out-BC more accurately replicates eddy LE fluxes. For example, the MAPE values from UAV LE fluxes is 7.0 % at the 1.33 m pixel resolution. In contrast, the MAPE value from MAV was at 19.6 %. The scatterplot between UAV Out-BC and eddy LE fluxes are not outwardly biased (Fig. 4.9). Therefore, aggregated UAV LE fluxes, given the limited number of sampling points, are a more suitable approach towards accurately estimating ET than using MAV remote sensing.

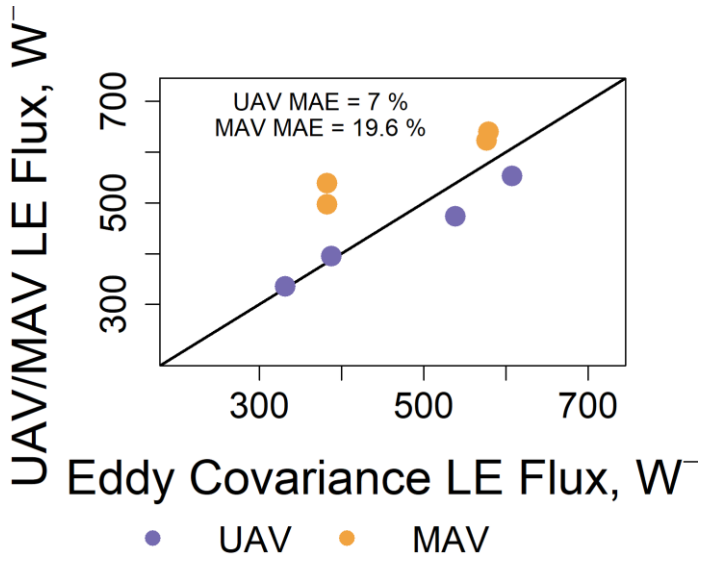

Fig. 4.9 UAV (purple)/MAV (orange) modeled LE flux (y-axis) vs. eddy covariance LE flux (x-axis). Fluxes obtained around the resolution of the MAV survey at 1.37 km altitude.

Trends observed at the flux towers (Fig. 4.9) were also observed across the whole field (Fig. 4.10), whereby modeled LE fluxes were greater from MAV than UAV imagery. One reason why this trend might be occurring is because T_r decreases as the survey altitude increases from UAV (purple) to MAV (orange) surveys (Fig. 4.11). All things being equal, lower T_r signatures result in higher LE fluxes due to evaporative cooling mechanisms. Fig. 4.11 also shows that the UAV aggregated T_r encompasses a greater range than that encountered by the MAV T_r. In this situation, therefore, the MAV uncooled microbolometer may be unsuitable for accurately capturing or estimating LE, especially when UAV aggregated solutions offer particular promise.

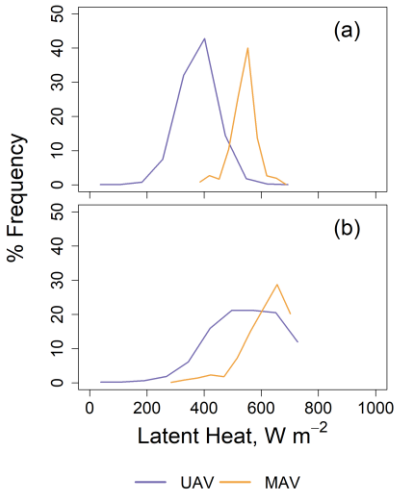

Fig. 4.10 Line histograms from aggregated UAV LE fluxes (purple) and from non-aggregated MAV LE fluxes (orange) across the entire field, on (a) June 16 and (b) July 28. Bold lines refer to the resolution closely resembling MAV surveys at 0.66 km altitude, while dashed lines refer to MAV surveys at 1.37 km.

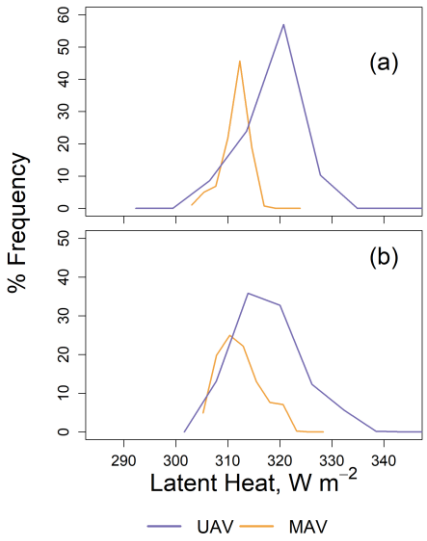

Fig. 4.11 Whole-field T_r histograms from UAV (1.33 m, purple) MAV (1.3 m, orange) surveys on (a) June 16 and (b) July 28.

In addition to MAV, UAV aggregated LE fluxes via Out-SA were compared with SAT LE fluxes, both across the field and the eddy tower. Fig. 4.12 shows the spatial correlation between UAV LE (y-axis) and SAT LE (x-axis) fluxes on June 16, 2017, from the limited sample area (Fig. A1). Whole-field comparisons between UAV and SAT LE reveal large differences in modeled LE, with UAVs ranging from 315-506 W m^{-2}, while SAT only range from 430-472 W m^{-2}. Note that this data is coming from areas that do not fall under cloud shadow (Fig. A1). While the LE fluxes between platforms are not entirely comparable due to differences in thermal acquisition times (Table 4.1), Fig. 4.12 does indicate that UAV aggregated LE fluxes, at the same resolution, are more variable than SAT LE fluxes. Therefore, any errors induced in the aggregation process may be acceptable because it may capture intra-row variability and its patterns (Matese et al., 2015).

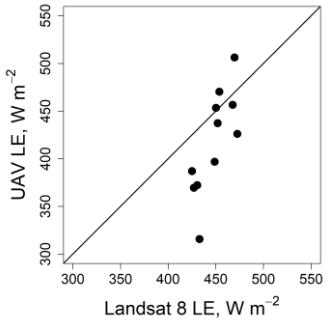

Fig. 4.12 Pixel-wise comparisons between UAV (y-axis) and SAT (x-axis) LE fluxes on June 16, 2017. Note that UAV LE fluxes were aggregated using Out-BC up to the SAT resolution (i.e. 90 m).

Flux comparisons between UAV and SAT platforms at the tower were performed like that from Fig. 4.11, except here fluxes were extracted from single pixels encompassing eddy tower B (Fig. 4.1, A1). Given the one tower data point on June 16, the residual error between UAV and eddy flux LE was -52 W m^{-2}, while between SAT and eddy flux it was 126 W m^{-2}. Therefore, while the number of data points are very limited, there is initial evidence to suggest that aggregated UAV fluxes (via Out-SA) are more accurate than SAT approaches – such a study should aim to collect imagery beyond the single year of data presented here.

4.4. Discussion

Given the rapid developments of UAV technology and the diversity of its applications, UAVs are expected to provide value to farmers. For example, UAVs can be used monitor agricultural and natural ecosystems and its state variables such as vegetation status, soil moisture content, and stream flow (Manfreda et al., 2018). However, certain applications, such as irrigation management, have not been performed with UAVs, as its information is often too detailed for practical applications (Jones and Sirault, 2014). Therefore, the purpose of this study was to evaluate ultra-high (cm-scale) UAV aggregated imagery within the context of ET modeling.

Out of the parameters selected in this study, the largest aggregation errors were predominantly attributed to f_c across both IOP dates (Fig. 4.6, 4.7). Here, it was assumed that f_c could be used as a proxy for LAI, based on the methodology described in this paper (Section 4.2.5.1.). This study reinforces previous observations that, even with

high-resolution UAV imagery, the surface heterogeneity of the site is a major factor that controls remotely sensed ET aggregation properties (Moran et al., 1997). These findings agree with other TSEB aggregation studies such as Bahir et al. (2017), although their study was restricted to SAT imagery. f_c affects several components of the TSEB-PT model, including: 1) aerodynamic roughness length (or z_{om}), 2) zero-plane displacement height (or d), 3) shortwave canopy/soil net radiation ($S_{n,c}/S_{n,s}$), 4) longwave canopy/soil net radiation ($L_{n,c}/L_{n,s}$), 5) clumping index (Ω_0), and 6) canopy layer boundary resistance (or r_x) (Norman et al., 1995; Kustas and Norman, 1999).

Because R_n-G aggregation errors were relatively low (Fig. 4.8), f_c aggregation errors were most likely not manifested through the components of R_n (i.e. $S_{n,c}/S_{n,s}$, $L_{n,c}/L_{n,s}$). Other parameters of R_n that could potentially contribute to aggregation errors, such as shortwave albedo and emissivity, relative to other parameters (such as H), are minimal (Fig. 4.8a, 4.8b). Other papers have reported substantial error (greater than 50 %) due to differences in surface roughness alone (Moran et al., 1997). Therefore, it is likely that LAI aggregation errors are manifested in z_{om}, d, Ω_0, and r_x. All of these parameters, either directly or indirectly, affect the estimation of sensible heat (H), and this could explain its relatively large pixel scale errors (Fig. 4.8e, 4.8f). r_x, in particular, is used to calculate H_c ($H_c = \rho c_p \frac{T_c - T_{ac}}{r_x}$) and is calculated from LAI based on formulations from Norman et al. (1995) and Kustas and Norman (1999). It would be interesting to analyze alternative r_x models (Choudhury and Monteith, 1988; McNaughton and Van den Hurk 1995) and their effects on aggregated LE within the TSEB modeling suite.

The topic of effects of aggregation also have relevance within crops other than cotton. For example, olive orchards present additional modeling challenges, as the latter exhibited vertically non-uniform leaf area distribution. This problem was addressed from a recent study by Yi et al. (2018), where different soil resistance (r_s) schemes were modified and evaluated within orchard systems. However, their study designed their experiment around data collected from eddy flux towers and not from remotely sensed fluxes. Norman et al. (1995) suggest that, under partial canopy conditions, r_a may also be several times smaller than other resistance terms beyond r_a and r_x, such r_s. Future studies, therefore, might consider the potential influence of r_x and r_s on input aggregated schemes. Given that the output flux aggregation was a better approach here, however, the question may not be of utmost importance.

Another significant finding in this study was that the f_c aggregation properties (Fig. 4.4), as well as the LE aggregation errors in general (Fig. 4.5), were most prominent during partial vegetation cover than full vegetation cover. Note that spatially variability in f_c can occur due to changes in soil moisture, soil type, management practice etc. Such challenges could be addressed by collecting at a finer scale and then aggregating the flux output, via output aggregation as shown in this study. Furthermore, the statistical distribution of the native LE flux output should be addressed before aggregating LE fluxes. Output flux aggregation is expected to play a role in the validation of coarser scale flux products provided by satellites such as Landsat and Sentinel. The finding here that calculating LE or ET at the original resolution, rather than an aggregated resolution, has been found elsewhere, at least with satellite imagery (Bresnahan et al., 1997; Su et

al., 1999). The downside from these findings, however, is that greater resources (i.e. time, money, etc.) will need to be spent towards post-processing operations, such as GCP deployment, high-grade GPS collection, and orthomosaicking. UAVs also present LE challenges in terms of finer resolution amplifies sources of noise such as shadows, canopy glint, and blurriness from wind (Aboutalebi et al., 2018).

Beyond the model parameterization, it is possible that f_c errors are exaggerated due to UAV data collection process. Multispectral surveys were conducted at different times than the thermal survey, indicating potential differences in illumination conditions between multispectral and thermal surveys (Table 4.1). These temporal differences can result in image misregistration and, therefore, LE estimation errors. However, given that the model results were less than 10 % on these two dates (Table 4.5), and that UAVs were more accurate than MAVs (Fig. 4.9), this potential error does not appear to be substantial. Recent technological improvements have allowed for multispectral and thermal cameras to collect data at the same time, and preliminary results in literature (Maes et al., 2017) suggest this platform setup maybe useful for future UAV studies that aim to model LE via TSEB models.

Aggregated UAV was more accurate in replicating eddy flux towers relative to MAV systems (Fig. 4.9). One hypothesis for this result may be because the differences in altitude between UAV and MAV. As the survey altitude gets further from the ground, outgoing longwave radiation can be attenuated through interaction with water vapor and gasses in the atmospheric column (Torres-Rua et al. 2017). While the thermal correction approach described here has been successful for UAV systems (Rouze et al., in

preparation), for MAV systems the approach is more uncertain due to relatively large pixel resolutions. It is hypothesized that there is more uncertainty in estimations of MAV T_r because the size of the cold object (i.e. polystyrene blocks), was at or slightly smaller than the MAV thermal pixel resolution. Therefore, an average of polystyrene predicted T_r could not be extracted with MAV thermal images. While other approaches that have converted brightness to surface temperature via atmospheric radiative transfer models (Torres-Rua et al., 2017), such approaches could not be applied towards the data here. Another reason why UAV may have outperformed the MAV sensor could be the thermal sensor. Both cameras in this study were uncooled microbolometers and are notorious for producing image blur while the sensor is in motion (Ribiero-Gomes et al., 2017). Given that the MAV was travelling much faster than the UAV (data not shown), the resulting blur could increasingly degrade the former's image quality. Thermal image blur can be reduced using cooled thermal infrared sensors, but these systems cannot be currently equipped aboard UAV platforms, nor are they cost effective (Riberio-Gomes et al., 2017). If funds are available, future studies might consider comparing UAV LE aggregation properties using output aggregation against that of MAV cooled sensors.

In this study, the land use type was mainly uniform, as a uniform seed variety was growing under a uniformly watered landscape. It would be interesting to evaluate UAV LE aggregation properties under production fields with multiple land use types. Kustas et al. (2004), for example, found that LE discrimination between corn and soybean fields was diminished beyond a pixel resolution of 960 m. The effects of these studies will be determined by the nature of the objects themselves, as well as their spatial pattern.

Erhasdi et al. (2013), for example, found that high pixel-scale relative errors were linked with areas that show highly contrasting surface roughness properties such as irrigation canals and production field boundaries. If there is interest beyond the single field scale, the approach described in this study could be used as a means to validate platform sensors, such as satellites. While this study was limited to Landsat 8, future satellite sensors such as Landsat 9 are in the preparation phases. Validation could also be applied for fused satellite products, such as Sentinel-2 and Sentinel-3 as proposed by Guzinski and Nieto et al. (2019).

4.5. Conclusions

The purpose of this study was to evaluate various ET aggregation schemes, both against itself and against pre-existing platforms using energy balance modeling. In 2017, UAV multispectral and thermal imagery, along with field data, were collected over various cotton growth stages. These data sources were combined to model instantaneous latent heat flux using a Priestley-Taylor Two-Source Energy Balance (TSEB-PT) model. Several UAV aggregation schemes were tested, including the initial mode of aggregation (i.e. input image and output flux), as well as the averaging scheme (i.e. simple aggregation vs. Box-Cox). Results indicate that output flux aggregation with Box-Cox averaging (termed Out-BC) produced the lowest relative pixel-scale errors and lowest absolute prediction errors (relative to eddy covariance towers). Out-BC was also more accurate in reproducing latent heat fluxes from manned and satellite imagery, relative to eddy towers. Therefore, UAV ET estimates, despite its data complexity, can be reliably aggregated to coarser pixel resolutions.

4.6. References

Allen, R. G., Tasumi, M., Morse, A., & Trezza, R. (2005). A Landsat-based energy balance and evapotranspiration model in Western US water rights regulation and planning. *Irrigation and Drainage Systems*, *19*(3–4), 251–268. doi:10.1007/s10795-005-5187-z

Bahir, M., Boulet, G., Olioso, A., Rivalland, V., Gallego-Elvira, B., Mira, M., et al. (2017). Evaluation and aggregation properties of thermal infra-red-based evapotranspiration algorithms from 100 m to the km scale over a semi-arid irrigated agricultural area. *Remote Sensing*, *9*, 1178. doi:10.3390/rs9111178

Brenner, C., Zeeman, M., Bernhardt, M., & Schulz, K. (2018). Estimation of evapotranspiration of temperate grassland based on high-resolution thermal and visible range imagery from unmanned aerial systems. *International Journal of Remote Sensing*, *39*(15–16), 5141–5174. doi:10.1080/01431161.2018.1471550

Bresnahan, P. A., & Miller, D. R. (1997). Choice of data scale: predicting resolution error in a regional evapotranspiration model. *Agricultural and Forest Meteorology*, *84*(1–2), 97–113. doi:10.1016/S0168-1923(96)02379-9

Brutsaert, W. (2014). Daily evaporation from drying soil: Universal parameterization with similarity. *Water Resources Research*, *50*(4), 3206–3215.

Campbell, G. S., & Norman, J. M. (1998). *An Introduction to environmental biophysics* (2nd ed.). New York: Springer Science+Business Media.

Carlson, T. N., & Ripley, D. A. (1997). On the relation between NDVI, fractional vegetation cover, and leaf area index. *Remote Sensing of Environment*, *62*(3), 241–252. doi:10.1016/S0034-4257(97)00104-1

Carruthers, I., Rosegrant, M. W., & Seckler, D. (1997). Irrigation and food security in the 21st century. *Irrigation and Drainage Systems*, *11*(2), 83–101. doi:10.1023/A:1005751232728

Cho, K., Kim, Y., & Kim, Y. (2018). Disaggregation of Landsat-8 thermal data using guided SWIR imagery on the scene of a wildfire. *Remote Sensing*, *10*(1), 105. doi:10.3390/rs10010105

Choudhury, B. J., & Monteith, J. L. (1988). A four-layer model for the heat budget of homogeneous land surfaces. *Quarterly Journal of the Royal Meteorological Society*, *114*, 373–398.

Courault, D., Seguin, B., & Olioso, A. (2005). Review on estimation of evapotranspiration from remote sensing data: From empirical to numerical modeling approaches. *Irrigation and Drainage Systems*, *19*(3–4), 223–249. doi:10.1007/s10795-005-5186-0

Duan, T., Chapman, S. C., Guo, Y., & Zheng, B. (2017). Dynamic monitoring of NDVI in wheat agronomy and breeding trials using an unmanned aerial vehicle. *Field Crops Research*, *210*(June), 71–80. doi:10.1016/j.fcr.2017.05.025

Ershadi, A., McCabe, M. F., Evans, J. P., & Walker, J. P. (2013). Effects of spatial aggregation on the multi-scale estimation of evapotranspiration. *Remote Sensing of Environment*, *131*, 51–62.

Fisher, J. B., Melton, F., Middleton, E., Hain, C., Anderson, M., Allen, R., et al. (2017). The future of evapotranspiration: Global requirements for ecosystem functioning, carbon and climate feedbacks, agricultural management, and water resources. *Water Resources Research*, *53*, 2618–2626.

Flörke, M., Schneider, C., & McDonald, R. I. (2018). Water competition between cities and agriculture driven by climate change and urban growth. *Nature Sustainability*, *1*, 51–58.

García-Tejero, I. F., Ortega-Arévalo, C. J., Iglesias-Contreras, M., Moreno, J. M., Souza, L., Tavira, S. C., & Durán-Zuazo, V. H. (2018). Assessing the crop-water status in almond (Prunus dulcis mill.) trees via thermal imaging camera connected to smartphone. *Sensors*, *18*(4), 1–13. doi:10.3390/s18041050

Guzinski, R., & Nieto, H. (2019). Evaluating the feasibility of using Sentinel-2 and Sentinel-3 satellites for high-resolution evapotranspiration estimations. *Remote Sensing of Environment*, *221*(October 2017), 157–172. doi:10.1016/j.rse.2018.11.019

Hassan-Esfahani, L., Ebtehaj, A. M., Torres-Rua, A., & McKee, M. (2017). Spatial scale gap filling using an unmanned aerial system: A statistical downscaling method for applications in precision agriculture. *Sensors*, *17*, 2106. doi:10.3390/s17092106

Hoffmann, H., Nieto, H., Jensen, R., Guzinski, R., Zarco-Tejada, P., & Friborg, T. (2016). Estimating evaporation with thermal UAV data and two-source energy balance models. *Hydrology and Earth System Sciences*, *20*, 697–713.

Hong, S. ho, Hendrickx, J. M. H., & Borchers, B. (2009). Up-scaling of SEBAL derived evapotranspiration maps from Landsat (30 m) to MODIS (250 m) scale. *Journal of Hydrology*, *370*(1–4), 122–138. doi:10.1016/j.jhydrol.2009.03.002

Hunt, E. R., & Daughtry, C. S. T. (2018). What good are unmanned aircraft systems for agricultural remote sensing and precision agriculture? *International Journal of Remote Sensing*, *39*(15–16), 5345–5376. doi:10.1080/01431161.2017.1410300

Jackson, R. D., Reginato, R. J., & Idso, S. B. (1977). Wheat canopy temperature: a practical tool for evaluating water requirements. *Water Resources Research*, *13*, 651–656.

Jarvis, P. G. (1976). The interpretation of the variations in leaf water potential and stomatal conductance found in canopies in the field. *Philosophical Transactions of the Royal Society B: Biological Sciences*, *273*(927), 593–610.

Jones, H. G. (2004). Irrigation scheduling: advantages and pitfalls of plant-based methods. *Journal of Experimental Botany*, *55*(407), 2427–2436. doi:10.1093/jxb/erh213

Jones, H. G., & Sirault, X. R. R. (2014). Scaling of thermal images at different spatial resolution: the mixed pixel problem. *Agronomy*, *4*, 380–396. doi:10.3390/agronomy4030380

Jurena, M. R. (2005). *Soil survey of Burleson County, Texas*. Washington D.C.

Knight, E. J., & Kvaran, G. (2014). Landsat-8 Operational Land Imager design, characterization and performance. *Remote Sensing*, *6*(11), 10286–10305. doi:10.3390/rs61110286

Knipper, K. R., Kustas, W. P., Anderson, M. C., Alfieri, J. G., Prueger, J. H., Hain, C. R., et al. (2019). Evapotranspiration estimates derived using thermal-based satellite remote sensing and data fusion for irrigation management in California vineyards. *Irrigation Science*, *37*(3), 431–449. doi:10.1007/s00271-018-0591-y

Kustas, W. P., & Daughtry, C. S. (1990). Estimation of the soil heat flux/net radiation ratio from spectral data. *Agricultural and Forest Meteorology*, *49*, 205–223.

Kustas, W. P., Li, F., Jackson, T. J., Prueger, J. H., MacPherson, J. I., & Wolde, M. (2004). Effects of remote sensing pixel resolution on modeled energy flux variability of croplands in Iowa. *Remote Sensing of Environment*, *92*(4), 535–547. doi:10.1016/j.rse.2004.02.020

Kustas, W. P., & Norman, J. M. (2000). Evaluating the effects of subpixel heterogeneity on pixel average fluxes. *Remote Sensing of Environment*, *74*(3), 327–342. doi:10.1016/S0034-4257(99)00081-4

Kustas, W. P., & Norman, J. M. (1999). Evaluation of soil and vegetation heat flux predictions using a simple two-source model with radiometric temperatures for partial canopy cover. *Agricultural and Forest Meteorology*, *94*(1), 13–29. doi:10.1016/S0168-1923(99)00005-2

Kustas, W. P., Norman, J. M., Anderson, M. C., & French, A. N. (2003). Estimating subpixel surface temperatures and energy fluxes from the vegetation index-radiometric temperature relationship. *Remote Sensing of Environment*, *85*(4), 429–440. doi:10.1016/S0034-4257(03)00036-1

Li, F., Kustas, W. P., Prueger, J. H., Neale, C. M. U., & Jackson, T. J. (2005). Utility of remote-sensing-based two-source energy balance model under low- and high-vegetation cover conditions. *Journal of Hydrometeorology*, *6*(6), 878–891. doi:10.1175/JHM464.1

Li, Y., Kustas, W. P., Huang, C., Kool, D., & Haghighi, E. (2018). Evaluation of soil resistance formulations for estimates of sensible heat flux in a desert vineyard. *Agricultural and Forest Meteorology*, *260–261*(March), 255–261. doi:10.1016/j.agrformet.2018.06.019

Liou, Y. A., & Kar, S. K. (2014). Evapotranspiration estimation with remote sensing and various surface energy balance algorithms-a review. *Energies*, *7*(5), 2821–2849. doi:10.3390/en7052821

Maes, W. H., Huete, A. R., & Steppe, K. (2017). Optimizing the processing of UAV-based thermal imagery. *Remote Sensing*, *9*(5), 476. doi:10.3390/rs9050476

Manfreda, S., McCabe, M. F., Miller, P. E., Lucas, R., Madrigal, V. P., Mallinis, G., et al. (2018). On the use of unmanned aerial systems for environmental monitoring. *Remote Sensing*, *10*(4). doi:10.3390/rs10040641

Matese, A., Toscano, P., Di Gennaro, S. F., Genesio, L., Vaccari, F. P., Primicerio, J., et al. (2015). Intercomparison of UAV, aircraft and satellite remote sensing platforms for precision viticulture. *Remote Sensing*, *7*(3), 2971–2990. doi:10.3390/rs70302971

McCabe, M. F., & Wood, E. F. (2006). Scale influences on the remote estimation of evapotranspiration using multiple satellite sensors. *Remote Sensing of Environment*, *105*(4), 271–285. doi:10.1016/j.rse.2006.07.006

Moran, M. S., Humes, K. S., & Pinter, P. J. (1997). The scaling characteristics of remotely-sensed variables for sparsely-vegetated heterogeneous landscapes. *Journal of Hydrology*, *190*(3–4), 337–362. doi:10.1016/S0022-1694(96)03133-2

Morison, J. I. L., Baker, N. R., Mullineaux, P. M., & Davies, W. J. (2008). Improving water use in crop production. *Philosophical Transactions of the Royal Society B: Biological Sciences*, *363*(1491), 639–658. doi:10.1098/rstb.2007.2175

Nieto, H., Bellvert, J., Kustas, W. P., Alfieri, J. G., Gao, F., Prueger, J., & Hipps, L. E. (2017). Unmanned airborne thermal and multispectral imagery for estimating evapotranspiration in irrigated vineyards, 5510–5513.

Norman, J. M., Kustas, W. P., & Humes, K. S. (1995). Source approach for estimating soil and vegetation energy fluxes in observations of directional radiometric surface temperature. *Agricultural and Forest Meteorology*, *77*(3–4), 263–293. doi:10.1016/0168-1923(95)02265-Y

Ozdogan, M., Yang, Y., Allez, G., & Cervantes, C. (2010). Remote sensing of irrigated agriculture: opportunities and challenges. *Remote Sensing*, *2*(9), 2274–2304. doi:10.3390/rs2092274

Priestley, C. H. B., & Taylor, R. J. (1972). On the assessment of surface heat flux and evaporation Using large-scale parameters. *Monthly Weather Review*, *100*, 81–92. doi:10.1175/1520-0493(1972)100<0081:otaosh>2.3.co;2

Ramírez-Cuesta, J. M., Allen, R. G., Zarco-Tejada, P. J., Kilic, A., Santos, C., & Lorite, I. J. (2019). Impact of the spatial resolution on the energy balance components on an open-canopy olive orchard. *International Journal of Applied Earth Observation and Geoinformation*, *74*, 88–102. doi:10.1016/j.jag.2018.09.001

Raupach, M. R., & Finnigan, J. J. (1995). Scale issues in boundary-layer meteorology: Surface energy balances in heterogeneous terrain. *Hydrological Processes*, *9*, 589–612.

Ribeiro-Gomes, K., Hernández-López, D., Ortega, J. F., Ballesteros, R., Poblete, T., & Moreno, M. A. (2017). Uncooled thermal camera calibration and optimization of the photogrammetry process for UAV applications in agriculture. *Sensors*, *17*(10), 9–11. doi:10.3390/s17102173

Rouze, G., Neely, H., Morgan, C., Kustas, W., McKee, L., Preuger, J., et al. (n.d.). Evaluation of contextual and non-contextual Unmanned Aerial Vehicle (UAV) evapotranspiration across various pixel resolutions and soil types.

Roy, D. P., Wulder, M. A., Loveland, T. R., C.E., W., Allen, R. G., Anderson, M. C., et al. (2014). Landsat-8: Science and product vision for terrestrial global change research. *Remote Sensing of Environment*, *145*, 154–172. doi:10.1016/j.rse.2014.02.001

Sagan, V., Maimaitijiang, M., Sidike, P., Eblimit, K., Peterson, K. T., Hartling, S., et al. (2019). UAV-based high resolution thermal imaging for vegetation monitoring, and plant phenotyping using ICI 8640 P, FLIR Vue Pro R 640, and thermomap cameras. *Remote Sensing*, *11*(3). doi:10.3390/rs11030330

Sharma, V., Kilic, A., & Irmak, S. (2016). Impact of scale/resolution on evapotranspiration from Landsat and MODIS images. *Water Resources Research*, *52*, 1800–1819. doi:10.1111/j.1752-1688.1969.tb04897.x

Sidwell, R. (1940). Sediments transported by the Brazos River from High Plains, Texas. *Journal of Sedimentary Petrology*, *10*(3), 138–141.

Smith, G. M., & Milton, E. J. (1999). The Use of the empirical line method to calibrate remotely sensed data to reflectance. *International Journal of Remote Sensing*, *20*(13), 2653–2662. doi:10.1080/014311699211994

Smith, R. J., Raine, S. R., Mccarthy, A. C., & Hancock, N. H. (2009). Managing spatial and temporal variability in irrigated agriculture through adaptive control. *Australian Journal of Multi-disciplinary Engineering*, *7*(1), 79–90.

Stanislav, S. (2010). *A Field-scale assessment of soil-specific seeding rates to optimize yield factors and water use in cotton*. Texas A&M University.

Strzepek, K., & Boehlert, B. (2010). Competition for water for the food system. *Philosophical Transactions of the Royal Society B: Biological Sciences*, *365*(1554), 2927–2940. doi:10.1098/rstb.2010.0152

Su, Z., Pelgrum, H., & Menenti, M. (1999). Aggregation effects of surface heterogeneity in land surface processes. *Hydrology and Earth System Sciences*, *3*(4), 549–563. doi:10.5194/hess-3-549-1999

Torres-Rua, A. (2017). Vicarious calibration of sUAS microbolometer temperature imagery for estimation of radiometric land surface temperature. *Sensors*, *17*(7), 5–9. doi:10.3390/s17071499

United Nations, Department of Economic and Social Affairs, P. D. (2017). *World Population Prospects The 2015 Revision*. *The British Journal of Psychiatry*. doi:10.1192/bjp.112.483.211-a

Vanino, S., Nino, P., De Michele, C., Falanga Bolognesi, S., D'Urso, G., Di Bene, C., et al. (2018). Capability of Sentinel-2 data for estimating maximum evapotranspiration and irrigation requirements for tomato crop in Central Italy. *Remote Sensing of Environment*, *215*, 452–470. doi:10.1016/j.rse.2018.06.035

Verstraeten, W. W., Veroustraete, F., & Feyen, J. (2008). Assessment of evapotranspiration and soil moisture content across different scales of observation. *Sensors*, *8*(1), 70–117. doi:10.3390/s8010070

Wang, W. M., Li, Z. L., & Su, H. B. (2007). Comparison of leaf angle distribution functions: Effects on extinction coefficient and fraction of sunlit foliage. *Agricultural and Forest Meteorology*, *143*(1–2), 106–122. doi:10.1016/j.agrformet.2006.12.003

Wang, Y., & Ientilucci, E. (2018). A practical approach to Landsat 8 TIRS stray light correction using multi-sensor measurements. *Remote Sensing*, *10*(4), 1–13. doi:10.3390/rs10040589

Woodcock, C. E., & Strahler, A. H. (1987). The factor of scale in remote sensing. *Remote Sensing of Environment*, *21*(3), 311–332. doi:10.1016/0034-4257(87)90015-0

Wu, H., & Li, Z. L. (2009). Scale issues in remote sensing: A review on analysis, processing and modeling. *Sensors*, *9*(3), 1768–1793. doi:10.3390/s90301768

Wu, M., Yang, C., Song, X., Hoffmann, W. C., Huang, W., Niu, Z., et al. (2018). Monitoring cotton root rot by synthetic Sentinel-2 NDVI time series using improved spatial and temporal data fusion. *Scientific Reports*, *8*(1), 1–12. doi:10.1038/s41598-018-20156-z

Xia, T., Kustas, W. P., Anderson, M. C., Alfieri, J. G., Gao, F., McKee, L., et al. (2016). Mapping evapotranspiration with high-resolution aircraft imagery over vineyards using one-and two-source modeling schemes. *Hydrology and Earth System Sciences*, *20*(4), 1523–1545. doi:10.5194/hess-20-1523-2016

Zhang, J., Yang, C., Zhao, B., Song, H., Hoffmann, W. C., Shi, Y., et al. (2017). Crop classification and LAI estimation using original and resolution-reduced images from two consumer-grade cameras. *Remote Sensing*, *9*(10). doi:10.3390/rs9101054

5. CONCLUSIONS

UAVs are a newly formed technology that offers promise within the realm of agriculture. This is because UAVs offers a wide array of advantages over satellite and manned aircraft, including image detail, flexible data collection, and can even be used in places that would otherwise be difficult to access (such as ponded fields). Because of this advantages, hype has surrounded UAVs, and will continue to do so in the future. As a result, the developments in the technology have outpaced developments in the research, leaving its potential users with an unclear direction regarding its intended uses. The work presented here, therefore, aims to evaluate the suitability of UAV imagery (i.e. thermal, near-infrared, visible) as decision-making tools for precisions agriculture or site-specific management. The two main areas of focus in this regard relate to management zone delineation and ET mapping. While it is currently more common to use UAVs operationally towards crop scouting (because it is simpler), UAVs can offer the greatest economic and environmental benefits through integration with management operations, such as input placement. However, such uses have not been widely adopoted because they are expensive, and studies have not demonstrated a return on investment. While we did not have the resources to conduct a cost benefit analysis, other topics here (i.e. management zones and ET mapping) were selected to demonstrate that such operations are worth exploring.

The purpose of Chapter 2 was to evaluate UAV imagery in terms of modeling MZ traits (e.g. height, seed-cotton yield), as well as management zone delineation, relative to

previously approaches such as soil EC_a. This comparative approach was performed before, during, and at the end of, a single growing season. Regression results indicated that both multispectral imagery (via NDVI) and thermal imagery (T_r) were significant predictors of in-season yield indicators such as canopy height. In addition, their respective MZs showed significant separation during flowering and boll filling, respectively. An RGB sensor could also be used to create MZs at the beginning and end of a season. The paper then addressed how UAV imagery compared with EC_a information in terms of modeling seed cotton yield. While the EC_a survey was also able to separate the field into two distinct zones, AIC_c results indicate that it was outperformed by UAV imagery, even with the high amounts of soil variability encountered within the field. Furthermore, the addition of UAV imagery via open boll imagery significantly affected the previous EC_a-yield model, suggesting the former may complement EC_a if desired.

The purpose of Chapter 3 was to evaluate fluxes estimated from various energy balance models from a UAV throughout a single cotton growing season. The energy balance models evaluated included various non-contextual (TSEB) and contextual (DATTUTDUT) models. These models were applied at various aggregated pixel resolutions (1.05 m and 10.05 m) and evaluated against eddy covariance data across two soil types using apparent electrical conductivity data. Non-contextual (i.e. TSEB) models were more accurate in estimating all energy balance components relative to contextual models (i.e. DATTUTDUT). At 1.05 m, TSEB models behaved similarly in estimating LE relative to eddy flux towers. At 10.05 m, however, TSEB-PT and TSEB-DTD were

the most accurate models, with the latter producing lower biases presumably due to reduction of T_r biases. With respect to soil type, LE model performance within the high clay content soil (~30 %) was slightly better than that from the higher clay content soil (~ 47%), both at 1.05 and 10.05 m. A comparison of spatial LE patterns across the entire field showed that low and high EC_a zones behaved differently with respect to the individual energy balance models. These results were consistent both at cotton flowering and boll production. Across both soil EC_a zones, DATTUTDUT LE fluxes were most dissimilar with TSEB during cotton flowering.

The purpose of Chapter 4 was to evaluate various ET aggregation schemes, both against itself and against pre-existing platforms using energy balance modeling. In 2017, UAV multispectral and thermal imagery, along with field data, were collected over various cotton growth stages. These data sources were combined to model instantaneous latent heat flux using a Priestley-Taylor Two-Source Energy Balance (TSEB-PT) model. Several UAV aggregation schemes were tested, including the initial mode of aggregation (i.e. input image and output flux), as well as the averaging scheme (i.e. simple aggregation vs. Box-Cox). Results indicate that output flux aggregation with Box-Cox averaging (termed Out-BC) produced the lowest relative pixel-scale errors and lowest absolute prediction errors (relative to eddy covariance towers). Out-BC was also more accurate in reproducing latent heat fluxes from manned and satellite imagery, relative to eddy towers. Therefore, UAV ET estimates, despite its data complexity, can be reliably aggregated to coarser pixel resolutions.

Future studies that are interested in researching UAVs should aim to conduct an experimental design over multiple growing seasons. While such an approach was attempted in the year 2016, quality UAV data could not be collected. Furthermore, the multispectral and thermal sensors used in 2016 were different from the ones described in this dissertation. Thus, results would not have been entirely comparable, even if good UAV data were obtained. Continuity in results are a important component of demonstrating value to potential users, such as farmers and other land managers. If resources are available, future studies should conduct a cost benefit analysis to address the monetary value provided by UAVs. Such value could be assessed in terms of input savings and/or output (i.e. yield) increases based on the results presented in this paper. Such resources were not available to the Texas A&M Experimental Farm during the field campaigns. Such endeavors will need to have access to precision agriculture equipment that can spatially modify inputs based on prescriptions via UAVs. To do this, image processing will need to occur in near real time, so that recommendations can be implemented without too much lag time. Such a task, while monumentous, can be aided by designing an automated processing chain for standardizing purposes.

APPENDIX A

PRESENTATION OF SUPPLEMENTARY FIGURES

Fig. A1. Landsat 8 near-infrared (NIR) image (30 m pixel resolution) over study area (red outline) on June 16, 2017. The two yellow circles refer to the eddy covariance flux towers (Tower A and Tower B) shown in Figure 1. Note that the upper flux tower (Tower A, Fig. 1) is located within cloud shadows from a scattered cloud located east of the field. Therefore, all SAT analysis was focused over pixels that do not contain clouds and/or cloud shadows.

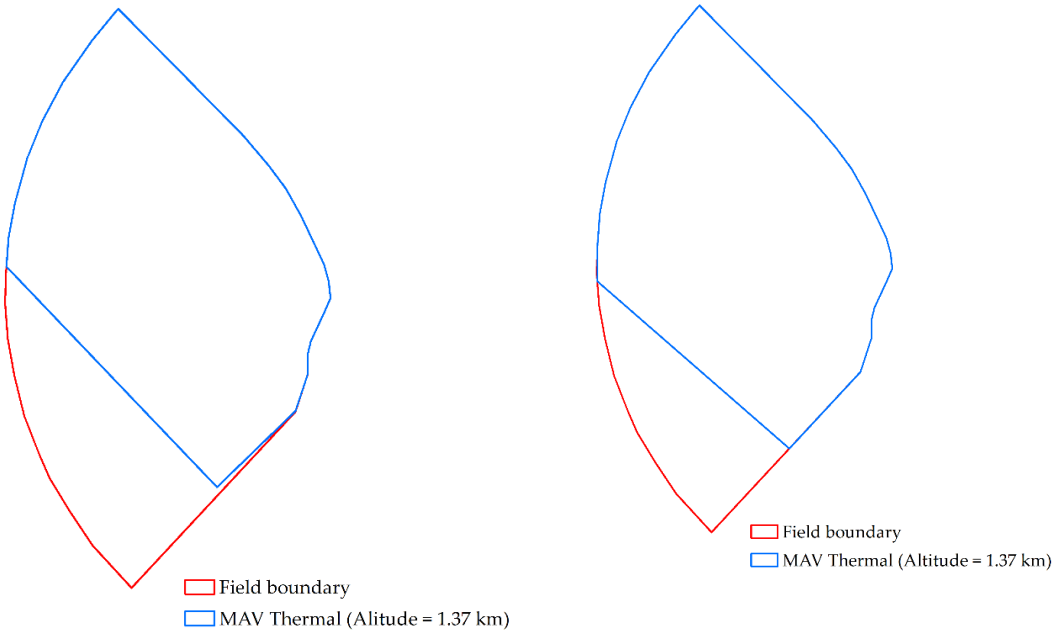

Fig. A2 Boundary of MAV thermal images collected at different altitudes, as well as the field boundary (same as that from Fig. A1).

APPENDIX B

ESTIMATION OF LANDSAT T_R

In this study, T_r was estimated at each i^{th} pixel from an IOP date using the single-channel method by Jimenez-Munoz et al. (2014). The main equation used to estimate T_r is as follows:

$$T_{r,i} = \gamma\left[\varepsilon_i^{-1}\left(\Psi_1 L_{sensor,i} + \Psi_2\right) + \Psi_3\right] + \delta \quad \text{(Eq. B1)}$$

With

$$\gamma_i = \frac{T_{sensor,i}^2}{b_\gamma L_{sensor,i}} \quad \text{(Eq. B2)}$$

Where $L_{sensor,i}$ is the at-sensor radiance (W m^{-2} sr^{-1} μm^{-1}), $T_{sensor,i}$ is the at-sensor brightness temperature (K), and b_γ is a constant (1324).

$L_{sensor,i}$ (used in Eq. A1-A2) is found by:

$$L_{sensor,i} = M_L Q_{cal,i} + A_L \quad \text{(Eq. B3)}$$

Where M_L and A_L are constants ($3.342*10^{-4}$ and 0.1, respectively) provided in the Landsat 8 metadata, and $Q_{cal,i}$ are the digital number (DN) values extracted from the level 1 product.

$T_{sensor,i}$ or TOA brightness temperature, is found as follows:

$$T_{sensor,i} = \frac{K_2}{\ln\left(\frac{K_1}{L_{sensor,i}} + 1\right)} \quad \text{(Eq. B4)}$$

Where K_1 and K_2 are constants (774.8853 and 1321.0789, respectively) from the Landsat 8 metadata, and L_{sensor} is from Equation A3.

ε_i (Eq. B1) is the land surface emissivity which was calculated according to Equation 25 from Yu et al. (2014):

$$\varepsilon_i = \begin{cases} a_i\rho_{red} + b_i & NDVI_i < 0.2 \\ \varepsilon_{v,i}P_{v,i} + \varepsilon_{s,i}\left(1 - P_{v,i}\right) + C_i & 0.2 \le NDVI_i \le 0.5 \\ \varepsilon_{v,i} + C_i & NDVI_i > 0.5 \end{cases} \quad \text{(Eq. B5)}$$

Where NDVI is defined as (Rouse et al., 1973):

$$NDVI_i = \frac{\rho_{i,NIR} - \rho_{i,Red}}{\rho_{i,NIR} + \rho_{i,Red}} \quad \text{(Eq. B6)}$$

Where $\rho_{i,NIR}$ and $\rho_{i,Red}$ are the surface reflectance values from the near-infrared and red bands, respectively using the LEDAPS system; a_i and b_i are the linear coefficients at each ith pixel, $\varepsilon_{v,i}$ and $\varepsilon_{s,i}$ are the vegetation and soil emissivity values, $P_{v,i}$ is the vegetation fraction, and C_i is the surface roughness. $\varepsilon_{v,i}$ and $\varepsilon_{s,i}$ are defined as 0.9863 and 0.9668 by Yu et al. (2014) using a MODIS UCSB (University of California, Santa Barbara) emissivity library. $P_{v,i}$ is defined as (Yu et al., 2014):

$$P_{v,i} = \left[\frac{NDVI - NDVI_{min}}{NDVI + NDVI_{max}}\right]^2 \quad \text{(Eq. B7)}$$

$NDVI_{min}$ is calculated as a field average of NDVI pixels collected from a cloud-free Landsat scene collected around cotton squaring, where soils are the dominant component in the scene (May 15, 2017). $NDVI_{max}$ is calculated as a field average of NDVI pixels collected from a different cloud-free Landsat scene collected around high vegetative growth (July 2, 2017).

C_i is calculated as (Yu et al., 2014):

$$C_i = \left(1 - \varepsilon_{s,i}\right)\varepsilon_{v,i}F'(1 - P_v) \quad \text{(Eq. B8)}$$

Where *F*' is a geometrical factor usually equal to 0.55 (Sanchez et al., 2008).

The atmospheric functions (i.e. Ψ_1, Ψ_2, Ψ_3, Eq. A1) are found by solving the matrix

$$\begin{bmatrix}\Psi_1\\ \Psi_2\\ \Psi_3\end{bmatrix} = \begin{bmatrix}c_{11}c_{12}c_{13}\\ c_{21}c_{22}c_{23}\\ c_{31}c_{32}c_{33}\end{bmatrix}\begin{bmatrix}w^2\\ w\\ 1\end{bmatrix} \quad \text{(Eq. B9)}$$

Where the c_{ij} coefficients are given as (Jimenez-Munoz et al., 2014):

$$\begin{bmatrix}c_{11}c_{12}c_{13}\\ c_{21}c_{22}c_{23}\\ c_{31}c_{32}c_{33}\end{bmatrix} = \begin{bmatrix}0.0419 & 0.02916 & 1.01523\\ -0.3833 & -1.50294 & 0.20324\\ 0.00918 & 1.36072 & -0.27514\end{bmatrix} \quad \text{(Eq. B10)}$$

W refers to the total vapor water content (in g cm^{-2}) estimated using local measurements of near-surface air humidity and density (ref. Equations 14-15 from Wang et al., 2015). Once w is known, Equations B9-B10 are used to find Ψ_1, Ψ_2, Ψ_3 using matrix algebra.

δ (Eq. B1) uses $T_{sensor,i}$ (Eq. B4) and bγ (Eq. B2) as follows:

$$\delta = T_{sensor,i} - \frac{T_{sensor,i}^2}{b_\gamma} \quad \text{(Eq. B11)}$$

γ (Eq. B2), ε_i (Eq. B5), Ψ_1, Ψ_2, Ψ_3 (Eq. A9-A10), $L_{sensor,i}$ (Eq. B3), and δ (Eq. B11) are used to find T_r at each i^{th} pixel (Eq. B1).

References

Jimenez-Munoz, J. C., Sobrino, J. A., Skokovic, D., Mattar, C., & Cristobal, J. (2014). Land surface temperature retrieval methods from landsat-8 thermal infrared sensor data. *IEEE Geoscience and Remote Sensing Letters*, *11*(10), 1840–1843. doi:10.1109/LGRS.2014.2312032

Rouse, J. W., Hass, R. H., Schell, J. A., & Deering, D. W. (1974). Monitoring vegetation systems in the great plains with ERTS. In *Third Earth Resources Technology Satellite (ERTS) symposium* (pp. 309–317).

Sánchez, J. M., Scavone, G., Caselles, V., Valor, E., Copertino, V. A., & Telesca, V. (2008). Monitoring daily evapotranspiration at a regional scale from Landsat-TM and ETM+ data: Application to the Basilicata region. *Journal of Hydrology*, *351*(1–2), 58–70. doi:10.1016/j.jhydrol.2007.11.041

Wang, F., Qin, Z., Song, C., Tu, L., Karnieli, A., & Zhao, S. (2015). An improved mono-window algorithm for land surface temperature retrieval from landsat 8 thermal infrared sensor data. *Remote Sensing*, *7*(4), 4268–4289. doi:10.3390/rs70404268

Yu, X., Guo, X., & Wu, Z. (2014). Land surface temperature retrieval from landsat 8 TIRS-comparison between radiative transfer equation-based method, split window algorithm and single channel method. *Remote Sensing*, *6*(10), 9829–9852. doi:10.3390/rs6109829

APPENDIX C

BOX-COX AVERAGING

This section describes the Box-Cox transformation approach used in this study. The assumption of the Box-Cox method is that the variable(s) of interest (i.e. f_c, LAI, T_r) are distributed in a non-normal manner. The extent to which these variables behave in a non-normal fashion will depend on many variables such, as growth stage, soil moisture etc. (Moran et al., 1997). The purpose of this approach, therefore, is to achieve data normality, so that aggregation is less likely to be affected by sub pixel heterogeneity. The Box Cox transformation aims to find an "optimal" power value (or λ) with which to transform the data (in this case UAV native pixel resolutions) (Box and Cox, 1964). The transformation of the variables ($i.e. y(\lambda)$) has the following form, given the original y dataset:

$$\begin{cases} y(\lambda) = \dfrac{y^{\lambda} - 1}{\lambda} \text{ , } if\ \lambda_1 \neq 0 \\ log\ y \text{ , } if\ \lambda_1 = 0 \end{cases} \quad \text{(Eq. C1)}$$

λ or the optimal power is found using the Maximum Likelihood or log-likelihood method. This is first expressed mathematically as follows (μ=Xβ):

$$f\big(y(\lambda)\big) = \frac{exp(-\frac{1}{2\sigma^2}(y(\lambda) - X\beta)'(y(\lambda) - X\beta)}{(2\pi\sigma^2)^{\frac{n}{2}}} \quad \text{(Eq. C2)}$$

Eq. B2 is then transformed into a proability distribution function (or pdf) by introducing the Jacobian ($\prod_{i=1}^{n} {y_i}^{\lambda-1}$):

$$f\big(y(\lambda)\big) = \frac{exp(-\frac{1}{2\sigma^2}(y(\lambda) - X\beta)'(y(\lambda) - X\beta)}{(2\pi\sigma^2)^{\frac{n}{2}}} \prod_{i=1}^{n} {y_i}^{\lambda-1} \quad \text{(Eq. C3)}$$

Which then results in the log likelihood function:

$$\ln L(\beta, \sigma^2, \lambda|y) \quad \text{(Eq. C4)}$$

$$= -\frac{1}{2\sigma^2}(z - X\beta)'(z - X\beta) - \frac{n}{2}\ln(2\pi\sigma^2) + (\lambda$$

$$- 1)\sum_{i=1}^{n} \ln\,(y_i)$$

Optimal β, σ2 and λ (the latter which is of interest) values are found by maximizing the log likelihood equation or Eq. B4. The λ has the largest log-likelihood value across a range of λ values (usually -5 to 5) is considered the transformation power necessary for the dataset Beyond this point, it is worth pointing the reader to the full computation for Box-Cox elsewhere (Hyde, 1999), as the mathematical details are too cumbersome for this research article.

Once λ was found, the UAV variables were transformed using this value. Next, aggregation was performed on the transformed dataset. Finally, these values were backtransformed to retrieve the values in their original units. The procedure described here was performed using several built-in functions and custom functions developed within the R programming language, including powerTransform() for the Box-Cox transformation (Fox, 2019) and raster() for image aggregation (Hijmans et al., 2019).

References

Box, G. E. P., & Cox, D. R. (1964). An Analysis of transformations. *Journal of the Royal Statistical Society. Series B (Methodological)*. doi:10.1017/S0031819100000875

Fox, J., Weisberg, S., & Price, B. (2019). *An R companion to applied regression* (3rd ed.). Thousand Oaks, CA: SAGE Publications, Inc.

Hijmans, R. J., Etten, J. Van, Sumner, M., Cheng, J., Bevan, A., Bivand, R., et al. (2019). Geographic data analysis and modeling.

Hyde, S. (1999). *Likelihood based inference on the box-cox family of transformations: SAS and Matlab programs*.

Moran, M. S., Humes, K. S., & Pinter, P. J. (1997). The scaling characteristics of remotely-sensed variables for sparsely-vegetated heterogeneous landscapes. *Journal of Hydrology*, *190*(3–4), 337–362. doi:10.1016/S0022-1694(96)03133-2

APPENDIX C

FOOTPRINTS

Appendix C.1. Tower locations, processing and results

Two eddy covariance flux towers were installed within the field (Fig. 1). The clay content at the Towers A and B are 296 and 466 g kg^{-1} respectively. Details of the sensors and general data collection are previously provided by Rouze et al. (in preparation). High frequency raw data collected by the eddy covariance towers were then post-processed within EddyPro software version 6.2.1 (LI-COR) to quality check raw data and remove potential outliers. After EddyPro processing, turbulent fluxes were corrected by an additional 10 %, based on recent findings of underestimates in vertical velocity using a non-orthogonal CSAT-3 anemometer (Kochendorfer et al., 2012; Frank et al., 2013). The average energy balance closure for each tower before and after correction is shown in Table B.1. The average closure across all dates and towers after the correction methods above was 0.90. Across all dates and towers, energy closure after correction was at least above 80 %, and this falls in line with closures reported from previous studies (Chavez et al., 2005; Xia et al., 2016).

Table C.1. Closure ratio (i.e. $\frac{LE+H}{Rn-G}$) before and after applying corrections (i.e. LE * 1.1, H * 1.1) to EddyPro fluxes. July 18 fluxes at the high EC_a site are omitted here, as the anemometer within the high EC_a zone was "looking at" a poorly vegetated part of the field.

Date	Time	Associated Platform	Closure Ratio - unclosed		Closure Ratio - closed with 1.1	
			High EC_a	Low EC_a	High EC_a	Low EC_a
June 16, 2017	11:57	SAT	0.91	1.00	1.00	1.10
June 16, 2017	13:00-13:15	UAV	0.86	0.85	0.94	0.93
June 16, 2017	13:21-13:47	MAV	0.89	0.93	0.98	1.02
June 16, 2017	13:58-14:10	MAV	0.91	0.86	1.00	0.95
July 28 2017	14:46-15:00	UAV	0.95	1.02	1.05	1.12
July 28 2017	14:45-15:09	MAV	0.90	0.96	0.98	1.06
July 28 2017	15:17-15:31	MAV	0.93	1.15	1.02	1.26

Appendix C.2. Footprints

The footprint of the fluxes measured by the eddy covariance tower describes the source area of the fluxes depending on parameters such as wind direction, wind speed, and atmospheric stability (Burba and Anderson, 2010). In order to effectively compare the UAV and eddy tower fluxes, footprints need to be generated in two-dimensional coordinate space. In this study, footprints were calculated using the footprint models by Hsieh et al. (2000) and Detto et al. (2006). UAV predicted fluxes were averaged within each footprint using the source weighted scheme proposed by Li et al. (2008):

$$\overline{UAV\ Flux} = \frac{\sum_{i=1}^{n} f(x_i, y_i, z_m) FLUX(x_i y_i)}{\sum_{1}^{n} f(x_i, y_i, z_m)}, \quad \text{(Eq. C1)}$$

where *i* is a given pixel with location x_i, y_i, given the flux tower height z_m. Note that each i^{th} pixel has an associated weight (i.e. $f(x_i,y_i,z_m)$) based on its corresponding location to the anemometer.

References

Burba, G., & Anderson, D. (2010). *A Brief practical guide to eddy covariance flux measurements: principles and workflow examples for scientific and industrial applications*. Lincoln, NE, USA: LI-COR Biosciences.

Chávez, J. L., Neale, C. M. U., Hipps, L. E., Prueger, J. H., & Kustas, W. P. (2005). Comparing aircraft-based remotely sensed energy balance fluxes with eddy covariance tower data using heat flux source area functions. *Journal of Hydrometeorology*, *6*(6), 923–940. doi:10.1175/JHM467.1

Detto, M., Montaldo, N., Albertson, J. D., Mancini, M., & Katul, G. (2006). Soil moisture and vegetation controls on evapotranspiration in a heterogeneous

Mediterranean ecosystem on Sardinia, Italy. *Water Resources Research*, *42*(8), 1–16. doi:10.1029/2005WR004693

Frank, J. M., Massman, W. J., & Ewers, B. E. (2013). Underestimates of sensible heat flux due to vertical velocity measurement errors in non-orthogonal sonic anemometers. *Agricultural and Forest Meteorology*, *171–172*, 72–81. doi:10.1016/j.agrformet.2012.11.005

Hsieh, C. I., Katul, G., & Chi, T. W. (2000). An approximate analytical model for footprint estimation of scalar fluxes in thermally stratified atmospheric flows. *Advances in Water Resources*, *23*(7), 765–772. doi:10.1016/S0309-1708(99)00042-1

Kochendorfer, J., Meyers, T. P., Frank, J., Massman, W. J., & Heuer, M. W. (2012). How well can we measure the vertical wind speed? Implications for fluxes of energy and mass. *Boundary-Layer Meteorology*, *145*(2), 383–398. doi:10.1007/s10546-012-9738-1

Li, F., Kustas, W. P., Anderson, M. C., Prueger, J. H., & Scott, R. L. (2008). Effect of remote sensing spatial resolution on interpreting tower-based flux observations. *Remote Sensing of Environment*, *112*(2), 337–349. doi:10.1016/j.rse.2006.11.032

Xia, T., Kustas, W. P., Anderson, M. C., Alfieri, J. G., Gao, F., McKee, L., et al. (2016). Mapping evapotranspiration with high-resolution aircraft imagery over vineyards using one-and two-source modeling schemes. *Hydrology and Earth System Sciences*, *20*(4), 1523–1545. doi:10.5194/hess-20-1523-2016